Transverse mode instability in high-power ytterbium doped fiber ampliers

Kristian Rymann Hansen

Ph. D. Thesis

June 2013

DTU Fotonik
Department of Photonics Engineering

Transverse mode instability in high-power ytterbium doped fiber amplifiers

PhD thesis

Kristian Rymann Hansen

December 31st, 2012

DTU Fotonik
Department of Photonics Engineering

DTU Fotonik
Department of Photonics Engineering
Technical University of Denmark
Ørsteds Plads 343
DK-2800 Kgs. Lyngby
Denmark

In memory of my grandfather, Waldemar Friedrich Nielsen Dall.

Contents

Preface vii

Abstract ix

Resumé (Danish abstract) xi

List of publications xiii

1 Introduction 1
- 1.1 Background . . . 1
- 1.2 Scope of the thesis . . . 2
- 1.3 Organization of the thesis . . . 2

2 Fiber amplifiers 5
- 2.1 The step-index fiber . . . 5
  - 2.1.1 Fiber design and materials . . . 5
  - 2.1.2 Fiber modes . . . 7
- 2.2 The photonic crystal fiber . . . 11
  - 2.2.1 Manufacturing of photonic crystal fibers . . . 13
  - 2.2.2 Index guiding fibers . . . 14
  - 2.2.3 Photonic bandgap fibers . . . 16
- 2.3 Active fibers and ytterbium doping . . . 17
  - 2.3.1 Energy states of ytterbium . . . 17
  - 2.3.2 Rate equations and gain . . . 19
- 2.4 Nonlinear effects in fibers . . . 20
  - 2.4.1 The nonlinear induced polarization . . . 21
  - 2.4.2 Self-phase modulation . . . 23
  - 2.4.3 Stimulated Raman scattering . . . 23
  - 2.4.4 Stimulated Brillouin scattering . . . 25

3 Circularly symmetric beam propagation method 27
3.1 Beam propagation method . . . 28
3.1.1 Beam propagation equation . . . 28
3.1.2 Density matrix and rate equations . . . 29
3.1.3 Split-operator method . . . 31
3.1.4 Thermal nonlinearity . . . 32
3.1.5 Pump propagation equation . . . 32
3.2 Numerical results . . . 33
3.2.1 Thermal lensing . . . 34
3.2.2 Thermally induced multimode behavior . . . 38
3.3 Conclusion . . . 46

4 Fourier expansion beam propagation method 49
4.1 Numerical method . . . 50
4.1.1 Beam propagation equation . . . 50
4.1.2 Input signal field . . . 52
4.1.3 Thermal nonlinearity . . . 53
4.1.4 Pump propagation equation . . . 53
4.2 Numerical results . . . 54
4.2.1 Forward pumping . . . 55
4.2.2 Backward pumping . . . 58
4.3 Conclusion . . . 60

5 Semi-analytic model of transverse mode instability 63
5.1 Coupled-mode equations . . . 64
5.2 TMI threshold of a SIF amplifier . . . 67
5.2.1 Calculation of the coupling constant . . . 68
5.2.2 Solution of the coupled-mode equations . . . 69
5.3 TMI threshold of a PCF amplifier . . . 72
5.4 Conclusion . . . 76

6 Coupled-mode model of transverse mode instability 77
6.1 Introduction . . . 77
6.2 Theory . . . 79
6.2.1 Coupled mode equations . . . 79
6.2.2 Steady-state solution . . . 84
6.3 Operation at threshold . . . 85
6.3.1 Quantum noise seeding . . . 85
6.3.2 Intensity noise seeding . . . 90
6.3.3 $LP_{01} - LP_{02}$ coupling . . . 93
6.3.4 Numerical results . . . 94

6.4 Operation beyond threshold 95
6.5 Amplitude modulated input signal 99
6.5.1 Perturbative calculation 101
6.5.2 Numerical results 103
6.6 Conclusion 111

7 Summary and outlook **113**
7.1 Summary 113
7.2 Outlook 115

List of acronyms **117**

Bibliography **119**

Preface

This thesis presents the results obtained from the scientific research carried out as part of the author's PhD project during the period January 1, 2010 to December 31, 2012. The work was carried out at the Department of Photonics Engineering (DTU Fotonik), Technical University of Denmark, and was funded by a grant from the Danish Council for Independent Research - Technology and Production.

The research was carried out under the supervision of Associate Professor Jesper Lægsgaard, PhD (DTU Fotonik) and Jes Broeng, PhD (Senior Executive Consultant - Business Development, DTU Fotonik).

Acknowledgments

I would like to express my sincere gratitude to my supervisors Jesper Lægsgaard and Jes Broeng for their helpfulness and competent guidance during my PhD project. Also, a special thanks to Thomas Tanggaard Alkeskjold of NKT Photonics A/S. Even though not officially a supervisor, he has taken a keen interest in my work and has provided invaluable help and feedback.

My friends and colleagues at DTU Fotonik deserve thanks for their helpfulness and for making DTU Fotonik a fun and enjoyable place to be. Finally, my family and friends off-campus deserve my gratitude for keeping me in touch with the world outside of academia.

Abstract

The last couple of decades have brought an impressive growth in the output power of rare-earth doped fiber lasers and amplifiers, reaching the kW average power regime in both CW and pulsed systems. As a result, even though fiber lasers have excellent heat dissipation properties, thermal effects due to quantum defect heating have recently begun to negatively impact these systems when operating at high average power. The guiding properties of large-core fiber amplifiers have been observed to change as the operating power is increased, and recently a mode instability phenomenon, which severely degrades the otherwise nearly diffraction-limited beam quality of fiber amplifiers, was discovered. The latter effect has impeded the further power scaling of fiber lasers, since the mode instability sets in when the average power exceeds a certain threshold.

The purpose of the research presented in this thesis is to provide a theoretical understanding of the thermo-optical effects in high-power ytterbium doped fiber amplifiers, with a particular emphasis on understanding the aforementioned mode instability issue. Two main approaches to the problem have been used. The first is the development of a numerical model based on the beam propagation method, and the second is by a formulation of a coupled-mode model of thermally induced mode instability. The former approach is used to study the effect of quantum defect heating on the guiding properties of the fiber, while the latter provides a simplified description of the mode instability. In spite of the approximations made in the formulation of the coupled-mode model, it will be shown that this model is able to explain most of the experimentally observed qualitative features of the mode instability phenomenon.

Resumé (Danish abstract)

De seneste par årtier har bragt en imponerende vækst i udgangseffekten af sjælden-jordartsmetal doterede fiberlasere- og forstærkere, og kW middeleffekt er opnået i både CW og pulsede systemer. Som følge heraf er termiske effekter pga. kvantedefekt opvarmning begyndt at påvirke disse systemer negativt ved høj middeleffekt, på trods af deres fremragende varmespredningsegenskaber. Det er observeret at lysleder egenskaberne af stor-kerne fiberforstærkere ændres når effekten øges, og et mode-ustabilitetsfænomen, som forværrer den ellers næsten diffraktionsbegrænsede strålekvalitet af fiberforstærkere betragtligt, er for nyligt blevet opdaget. Sidstnævnte effekt har modvirket yderligere opskalering af fiberlaseres effekt, eftersom mode-ustabiliteten sætter ind når middeleffekten overstiger en bestemt grænse.

Formålet med forskningen præsenteret i denne afhandling er at skabe en teoretisk forståelse af termo-optiske effekter i højeffekt ytterbium-doterede fiberforstærkere, med et særligt fokus på forståelsen af førnævnte mode-ustabilitetsfænomen. To hovedfremgangsmåder til problemet er blevet benyttet. Den første er udviklingen af en numerisk model, baseret på den såkaldte "beam propagation method", og den anden er ved formuleringen af en koblet-mode model af termisk induceret mode-ustabilitet. Førstnævnte er brugt til at studere effekten af kvantedefekt opvarmning på fiberens lysleder egenskaber, mens sidstnævnte giver en simplificeret beskrivelse af mode-ustabilitet. Det vil blive vist at denne model er istand til at forklare de fleste af de eksperimentelt observerede kvalitative egenskaber ved mode-ustabilitetsfænomenet, på trods af de anvendte approksimationer.

List of publications

Journal publications

The following articles form the basis of this thesis:

[1] K. R. Hansen, T. T. Alkeskjold, J. Broeng, and J. Lægsgaard, "Thermo-optical effects in high-power Ytterbium-doped fiber amplifiers," Opt. Express **19**, 23965–23980 (2011).

[2] K. R. Hansen, T. T. Alkeskjold, J. Broeng, and J. Lægsgaard, "Thermally induced mode coupling in rare-earth doped fiber amplifiers," Opt. Lett. **37**, 2382–2384 (2012).

[3] K. R. Hansen, T. T. Alkeskjold, J. Broeng, and J. Lægsgaard, "Theoretical analysis of mode instability in high-power fiber amplifiers," Opt. Express (submitted for publication).

In addition, the following article was published during the PhD project, but is not discussed in this thesis:

[4] M. Laurila, M. M. Jørgensen, K. R. Hansen, T. T. Alkeskjold, J. Broeng, and J. Lægsgaard, "Distributed mode filtering rod fiber amplifier delivering 292W with improved mode stability," Opt. Express **20**, 5742–5753 (2012).

Conference contributions

[5] K. R. Hansen, and J. Lægsgaard, "Thermal Effects in High-Power Fiber Amplifiers," in *CLEO:2011 - Laser Applications to Photonic Applications*, OSA Technical Digest (CD) (Optical Society of America, 2011), paper JWA32.

[6] M. M. Jørgensen, K. R. Hansen, M. Laurila, D. Noordegraaf, T. T. Alkeskjold, and J. Lægsgaard, "Modal instabilities in very large mode area rod fiber amplifiers," in *Northern Optics 2012*, Snekkersten, Denmark (2012).

[7] M. M. Jørgensen, K. R. Hansen, M. Laurila, T. T. Alkeskjold, and J. Lægsgaard, "Modal instability of rod fiber amplifiers: a semi-analytic approach," in *SPIE, Photonics West 2013* (accepted).

Chapter 1

Introduction

1.1 Background

Rare-earth doped fiber lasers and amplifiers have a long and distinguished history as a backbone technology in long-haul optical communications, in particular the erbium doped fiber amplifier, which can provide gain in the telecom band around 1550 nm. During the last couple of decades, however, the output power of rare-earth doped fiber lasers has increased considerably, and fiber lasers are now beginning to find their way into applications that require high output power, such as e.g. precision laser cutting and scribing.

The fiber laser offers a number of advantages over the traditional rod-type solid-state laser. In particular their near diffraction-limited beam quality, resilience to environmental disturbances and their flexibility and compactness. In addition, fiber lasers are less affected by thermal effects caused by heat generated in the gain medium due to their large ratio of the surface area to the volume of the gain medium. On the negative side, the long length and tight confinement of the beam make the fiber laser more susceptible to detrimental nonlinear effects. However, with the invention of the photonic crystal fiber (PCF) in the mid 1990's came the possibility to produce single-mode fibers with much larger cores, which reduced the negative impact of nonlinear effects and lead to an impressive increase in both peak and average power in PCF lasers and amplifiers.

With the increase in operating power, which broke the 1 kW barrier in the mid 2000's [8], the presence of thermal effects began to become an issue. Initial theoretical investigations of the effects of quantum defect heating focused mainly on mechanical limitations such as thermally induced stresses and melting, and on optimizing the heat dissipation in the fiber [9, 10, 11, 12].

Later it was realized that the presence of strong radial thermal gradients could potentially alter the guiding properties of the fiber due to the temperature dependence of the refractive index of silica [13], but further scaling of the output power while maintaining near diffraction-limited output was still considered possible.

Then, around 2011, came the first published reports [14, 15, 16] of a new "mode instability" phenomenon, which we shall refer to as transverse mode instability (TMI) in this thesis. This instability manifested itself as a sudden degradation of the beam quality and pointing stability of the signal as the average output power was increased beyond a certain threshold value, which depended on the particular fiber amplifier. This phenomenon has become a major challenge to further power scaling of fiber amplifiers.

1.2 Scope of the thesis

The purpose of this PhD project was to theoretically investigate thermo-optical effects in high-power ytterbium doped fiber amplifiers. The initial work focused on developing a numerical model, based on the beam propagation method (BPM), which could take the effects of thermally induced changes in the refractive index of the fiber material into account, as well as gain saturation effects. The model was initially intended to be used primarily to study thermal lensing effects in detail, but following anecdotal and later published reports of the phenomenon of TMI, the focus quickly shifted to understand and model this effect. After it was realized that the BPM model could not adequately explain TMI, work was initiated to formulate the problem in terms of coupled modes, which resulted in a semi-analytical treatment of the problem, as well as a more comprehensive numerical coupled-mode model. This work on TMI thus constitutes the main results of the project.

1.3 Organization of the thesis

A brief overview of certain aspects of the theory of fiber amplifiers is given in chapter 2. This treatment is by no means intended to be exhaustive, but merely to serve as a background for the work presented in the thesis.

The results obtained with a circularly symmetric 2D BPM model of ytterbium doped fiber amplifiers are presented in chapter 3, where thermal lensing, thermally induced multimode behavior and initial attempts to explain TMI are discussed. The results presented in this chapter are also published in [1]. The extension of the model to 3D by means of a Fourier expansion of the azimuthal

dependence of the dynamical variables is presented in chapter 4. This numerically efficient method is used to study the interaction between the LP_{01} and LP_{11} modes of a large-core fiber amplifier under high average power operation.

A semi-analytic model of quantum noise seeded TMI is presented in chapter 5. The TMI threshold power is calculated, and the model is used to study the dependence of the threshold on various design parameters of a step-index fiber (SIF). This work is published in [2]. It is also demonstrated how the model can be applied to PCFs, which was done in collaboration with Mette Marie Jørgensen from the Department of Photonics Engineering, Technical University of Denmark [6, 7].

A complete coupled-mode model of TMI is formulated in chapter 6. Compared to the semi-analytic model, this model provides a much more detailed description of the dynamics of TMI. The predictions of this model are compared to a number of recently experimentally discovered features of TMI. The results presented in this chapter have been submitted for publication and is currently undergoing peer review [3]. Finally, a summary of the thesis and an outlook towards future research is given in chapter 7.

Chapter 2

Fiber amplifiers

In this chapter we shall review some aspects of the theory of optical fibers, which will serve as the foundation for the work presented in this thesis. In section 2.1 we discuss the theory of the simple SIF. This simple model turns out to be very useful, as it often provides a reasonable approximation to the more complicated PCF, discussed in section 2.2. Due to the wide variety of PCF designs, we shall only discuss the more general properties of these fibers here.

In section 2.3 we discuss rare-earth doped fibers, with special emphasis on ytterbium doping, and review some basic theory of stimulated emission and gain in such fibers. Finally, we briefly review some aspects of the nonlinear effects in optical fibers which are detrimental to the power scaling of fiber amplifiers in section 2.4.

2.1 The step-index fiber

2.1.1 Fiber design and materials

An illustration of the cross section of a typical SIF is shown in Fig. 2.1. It consists of a small center core of radius R_c and refractive index n_c surrounded by a much thicker cladding with a slightly lower refractive index n_{cl}. As we shall see, this refractive index difference allows the fiber core to guide light due to total internal reflection (TIR) at the core-cladding interface.

Optical fibers of this kind are typically made of highly pure silica (SiO_2) glass, which has a refractive index $n_{SiO_2} \approx 1.45$ at a wavelength of 1 μm. To produce the necessary index difference, the core typically consists of germanium doped silica, which increases its refractive index relative to the pure

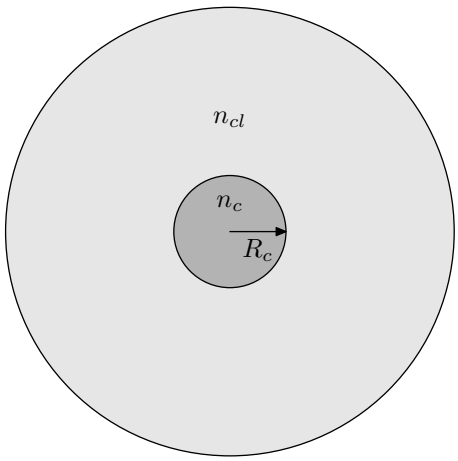

Figure 2.1: The cross section of a SIF.

silica cladding. The precise index contrast is determined by the dopant concentration, and index differences up to approximately 0.05 can be obtained in this way. Other dopants can be used to modify the refractive index, such as e.g. fluorine which can be used to lower the refractive index of the cladding, but index differences much higher than the above mentioned 0.05 are hard to obtain. Perhaps more importantly, it is difficult to produce SIFs with index contrasts smaller than 10^{-3} due to the finite precision of the manufacturing process.

The high purity of the glass makes for extremely low losses at visible and near-infrared wavelengths. The dominant loss mechanism at wavelengths down to the telecom wavelength of 1550 nm is Rayleigh scattering by intrinsic nm-scale inhomogeneities in the glass. The loss due to Rayleigh scattering scales with wavelength as λ^{-4} and so the total loss reaches a minimum at 1550 nm, where absorption due to excitation of lattice vibrations in the silica matrix begins to dominate. The best optical communications fibers have reduced losses to a mere 0.2 dB/km at a wavelength of 1550 nm.

Typical core diameters range from a few μm for single-mode fibers to several hundred μm for heavily multimode fibers. Single-mode fibers have the advantage of greater beam quality, which is important in fiber laser systems, and higher data transmission rates in optical communication systems compared to the multimode fibers. However, as we shall see later, the smaller core required for single-mode guidance makes these fibers more susceptible to unwanted nonlinear effects.

2.1.2 Fiber modes

The electric and magnetic fields in the optical fiber obey the source-free Maxwell equations

$$\nabla \cdot \mathbf{D}(\mathbf{r}, t) = 0, \tag{2.1a}$$
$$\nabla \cdot \mathbf{B}(\mathbf{r}, t) = 0, \tag{2.1b}$$
$$\nabla \times \mathbf{E}(\mathbf{r}, t) = -\frac{\partial \mathbf{B}}{\partial t}, \tag{2.1c}$$
$$\nabla \times \mathbf{H}(\mathbf{r}, t) = \frac{\partial \mathbf{D}}{\partial t}, \tag{2.1d}$$

where $\mathbf{E}$ and $\mathbf{H}$ are the electric and magnetic fields, respectively, $\mathbf{D}$ is the electric displacement and $\mathbf{B}$ is the magnetic flux density. The constitutive relations between the electric and magnetic fields and the electric displacement and magnetic flux density are given by

$$\mathbf{D}(\mathbf{r}, t) = \varepsilon_0 \mathbf{E}(\mathbf{r}, t) + \mathbf{P}(\mathbf{r}, t), \tag{2.2a}$$
$$\mathbf{B}(\mathbf{r}, t) = \mu_0 \mathbf{H}(\mathbf{r}, t) + \mathbf{M}(\mathbf{r}, t), \tag{2.2b}$$

where ε_0 is the vacuum permittivity, μ_0 is the vacuum permeability, $\mathbf{P}$ is the polarization and $\mathbf{M}$ is the magnetization of the fiber material. For a dielectric such as silica, the magnetization is zero to an excellent approximation.

To obtain a wave equation for the electric field, we take the curl of Eq. (2.1c) and use Eq. (2.1d) along with the constitutive equations (2.2) which gives

$$\nabla \times \nabla \times \mathbf{E}(\mathbf{r}, t) + \frac{1}{c^2} \frac{\partial^2 \mathbf{E}}{\partial t^2} = -\mu_0 \frac{\partial^2 \mathbf{P}}{\partial t^2}, \tag{2.3}$$

where c is the speed of light in vacuum. Taking the Fourier transform[1] with respect to t yields the wave equation in the angular frequency domain

$$\nabla \times \nabla \times \mathbf{E}(\mathbf{r}, \omega) - k^2 \mathbf{E}(\mathbf{r}, \omega) = \mu_0 \omega^2 \mathbf{P}(\mathbf{r}, \omega), \tag{2.4}$$

where $k^2 = \omega^2 / c^2$.

In our discussion of fiber modes of a SIF, we assume that the fiber material is well approximated by an isotropic, linear dielectric, in which case the induced polarization is related to the electric field by a scalar linear susceptibility $\chi^{(1)}$

$$\mathbf{P}(\mathbf{r}, \omega) = \varepsilon_0 \chi^{(1)}(\mathbf{r}, \omega) \mathbf{E}(\mathbf{r}, \omega). \tag{2.5}$$

[1] We use the Fourier transform convention $f(\omega) = \int_{-\infty}^{\infty} f(t) e^{-i\omega t} \mathrm{d}t$.

Inserting the induced polarization into Eq. (2.4) yields a wave equation valid for a fiber in the absence of birefringence and nonlinear effects

$$\nabla \times \nabla \times \mathbf{E}(\mathbf{r},\omega) - \varepsilon(\mathbf{r},\omega)k^2\mathbf{E}(\mathbf{r},\omega) = 0, \tag{2.6}$$

where we have introduced the relative permittivity $\varepsilon = 1+\chi^{(1)}$. For small index contrasts we can invoke the so-called *weakly guiding* or *scalar* approximation to rewrite the double curl operator as

$$\nabla \times \nabla \times \mathbf{E}(\mathbf{r},\omega) = \nabla\left(\nabla \cdot \mathbf{E}(\mathbf{r},\omega)\right) - \nabla^2\mathbf{E}(\mathbf{r},\omega) \approx -\nabla^2\mathbf{E}(\mathbf{r},\omega), \tag{2.7}$$

and the wave equation takes the form of the vector Helmholtz equation

$$\nabla^2\mathbf{E}(\mathbf{r},\omega) + \varepsilon(\mathbf{r},\omega)k^2\mathbf{E}(\mathbf{r},\omega) = 0. \tag{2.8}$$

Using the fact that the relative permittivity of the fiber is invariant in the longitudinal direction, which we take to be the z direction, we look for solutions of Eq. (2.8) on the form

$$\mathbf{E}(\mathbf{r},\omega) = \mathbf{E}_0\Psi(\mathbf{r}_\perp,\omega)e^{-i\beta(\omega)z}, \tag{2.9}$$

where $\mathbf{E}_0$ is a constant vector specifying the polarization, amplitude and phase of the electric field, Ψ is a normalized transverse mode function which depends on the transverse coordinates $\mathbf{r}_\perp$ and β is a frequency dependent propagation constant. With this ansatz Eq. (2.8) takes the form of an eigenvalue equation

$$\nabla_\perp^2\Psi(\mathbf{r}_\perp,\omega) + \varepsilon(\mathbf{r}_\perp,\omega)k^2\Psi(\mathbf{r}_\perp,\omega) = \beta(\omega)^2\Psi(\mathbf{r}_\perp,\omega), \tag{2.10}$$

which can be solved for the mode functions Ψ and corresponding propagation constants β. The modes will in general consist of a discrete set of guided modes, which are confined within the fiber structure, and a continuum of radiation modes, which are not confined. In the following, we shall concern ourselves only with the guided modes.

For a fiber with a circularly symmetric cross section, it is convenient to write Eq. (2.10) in polar coordinates r, ϕ:

$$\frac{\partial^2\Psi}{\partial r^2} + \frac{1}{r}\frac{\partial\Psi}{\partial r} + \frac{1}{r^2}\frac{\partial^2\Psi}{\partial\phi^2} + \varepsilon(r)k^2\Psi(r,\phi) = \beta^2\Psi(r,\phi), \tag{2.11}$$

where we have omitted ω from the notation for brevity. Since the relative permittivity ε is independent of ϕ, we look for solutions on the form

$$\Psi_m^c(r,\phi) = R_m(r)\cos(m\phi), \tag{2.12a}$$
$$\Psi_m^s(r,\phi) = R_m(r)\sin(m\phi), \tag{2.12b}$$

where m is required to be a non-negative integer. For the SIF illustrated in Fig. 2.1, the radial mode functions R_m must then satisfy the eigenvalue equation

$$\frac{\partial^2 R_m}{\partial r^2} + \frac{1}{r}\frac{\partial R_m}{\partial r} - \frac{m^2}{r^2}R_m + k^2 n_c^2 R_m = \beta^2 R_m \quad \text{for } r \leq R_c, \tag{2.13a}$$

$$\frac{\partial^2 R_m}{\partial r^2} + \frac{1}{r}\frac{\partial R_m}{\partial r} - \frac{m^2}{r^2}R_m + k^2 n_{cl}^2 R_m = \beta^2 R_m \quad \text{for } r > R_c, \tag{2.13b}$$

where we used the fact that $\varepsilon = n^2$ for loss-less dielectrics. Introducing the *effective index* $n_{eff} = \beta/k$ and the dimensionless variables

$$u = ar = kr\sqrt{n_c^2 - n_{eff}^2} \tag{2.14a}$$

$$v = br = kr\sqrt{n_{eff}^2 - n_{cl}^2} \tag{2.14b}$$

the radial eigenvalue equation becomes

$$u^2\frac{\partial^2 R_m}{\partial u^2} + u\frac{\partial R_m}{\partial u} + \left(u^2 - m^2\right) R_m(u) = 0 \quad \text{for } u \leq aR_c, \tag{2.15a}$$

$$v^2\frac{\partial^2 R_m}{\partial v^2} + v\frac{\partial R_m}{\partial v} - \left(v^2 + m^2\right) R_m(v) = 0 \quad \text{for } u > bR_c. \tag{2.15b}$$

The solutions to Eq. (2.15a) are linear combinations of the Bessel functions of the first kind $J_m(u)$ and second kind[2] $Y_m(u)$, but since the latter is singular at $r = 0$, only the former is included in the solution. Analogously, the solutions to Eq. (2.15b) are linear combinations of the modified Bessel functions of the first kind $I_m(v)$ and second kind $K_m(v)$. Since we are looking for guided mode solutions, we impose the boundary condition

$$\lim_{v\to\infty} R_m(v) = 0 \tag{2.16}$$

which immediately implies that only the modified Bessel function of the second kind K_m is included. The cosine solutions to Eq. (2.13) are thus given by

$$\Psi_m^c(r,\phi) = AJ_m(ar)\cos(m\phi) \qquad \text{for } r \leq R_c, \tag{2.17a}$$

$$\Psi_m^c(r,\phi) = BK_m(br)\cos(m\phi) \qquad \text{for } r > R_c, \tag{2.17b}$$

with an analogous expression for the sine solutions. The effective index n_{eff} is determined by the requirement that the radial mode function R_m and its first

[2]The Bessel function of the second kind is also sometimes called the Neuman function N_m.

derivative must be continuous across the interface at $r = R_c$, which yields the two conditions

$$AJ_m(aR_c) = BK_m(bR_c), \tag{2.18a}$$
$$AaJ'_m(aR_c) = BbK'_m(bR_c), \tag{2.18b}$$

where the prime denotes differentiation with respect to r. Using the recursion relations for the Bessel functions

$$xJ'_m(x) = xJ_{m-1}(x) - mJ_m(x), \tag{2.19a}$$
$$xK'_m(x) = -xK_{m-1}(x) - mK_m(x), \tag{2.19b}$$

the two conditions in Eqs. (2.18) can be combined into a single equation

$$\frac{aJ_{m-1}(aR_c)}{J_m(aR_c)} = -\frac{bK_{m-1}(bR_c)}{K_m(bR_c)}. \tag{2.20}$$

Since a and b are given by the effective index n_{eff}, Eq. (2.20) can be solved for n_{eff} for a given m. As we shall see, the equation may have no solution or a number of solutions depending on the SIF parameters and frequency of the electromagnetic field. Although Eq. (2.20) is transcendental and thus must be solved numerically, a cutoff condition for the guided modes can be found by considering the asymptotic behavior of the solution as $r \to \infty$. For modes of order m this cutoff criterion is [17]

$$J_{m-1}(V) = 0, \tag{2.21}$$

where the V parameter is defined as

$$V = \frac{2\pi R_c}{\lambda}\sqrt{n_c^2 - n_{cl}^2} = \frac{2\pi R_c}{\lambda}NA, \tag{2.22}$$

where NA is the numerical aperture (NA), which gives the largest angle of incidence that will lead to TIR in a ray-optics picture of the fiber. We see that V is proportional to the frequency of the electromagnetic field, and as V increases additional guided modes appear. The mode with the highest n_{eff} is called the fundamental mode (FM), and all other guided modes, which have lower effective indices, are called higher-order modes (HOMs). For the SIF the modes are labeled LP_{ml} where LP stands for *linearly polarized* to emphasize that we are working under the scalar approximation in which all modes are linearly polarized in the same direction. The index l labels the modes for a given m with the number of nodes of the radial mode function R_{ml} of the mode being $l - 1$. The cutoff values of the V parameter for the first few modes

LP_{ml}	$m=0$	$m=1$	$m=2$	$m=3$
$l=1$	0	2.4048	3.8317	5.1356
$l=2$	3.8317	5.5201	7.0156	8.4172
$l=3$	7.0156	8.6537	10.1745	11.6198
$l=4$	10.1735	11.7915	13.3237	14.7960

Table 2.1: Cutoff values of the V parameter for the LP_{ml} modes of a SIF.

are given in Table 2.1. We see that a SIF with $V < 2.4048$ supports only a single guided mode, namely the LP_{01} mode. An optical fiber which guides only the FM at a particular wavelength is said to be *single-mode*, while fibers supporting multiple guided modes are called *multimode*. From the definition of the V parameter given in Eq. (2.22) it is evident that increasing the core diameter and the index contrast will result in a higher V and hence eventually to multimode guidance.

In principle, the LP_{01} mode exists for any positive value of V. However, as guided modes becomes more confined to the core with increasing V, this mode will be very poorly confined if $V < 1$. The same is true for HOMs, which are poorly confined if the V parameter is only slightly above the cutoff value for the mode.

The modes are normalized according to

$$\int_0^{2\pi} \int_0^{\infty} \Psi_{ml}(r,\phi)^2 r \mathrm{d}r\mathrm{d}\phi = 1, \tag{2.23}$$

and also satisfy the orthogonality condition

$$\int_0^{2\pi} \int_0^{\infty} \Psi_{ml}(r,\phi)\Psi_{nk}(r,\phi) r \mathrm{d}r\mathrm{d}\phi = \delta_{mn}\delta_{lk}. \tag{2.24}$$

As an example, we consider the guided modes of a SIF with $V = 5$, $R_c = 20$ μm, $n_c = 1.45$ and a signal wavelength $\lambda = 1$ μm. From Table 2.1 we find that only the modes LP_{01}, LP_{11}, LP_{02} and LP_{21} are guided. The mode functions Ψ for these modes are plotted in Fig. 2.2.

2.2 The photonic crystal fiber

A revolutionary new type of optical fiber, known as a PCF, was invented by Knight *et al.* [18]. Rather than relying on doping of silica to achieve the necessary refractive index variation to provide the guiding properties of the fiber, a PCF obtains its light guiding properties by having a cladding typically

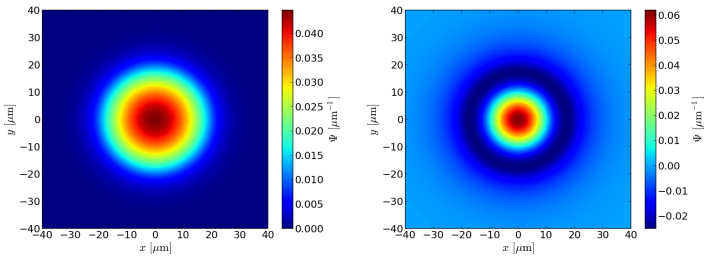

(a) LP_{01}

(b) LP_{02}

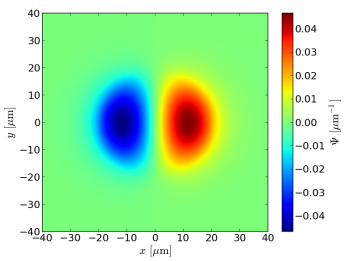

(c) LP_{11} cos

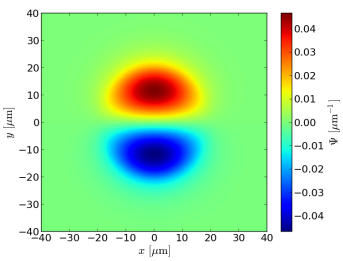

(d) LP_{11} sin

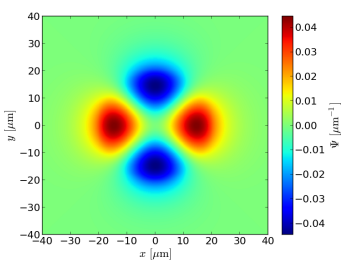

(e) LP_{21} cos

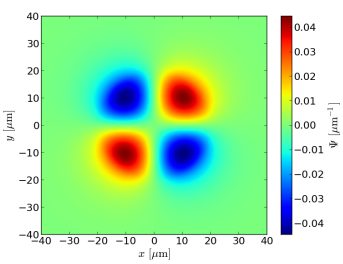

(f) LP_{21} sin

Figure 2.2: Guided modes of a SIF with $V = 5$, $R_c = 20$ μm, $n_c = 1.45$ and $\lambda = 1$ μm.

made up of a μm-scale periodic array of airholes in the silica matrix, with the core consisting of a central defect in this periodic array. As can be seen from the examples shown in Fig. 2.3, the possibilities for varying the structure of the cladding are enormous, and the PCF technology thus offers a design flexibility that greatly exceeds that of the traditional optical fibers. In addition to the

greater design flexibility, PCFs also possess a number of unique properties, which we shall discuss in the following. Since the focus of the work presented in this thesis is not directed explicitly at PCFs, the discussion given here will be brief and only discuss some basic features of this type of fiber.

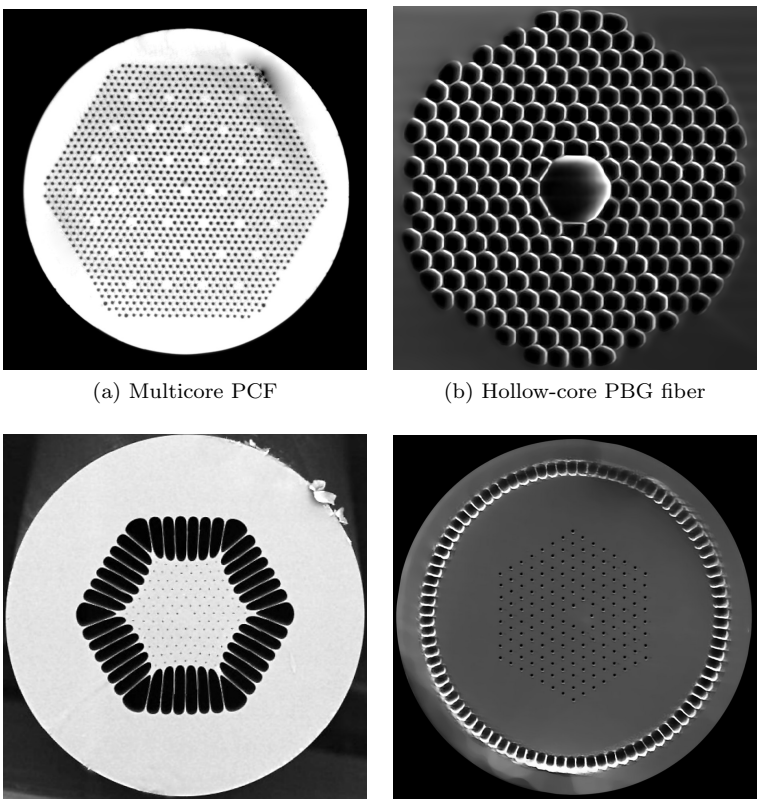

(a) Multicore PCF (b) Hollow-core PBG fiber

(c) Double-clad PCF (d) Double-clad PCF

Figure 2.3: Scanning electron microscope images of various PCF designs. Images courtesy of NKT Photonics A/S.

2.2.1 Manufacturing of photonic crystal fibers

PCFs are drawn using a draw-tower in much the same way that traditional fibers are drawn. The main difference lies in the creation of the fiber preform. A PCF preform is made by stacking together a number of cylindrical silica rods and capillary tubes into the desired pattern. In the case of active fibers, some of

the rods constituting the core are doped with an appropriate rare-earth element to provide the gain medium. The preform stack is then fused together in an intermediate drawing step, producing a number of so-called canes, which can then be drawn into the final PCF. Care must be taken during the production to prevent the collapse of the capillary tubes while at the same time collapsing the interstitial holes between the close-packed tubes.

2.2.2 Index guiding fibers

PCFs can be roughly divided into two categories, depending on the physical mechanism by which light is guided in the core. The first type, which we shall consider here, guides light by TIR as in traditional optical fibers, whereas the second type confines light to the core by the so-called photonic bandgap (PBG) effect. A PCF which guides light by TIR is also called an *index-guiding* PCF.

A particularly simple example of an index-guiding PCF is illustrated in Fig. 2.4. This fiber consists of a triangular array of airholes of diameter d and center-to-center hole distance Λ, which is known as the *pitch*. Both parameters have a profound impact on the optical properties of the fiber, such as the dispersion and the number and characteristics of guided modes, and can be varied a great deal. Calculating the guided modes of such a fiber requires numerical methods, such as the finite element method (FEM). However, it has been shown by Koshiba and Saitoh [19] that these simple PCFs are well approximated by an effective SIF model. In this model, the core has a refractive index equal to the refractive index of the glass matrix of the PCF and an *effective core radius* $R_{eff} = \Lambda/\sqrt{3}$, and is surrounded by an effective homogeneous cladding. The refractive index of this effective cladding is taken to be the effective index of the fundamental mode of the infinite periodic microstructure of the cladding without the core defect. This fundamental mode is also called the fundamental space-filling mode (FSM), and its effective mode index n_{FSM} depends on the hole diameter, pitch and wavelength of the light.

Analogous to the SIF considered in section 2.1, the V parameter for the effective SIF model of the PCF is given by

$$V_{PCF} = \frac{2\pi\Lambda}{\sqrt{3}\lambda}\sqrt{n_{SiO_2}^2 - n_{FSM}^2}. \tag{2.25}$$

With this definition, it was shown that the single-mode cutoff criterium for the simple PCF shown in Fig. 2.4 is $V_{PCF} < 2.4048$, the same as for a SIF. It was also shown that important mode properties such as effective index, dispersion and mode field diameter (MFD) are well approximated by the SIF model.

There is, however, a very important difference between the SIF and the PCF. In the SIF, the refractive index of the cladding n_{cl} is largely independent

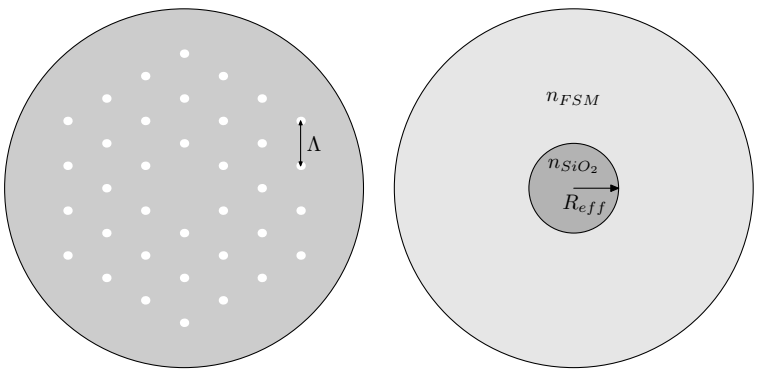

(a) Index-guiding PCF (b) Effective SIF model

Figure 2.4: (a) A simple index-guiding PCF consisting of a triangular array of airholes with a central defect core. (b) The SIF approximation to the PCF.

of the frequency of the light. As was discussed in section 2.1, this means that a SIF becomes multimode as the wavelength of the light decreases below a certain cutoff value. The situation is quite different in a PCF, since the effective index of the cladding n_{FSM} is strongly wavelength dependent. In the short wavelength limit $\lambda/\Lambda \ll 1$, the field of the fundamental mode of the infinite cladding structure is largely confined to the high-index silica matrix, avoiding the airholes. This implies that the effective index $n_{FSM} \to n_{SiO_2}$ in this limit. In the long wavelength limit $\lambda/\Lambda \gg 1$, the field of the fundamental mode of the cladding will be approximately uniform, and n_{FSM} will tend toward an area-weighted average of the refractive indices of air and silica. Let us now consider the behavior of V_{PCF} in the short wavelength limit. As mentioned above, the field of the fundamental space-filling mode of the cladding is essentially confined to the silica matrix, and we can therefore consider this mode to satisfy the scalar eigenvalue equation

$$\nabla_\perp^2 \Psi_{FSM} + n_{SiO_2}^2 k^2 \Psi_{FSM} = \beta_{FSM}^2 \Psi_{FSM}, \tag{2.26}$$

where $\beta_{FSM} = n_{FSM} k$ is the propagation constant of the fundamental space-filling mode. Multiplying Eq. (2.26) by Ψ_{FSM}^* and integrating over the transverse coordinates yields

$$n_{SiO_2}^2 - n_{FSM}^2 = \left(\frac{\lambda}{2\pi}\right)^2 \frac{\int |\nabla_\perp \Psi_{FSM}|^2 \, \mathrm{d}\mathbf{r}_\perp}{\int |\Psi_{FSM}|^2 \, \mathrm{d}\mathbf{r}_\perp}. \tag{2.27}$$

This means that in the short wavelength limit, $V_{PCF} \to \textit{constant}$ rather than diverging as in the SIF case. The limiting value of V_{PCF} is determined by

the ratio d/Λ, and if it is smaller than the cutoff value 2.4048, the PCF will be single-mode for all wavelengths. This has been found to be the case when $d/\Lambda < 0.42$. This very important property of PCFs is called *endlessly single-mode* guidance. If d/Λ exceeds the endlessly single-mode threshold of 0.42, the PCF will support multiple guided modes. Since the endlessly single-mode criterium depends only on the ratio d/Λ, it is possible to scale the pitch to quite large values, and thereby obtain single-mode fibers with a very large core diameter. As was discussed in section 2.1, the core diameter of a single-mode SIF is limited by the finite precision of the fiber manufacturing process, which limits the smallest achievable core-cladding index contrast. The fabrication of a large-pitch PCF is fairly straightforward, and it is therefore possible to produce single-mode fibers with larger cores using PCFs.

2.2.3 Photonic bandgap fibers

The guiding mechanism of so-called PBG fibers differ significantly from the essentially TIR guiding of the index-guiding PCFs. A PBG fiber utilizes the fact that a 2D periodic array of scatterers can prevent light propagation in the transverse direction for a certain frequency range, provided that the index contrast between the scatterers and the background material is sufficiently large [20]. This is known as a PBG. For airholes in a silica matrix, however, the index contrast is insufficient to create a PBG for both polarizations simultaneously. However, when we take propagation in the longitudinal direction into account, the air-silica index contrast is sufficient to create a PBG, provided that the propagation constant is large enough. Alternatively, we can say that for a given frequency, a certain range of propagation constants are not allowed. This means that a central defect in the periodic microstructure can confine light with a frequency and propagation constant that falls within the PBG.

Since the PBG fibers do not rely on TIR to confine the light, the refractive index of the core need not be greater than the refractive index of the surrounding cladding. PBG fibers are therefore ideal for creating hollow-core fibers, an example of which is shown in Fig. 2.3b. Since the light in such fibers is guided in air, the nonlinear optical effects are extremely small.

The scatterers in the cladding microstructure need not consist of airholes, but can also consist of high-index rods. The solid core then consists of a low-index defect. Such fibers thus have no airholes at all, which can facilitate handling and splicing. The inclusion of high-index rods in an otherwise index-guiding PCF design has also been used to fabricate a kind of hybrid between the index guiding PCF and the PBG fiber, where the PBG effect is utilized to suppress HOMs in the large-core fiber [21, 22].

As most active PCFs are based on index-guiding designs, we shall not dis-

cuss PBG fibers any further in this thesis.

2.3 Active fibers and ytterbium doping

Optical fibers can be turned into lasers and optical amplifiers by doping the fiber core with atoms which have a transition at the desired frequency. A population inversion is created by optical pumping of these atoms, and the fiber can then amplify the signal. Traditionally, erbium (Er) has been used as dopant since it can provide gain at the telecom band at 1550 nm, but more recently, other rare-earth elements such as neodymium (Nd) [23], ytterbium (Yb) [24] and thulium (Tm) [25] have been used. Since the work presented in this thesis concerns Yb-doped fibers, we shall restrict the discussion to this dopant only. Furthermore, the brief discussion presented here serves only as an introduction to the more detailed work presented in chapter 3.

To ensure excellent beam quality, the signal should preferably be guided in the FM of the fiber, but no such requirement exist for the pump light. In fact, since the pump light is often provided from high-power, low-brightness sources, it can be difficult to ensure efficient coupling of the pump light into the low-NA fiber core. For this reason, a so-called *double-clad* design, an example of which is shown in Fig. 2.3d, can be used to guide the pump light in an inner cladding surrounded by an outer cladding, which provides a high-NA waveguide into which the pump light is efficiently coupled. Since the pump waveguide in the double-clad fiber is highly multimode, the transverse profile of the pump light will be fairly uniform and can therefore efficiently pump the rare-earth dopants in the core, providing gain for the signal.

2.3.1 Energy states of ytterbium

When rare-earth ions are used as dopants in silica fibers, their partially filled $4f$ orbitals do not participate in the bonding to the silica host and hence energy levels of this orbital are well defined and have long lifetimes [17]. When Yb is used as a dopant in silica, it is in the form of the Yb^{3+} ion, which has 13 electrons out of the 14 possible in the $4f$ orbital. This makes for a very simple energy level diagram, which is illustrated in Fig. 2.5 [26, 27].

The states of the ground state manifold $^2F_{7/2}$ and the excited state manifold $^2F_{5/2}$ are split by Stark shifts due to interaction with the silica host and are labeled a through d for the ground state manifold, while the 3 energy states of the excited state manifold are labeled e through g. The optical transitions between the individual states of the ground and excited state manifolds can then be used for lasing. Experimental values for the absorption and emission cross sections are plotted in Fig. 2.6. The sharp peak at 975 nm in both the

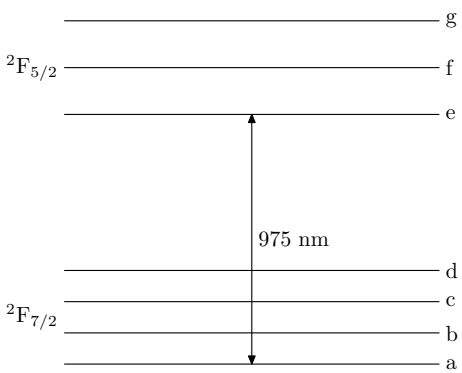

Figure 2.5: Energy level diagram of the Yb^{3+} ion. The degeneracy of the ground and excited state manifolds is lifted by the Stark effect caused by the silica host.

absorption and emission spectra is due to transitions between the lowest levels in the ground state and excited state manifolds, labeled a and e in Fig. 2.5. This line is quite narrow due to the long radiative lifetime of the excited state, which is about 0.85 ms. The broad emission peak around 1030 nm is due to transitions from state e to the higher states of the ground state manifold, labeled b, c and d. These states decay to the ground state a by rapid non-radiative transitions. It is thus clear that it should be possible to achieve gain at wavelengths in a broad range from around 1 μm to 1.2 μm by optical pumping of the fiber at 975 nm. This is indeed perhaps the most used pumping configuration used with Yb-doped fiber lasers. Furthermore, we identify the broad peak in the absorption spectrum around 915 nm with transitions from the ground state a to the higher states of the excited state manifold, labeled f and g, which permits gain at shorter wavelengths to be obtained.

Regardless of which pumping scheme is employed, the signal wavelength must always be greater than the pump wavelength. In the amplification process, pump photons are converted into signal photons of lower energy. This energy discrepancy, also known as the *quantum defect*, is carried away by phonons in the silica host and hence converted into heat. Since the refractive index of silica is sensitive to temperature, this quantum defect heating leads to a thermal nonlinear effect in rare-earth doped fiber amplifiers. As we shall see later, this effect can have a profound impact on the performance of such amplifiers. Compared to other rare-earth dopants, Yb has a relatively small quantum defect and is therefore well-suited for high average power fiber amplifiers.

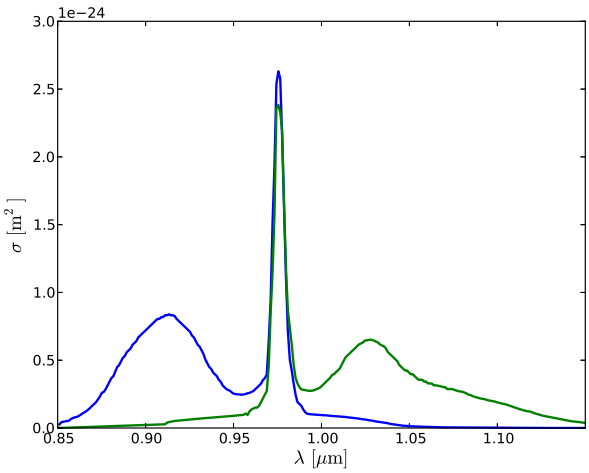

Figure 2.6: Absorption (blue curve) and emission (green curve) cross section of Yb-doped silica. Data courtesy of NKT Photonics A/S.

2.3.2 Rate equations and gain

The dynamics of the Yb ions can be modelled by the rate equations

$$\frac{\partial N_{7/2}}{\partial t} = -\left(\sigma_{ap}\Phi_p + \sigma_{as}\Phi_s\right) N_{7/2} + \left(\sigma_{ep}\Phi_p + \sigma_{es}\Phi_s + \gamma\right) N_{5/2}, \tag{2.28a}$$

$$\frac{\partial N_{5/2}}{\partial t} = \left(\sigma_{ap}\Phi_p + \sigma_{as}\Phi_s\right) N_{7/2} - \left(\sigma_{ep}\Phi_p + \sigma_{es}\Phi_s + \gamma\right) N_{5/2}, \tag{2.28b}$$

where $N_{7/2}$, $N_{5/2}$ are the densities of Yb ions in the ${}^2\mathrm{F}_{7/2}$ and ${}^2\mathrm{F}_{5/2}$ manifolds, respectively, Φ_p and Φ_s denote the photon flux density of the pump and signal fields, σ_{ap}, σ_{ep} are the absorption and emission cross sections of Yb at the pump wavelength, while σ_{as} and σ_{es} are the corresponding quantities at the signal wavelength. The spontaneous emission rate of the ${}^2\mathrm{F}_{5/2}$ manifold is denoted by γ.

When the pump and signal power changes only slowly with time, the solution to Eqs. (2.28) can be approximated by the steady-state solution, which is obtained by setting the time derivatives equal to zero

$$N_{5/2} = \frac{\left(\sigma_{ap}\Phi_p + \sigma_{as}\Phi_s\right) N_{Yb}}{\left(\sigma_{ap} + \sigma_{ep}\right)\Phi_p + \left(\sigma_{as} + \sigma_{es}\right)\Phi_s + \gamma}, \tag{2.29}$$

where $N_{Yb} = N_{7/2} + N_{5/2}$ is the total density of Yb ions.

The photon flux density of the signal satisfies the rate equation

$$\frac{\partial \Phi_s}{\partial z} = \left(N_{5/2}\sigma_{es} - N_{7/2}\sigma_{as} \right) \Phi_s(z) = g\Phi_s(z), \tag{2.30}$$

where the *gain coefficient* is given by

$$g = N_{5/2}\sigma_{es} - N_{7/2}\sigma_{as}. \tag{2.31}$$

From Eq. (2.30) we see immediately that a positive value of g leads to amplification of the signal, and that this requires a certain minimum population of the excited state manifold $^2\mathrm{F}_{5/2}$, which depends on the signal wavelength. Assuming fixed populations in the ground and excited state manifolds leads to a constant gain coefficient, and the solution to Eq. (2.30) is the simple exponential growth

$$\Phi_s(z) = \Phi_s(0)e^{gz}. \tag{2.32}$$

However, from the steady-state solution of the rate equations, given by Eq. (2.29), we see that the population densities themselves depend on the pump and signal power. As the signal power grows the excited state population falls, which is known as gain saturation. A more realistic treatment of Yb-doped fibers must thus solve the rate equations for the Yb ions in addition to the rate equations for the pump and signal.

2.4 Nonlinear effects in fibers

Up to now we have treated the material constituting the optical fiber as a *linear* dielectric, for which the induced polarization is proportional to the electric field. Although this is an excellent approximation for small field amplitudes, it fails when the field intensity becomes high enough. This gives rise to a host of *nonlinear optical* effects, which have many interesting and useful applications in fiber optics [28]. For rare-earth doped fiber lasers and amplifiers, however, these nonlinear effects lead to unwanted side effects which are detrimental to the power scalability of the system.

In this section we shall briefly review the most important nonlinear optical effects that limit the output power of fiber amplifiers. As we shall see, one obvious way of reducing the impact of nonlinear optical effects is to increase the area of the core. This leads to a larger MFD and hence a lower signal intensity, which reduces the strength of the nonlinear optical effects. This fact has motivated the development of large mode area (LMA) PCF amplifiers during the last decade.

2.4.1 The nonlinear induced polarization

In order to take nonlinear optical effects into account, we expand the dependence of the induced polarization $\mathbf{P}$ on the electric field E in a Taylor series, keeping terms to third order. In an isotropic material such as fused silica, the even order terms in the Taylor expansion must vanish due to the inversion symmetry of the material. We thus write the total induced polarization as

$$\mathbf{P}(\mathbf{r},t) = \mathbf{P}_L(\mathbf{r},t) + \mathbf{P}_{NL}(\mathbf{r},t), \tag{2.33}$$

where $\mathbf{P}_L$ is the usual linear induced polarization and $\mathbf{P}_{NL}$ is the nonlinear induced polarization. The latter is given by

$$P_{NL,i}(t) = \varepsilon_0 \iiint_{-\infty}^{\infty} R^{(3)}_{ijkl}(t-t_1, t-t_2, t-t_3) E_j(t_1) E_k(t_2) E_l(t_3) \mathrm{d}t_1 \mathrm{d}t_2 \mathrm{d}t_3 \tag{2.34}$$

where $R^{(3)}$ is the rank 4 tensor response function for the third order nonlinear induced polarization, the indices i, j, k, l refer to cartesian components of the tensor and vectors and summation over repeated indices is implied. Note that although we are considering an isotropic medium, the third order nonlinear response tensor need not be diagonal.

The motion of the electrons and the nuclei that constitute a silica molecule both contribute to the nonlinear response, with the vibrational motion of the nuclei being responsible for the duration of the response. Typical response times for fused silica glass used in fibers is around 65 fs, and for signal pulses with a significantly longer duration, the response function $R^{(3)}$ can be treated as effectively instantaneous, i.e.

$$R^{(3)}_{ijkl}(\tau_1, \tau_2, \tau_3) \approx \chi^{(3)}_{ijkl} \delta(\tau_1) \delta(\tau_2) \delta(\tau_3), \tag{2.35}$$

where $\chi^{(3)}$ is the third order nonlinear susceptibility. This leads to the following expression for the nonlinear induced polarization

$$P_{NL,i}(\mathbf{r},t) \approx \varepsilon_0 \chi^{(3)}_{ijkl} E_j(\mathbf{r},t) E_k(\mathbf{r},t) E_l(\mathbf{r},t). \tag{2.36}$$

This approximate form of the nonlinear induced polarization describes many effects such as self-phase modulation (SPM), third-harmonic generation (THG) and four-wave mixing (FWM). Because we have neglected the effect of the finite duration of the nonlinear response, it does not describe effects that are caused by molecular vibrations, such as stimulated Raman scattering (SRS).

Inserting Eq. (2.36) into Eq. (2.3) and assuming that the x-polarized electric field in the fiber can be written as

$$\mathbf{E}(\mathbf{r},t) = \frac{1}{2}\mathbf{x}\left(\Psi(\mathbf{r}_\perp) A(z,t) e^{i(\omega_0 t - \beta_0 z)} + c.c.\right), \tag{2.37}$$

where Ψ is the mode function for the FM, it is possible to derive a wave equation for the slowly-varying complex amplitude A [28]

$$\frac{\partial A}{\partial z} + \frac{\alpha}{2}A(z,T) + \frac{i}{2}\beta_2\frac{\partial^2 A}{\partial T^2} = i\gamma\left|A(z,T)\right|^2 A(z,T). \tag{2.38}$$

Here α describes fiber loss (or, if $\alpha < 0$, gain), and we have made the coordinate transformation $T = t - \beta_1 z$. The frequency dependent propagation constant of the FM has been expanded in a Taylor series about the carrier frequency ω_0

$$\beta(\omega) \approx \beta_0 + (\omega - \omega_0)\beta_1 + \frac{1}{2}(\omega - \omega_0)^2\beta_2, \tag{2.39}$$

where

$$\beta_n = \frac{\mathrm{d}^n\beta}{\mathrm{d}\omega^n}(\omega_0). \tag{2.40}$$

β_0 is the propagation constant at ω_0, $\beta_1 = v_g^{-1}$ gives the group velocity of the pulse described by the envelope function $A(z,T)$ and β_2 is a measure of the group-velocity dispersion (GVD). The *nonlinear parameter* γ is given by

$$\gamma = \frac{n_2\omega_0}{cA_{eff}}, \tag{2.41}$$

where the nonlinear-index coefficient n_2 is given in terms of the third order susceptibility $\chi^{(3)}$ and the linear refractive index n as

$$n_2 = \frac{3}{8n}\mathrm{Re}\left(\chi^{(3)}_{xxxx}\right), \tag{2.42}$$

and the *effective mode area* A_{eff} is defined by

$$A_{eff} = \frac{\left(\iint \left|\Psi(\mathbf{r}_\perp)\right|^2 \mathrm{d}^2\mathbf{r}_\perp\right)^2}{\iint \left|\Psi(\mathbf{r}_\perp)\right|^4 \mathrm{d}^2\mathbf{r}_\perp}. \tag{2.43}$$

It is clear from Eq. (2.38) that γ determines the strength of the nonlinearity. The nonlinear-index coefficient n_2 is a material parameter, which for fused silica is 2.6×10^{-20} m^2/W. The effective mode area on the other hand can vary a great deal depending on fiber core diameter. In particular, it is obvious that a large effective mode area leads to a small nonlinear parameter and hence to reduced nonlinear optical effects.

In the special case of zero loss or gain ($\alpha = 0$), Eq. (2.38) is known as the nonlinear Schrödinger equation and is a quite general equation for wave phenomena in which dispersion and nonlinearity is taken into account to lowest order.

2.4.2 Self-phase modulation

One of the most limiting nonlinear optical effects for pulsed fiber amplifiers is SPM [29]. As we shall see, the nonlinear term in Eq. (2.38) leads to an intensity dependent variation of the phase of the electric field, which results in spectral broadening of the pulses. For sufficiently long pulses of high peak power, the GVD term in Eq. (2.38) can be neglected. The solution to the nonlinear Schrödinger equation in this case is then given by [28]

$$A(L,T) = A(0,T)e^{-\alpha L/2}\exp\left(i\Phi_{NL}(L,T)\right), \tag{2.44}$$

where the *nonlinear phase* is given by

$$\Phi_{NL}(L,T) = \gamma L_{eff}\left|A(0,T)\right|^2. \tag{2.45}$$

The *effective length* L_{eff} for a fiber of length L is defined by

$$L_{eff} = \frac{1-e^{-\alpha L}}{\alpha}. \tag{2.46}$$

From the solution given in Eq. (2.44) we see that the phase of the electric field changes with time due to the changing field amplitude. The maximum phase shift Φ_{max} occurs at the peak of the pulse and is given by

$$\Phi_{max} = \gamma P_0 L_{eff}, \tag{2.47}$$

where P_0 is the peak power of the pulse. The temporally varying phase leads to a temporally varying instantaneous frequency of the light. Assuming a Gaussian pulse envelope with an initial spectral width of $\Delta\omega_0$, this frequency chirp leads to spectral broadening of the pulse. The magnitude of this spectral broadening, as measured by the root-mean-square width of the pulse spectrum, is given by [28]

$$\frac{\Delta\omega(L)}{\Delta\omega_0} = \sqrt{1+\frac{4\Phi_{max}^2}{3\sqrt{3}}}, \tag{2.48}$$

where $\Delta\omega(L)$ is the spectral width of the output pulse. From this result, it is clear that in order to avoid the SPM induced spectral broadening, fibers with very large cores can be utilized, as this leads to a reduction of the nonlinear parameter γ.

2.4.3 Stimulated Raman scattering

As mentioned earlier, the vibrational motion of the nuclei constituting the SiO_2 molecules in fused silica glass also contributes to the nonlinear response

of the material. Two-photon transitions between the ground state and excited vibrational states of the molecule, in which a photon from a strong pump field is absorbed and a photon is emitted into a lower-frequency Stokes field, is known as Raman scattering. If the process is stimulated, i.e. if the Stokes field is present alongside the pump, the process is called SRS.

In the continuous wave (CW) or quasi-CW regime, where effects of dispersion and the group velocity difference between the pump and Stokes fields can be neglected, the SRS process can be described by the simple set of coupled differential equations for the pump and Stokes intensity [28]

$$\frac{\partial I_s}{\partial z} = g_R(\Omega) I_p I_s - \alpha_s I_s, \tag{2.49a}$$

$$\frac{\partial I_p}{\partial z} = -\frac{\omega_p}{\omega_s} g_R(\Omega) I_p I_s - \alpha_p I_p. \tag{2.49b}$$

In Eqs. (2.49) $I_{s,p}$ are the Stokes and pump intensities, $\omega_{s,p}$ the corresponding angular frequencies and $\alpha_{s,p}$ account for fiber losses or gain at the Stokes and pump frequencies. The Raman gain coefficient g_R determines the strength of the SRS process and depends on the frequency difference $\Omega = \omega_p - \omega_s$. For copolarized pump and Stokes fields, the gain spectrum has a broad peak around $\Omega/2\pi \approx 13$ THz, and for a pump wavelength of 1 μm has the peak value $g_{R,max} \approx 10^{-13}$ m/W.

Under the assumption of negligible pump depletion, Eqs. (2.49) have the approximate solution

$$I_p(L) = I_p(0) \exp\left(-\alpha_p L\right), \tag{2.50a}$$

$$I_s(L) = I_s(0) \exp\left(g_R I_p(0) L_{eff} - \alpha_s L\right), \tag{2.50b}$$

where L_{eff} is given by Eq. (2.46) with $\alpha = \alpha_p$. From this solution we see that the Stokes intensity grows exponentially with input pump power, provided that a small amount of Stokes light is present at the input. In reality, this "seeding" of the Stokes field is provided by spontaneous Raman scattering, which is always present. As the Stokes field power increases, the pump will eventually become depleted and the approximate solution given by Eqs. (2.50) becomes invalid.

In the context of rare-earth doped fiber amplifiers, it is now clear that the amplified signal can act as a pump in the SRS process, resulting in a loss of signal at the desired wavelength and a buildup of power in the Stokes field. Defining the Raman threshold as the input pump power $P_{R,th}$ at which the output pump and Stokes powers are equal, Smith [30] derived the following expression for the Raman threshold

$$P_{R,th} = \frac{16 A_{eff}}{g_{R,max} L_{eff}}. \tag{2.51}$$

From this expression we see immediately that a larger effective mode area leads to a higher threshold power for SRS. As with SPM, this fact motivates the design of LMA fibers. However, other means of suppressing SRS besides scaling up the core exists. Since SRS involves the generation of a new frequency component, various "filtering" techniques can also be employed, in which the modes of the Stokes field are highly delocalized from the core [31, 32].

2.4.4 Stimulated Brillouin scattering

Another important nonlinear process which leads to the generation of a redshifted Stokes component from a stronger pump field is stimulated Brillouin scattering (SBS). Unlike SRS however, the pump and Stokes fields involved in SBS do not interact through the vibrational states of the individual molecules of the fiber material, but rather through the effect known as *electrostriction*. The interference pattern created by the pump and Stokes fields creates an acoustic wave in the fiber through this effect, and the density variation associated with this wave results in a moving refractive index grating. This index grating can in turn scatter the pump light by Bragg diffraction. The scattered light is redshifted due to the Doppler effect associated with the moving index grating, resulting in amplification of the Stokes field. Due to the dispersion relation obeyed by the acoustic wave, the pump light is scattered almost exclusively in the backward direction, unlike SRS which can scatter light in both the forward and backward direction.

In the case of a CW electric field, the intensities of the pump and Stokes components obey a set of coupled differential equations very similar to the equations governing SRS

$$\frac{\partial I_p}{\partial z} = -g_B(\Omega) I_p I_s - \alpha I_p, \tag{2.52a}$$

$$-\frac{\partial I_s}{\partial z} = g_B(\Omega) I_p I_s - \alpha I_s, \tag{2.52b}$$

where we have assumed $\omega_s \approx \omega_p$ and equal loss coefficients α for both pump and Stokes fields. This is justified because of the much smaller frequency shift associated with SBS compared to SRS. If we assume a simple model for the Brillouin gain, in which the acoustic wave decays as $\exp(-\Gamma_B t)$, the gain spectrum has the simple Lorentzian form

$$g_B(\Omega) = \frac{g_{B,max}(\Gamma_B/2)^2}{(\Omega - \Omega_B)^2 + (\Gamma_B/2)^2}, \tag{2.53}$$

where Γ_B^{-1} is the acoustic phonon lifetime and the Brillouin shift is given by

$$\Omega_B = \frac{4\pi v_a n_{eff,p}}{\lambda_p}. \tag{2.54}$$

Here v_a is the acoustic velocity of the fiber material, $n_{eff,p}$ is the effective mode index of the pump and λ_p is the pump wavelength. A typical value for the Brillouin shift is $\Omega_B/2\pi \approx 11$ GHz at $\lambda_p = 1.55$ μm. The width of the Brillouin gain is given by Γ_B and varies with fiber material and design, but can exceed 100 MHz at $\lambda_p = 1.55$ μm [28]. A typical value for the peak Brillouin gain is $g_{B,max} \approx 5 \times 10^{-11}$ m/W, which is about 500 times larger than the peak Raman gain.

A Brillouin threshold pump power $P_{B,th}$ can be calculated in the same manner as for SRS [30]

$$P_{B,th} = \frac{21 A_{eff}}{g_{B,max} L_{eff}}. \tag{2.55}$$

Due to the much larger peak value of the SBS gain compared to the SRS gain, the SBS threshold calculated from Eq. (2.55) is almost 3 orders of magnitude smaller than the corresponding SRS threshold calculated from Eq. (2.51). However, it should be kept in mind that the SBS threshold given by Eq. (2.55) is derived for quasi-CW light with a linewidth smaller than the width of the Brillouin gain spectrum. For pulses or CW fields with a spectral width larger than the width of the Brillouin gain spectrum, the Brillouin gain is substantially reduced, and the SBS threshold can become higher than the SRS threshold [28].

As with SPM and SRS, the unwanted effects of SBS can be mitigated by increasing the effective mode area. However, a number of other mitigation techniques exists for SBS. For CW operation in which a narrow linewidth of the signal is not required, the linewidth of an otherwise narrowband input signal can be broadened by modulation of the phase prior to amplification in the rare-earth doped fiber [33]. Other techniques involve manipulating the acoustic properties of the fiber to reduce the SBS threshold [34].

Chapter 3

Circularly symmetric beam propagation method

Recent development in high-power Yb-doped fiber amplifiers have lead to significant increases in operating power, and CW output power of a few kW has been demonstrated [35, 36]. Although Yb-doped fiber amplifiers have excellent heat dissipation properties owing to the large surface-to-volume ratio of the fiber, as we discussed in chapter 2, significant heating of the core occurs during high average power operation due to the quantum defect associated with the gain medium. Previous work has investigated the heat dissipation mechanism [12] and the effect of a specified thermal load on the transverse mode properties of fiber lasers and amplifiers [10, 13], and recent publications have discussed limiting factors for the power-scalability of fiber amplifiers, such as SPM in high peak power pulsed systems [29] and TMI issues at high average power [14, 15, 16]. Numerical studies have suggested that the latter effect is due to either thermal or population inversion induced coupling between the FM and a HOM of a multimode fiber [37, 38].

In this chapter we present a numerical model, based on a BPM, that includes the nonlinear interaction between the temperature distribution generated by the signal gain and the transverse field profile, which is influenced by the temperature induced change in refractive index. We have used this model to study the thermo-optical effects in LMA SIF amplifiers under high-power operation. In particular, we focus on two effects related to the above mentioned scalability limitations: The thermal lensing effect, which leads to beam self-focusing and hence to increased SPM, and an effective multimode behavior which can occur at high average power even in fibers which are single-mode by design. Contrary to the investigations of Jauregui *et al.* [37] and Smith *et al.* [38], we focus

on single-mode fibers and show that the thermal effect in itself is sufficient to induce a multi-moded behavior.

Many state-of-the-art rare-earth doped fiber amplifiers are based on PCFs, the simulation of which require computationally demanding full 3D BPM codes. In order to make the calculations less demanding, we have chosen to model SIFs, but since simple index-guiding PCFs are well approximated by an effective SIF model, as we discussed in chapter 2, we expect our results to be applicable to such fibers as well.

The chapter is organized as follows: In section 3.1 we describe the details of our numerical model, and discuss advantages and limitations. In section 3.2 we present the results of our numerical investigation of the thermo-optical effect for various fiber design parameters, and discuss the implications for the design of high-power fiber amplifiers.

3.1 Beam propagation method

Our BPM algorithm simulates double-clad Yb-doped SIF amplifiers. Since we will deal mainly with single-mode fibers in this chapter, we can assume that the electromagnetic field of the signal is cylindrically symmetric. This drastically reduces the numerical complexity of the problem and leads to a very efficient numerical solution. This is particularly important for modeling backward pumped amplifiers, since the required initial condition for the pump power is not known a priori in this case, and thus requires the BPM code to be run iteratively to obtain the desired input pump power. This assumption, however, also imposes the limitation that we cannot consider an input beam profile which is shifted or tilted relative to the symmetry axis of the fiber. The method can be extended to handle non-symmetric cases by expanding the azimuthal dependence of the field in a Fourier series, which will be discussed in chapter 4.

3.1.1 Beam propagation equation

The electric field of the signal can be written

$$\mathbf{E}_s(\mathbf{r},t) = \mathbf{u}_s E_s(r,z) e^{i(\beta z - \omega_s t)} + c.c., \tag{3.1}$$

where $\mathbf{u}_s$ is the polarization unit vector, E_s is the slowly varying envelope of the signal field, β is an estimate of the propagation constant of the FM and ω_s is the carrier angular frequency of the signal. In the scalar approximation, the

field envelope E_s obeys the paraxial wave equation

$$\frac{\partial E_s}{\partial z} = \frac{i}{2\beta}\left[\frac{\partial^2 E_s}{\partial r^2} + \frac{1}{r}\frac{\partial E_s}{\partial r} + \left(k_0^2\left[\varepsilon(r) + \Delta\varepsilon(r,z)\right] - \beta^2\right)E_s + \mu_0\omega_s^2 p\right]. \quad (3.2)$$

The first terms on the right hand side of Eq. (3.2) describe the propagation of the signal field, with vacuum wavenumber $k_0 = \omega_s/c$, in a fiber with a relative permittivity distribution given by ε. The perturbation of this permittivity distribution due to heating of the core is given by $\Delta\varepsilon$. The last term describes the effect of the Yb doping, which gives rise to an induced polarization $\mathbf{P}_{Yb}$ given by a slowly varying envelope p as

$$\mathbf{P}_{Yb}(\mathbf{r},t) = \mathbf{u}_s p(r,z) e^{i(\beta z - \omega_s t)} + c.c. \quad (3.3)$$

3.1.2 Density matrix and rate equations

We assume that the fiber is cladding pumped at a wavelength of 975 nm and that the signal wavelength is close to 1030 nm. In this case the Yb^{3+} ions can be modeled as the quasi-three-level system shown in Fig. 3.1.

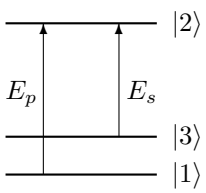

Figure 3.1: Simplified energy level diagram for Yb^{3+}.

The equations of motion for the slowly varying density matrix elements $\sigma_{\mu\nu}$ are [39]:

$$\dot{\sigma}_{11} = \frac{i}{\hbar}\left(\mu_{12}E_p^*\sigma_{21} - \text{c.c.}\right) + \gamma_{21}\sigma_{22} + \bar{\gamma}_{31}\sigma_{33} - \bar{\gamma}_{13}\sigma_{11} \quad (3.4a)$$

$$\dot{\sigma}_{22} = -\frac{i}{\hbar}\left(\mu_{12}E_p^*\sigma_{21} + \mu_{32}E_s^*\sigma_{23} - \text{c.c.}\right) - \left(\gamma_{23} + \gamma_{21}\right)\sigma_{22} \quad (3.4b)$$

$$\dot{\sigma}_{33} = \frac{i}{\hbar}\left(\mu_{32}E_s^*\sigma_{23} - \text{c.c.}\right) + \gamma_{23}\sigma_{22} - \bar{\gamma}_{31}\sigma_{33} + \bar{\gamma}_{13}\sigma_{11} \quad (3.4c)$$

$$\dot{\sigma}_{21} = \frac{i}{\hbar}\left(\mu_{12}^*E_p\left(\sigma_{11} - \sigma_{22}\right) + \mu_{32}^*E_s\sigma_{31}\right) - \tilde{\Gamma}_{21}\sigma_{21} \quad (3.4d)$$

$$\dot{\sigma}_{23} = \frac{i}{\hbar}\left(\mu_{32}^*E_s\left(\sigma_{33} - \sigma_{22}\right) + \mu_{12}^*E_p\sigma_{31}^*\right) - \tilde{\Gamma}_{23}\sigma_{23} \quad (3.4e)$$

$$\dot{\sigma}_{31} = \frac{i}{\hbar}\left(\mu_{32}E_s^*\sigma_{21} - \mu_{12}^*E_p\sigma_{23}^*\right) - \tilde{\Gamma}_{31}\sigma_{31}, \quad (3.4f)$$

where $\mu_{\mu\nu}$ are the matrix elements of the dipole moment operator, E_p is the pump field envelope, $\gamma_{\mu\nu}$ are spontaneous emission rates from state μ into state ν and the non-radiative transition rates are denoted $\bar{\gamma}_{\mu\nu}$. The complex dephasing rates $\tilde{\Gamma}_{\mu\nu}$ of the coherences are given by

$$\tilde{\Gamma}_{21} = \tilde{\gamma}_{21} - i\Delta_p \tag{3.5a}$$

$$\tilde{\Gamma}_{23} = \tilde{\gamma}_{23} - i\Delta_s \tag{3.5b}$$

$$\tilde{\Gamma}_{31} = \tilde{\gamma}_{31} - i\Delta_2, \tag{3.5c}$$

where $\tilde{\gamma}_{\mu\nu}$ are the real dephasing rates of the coherences $\sigma_{\mu\nu}$, $\Delta_p = \omega_p - \omega_{21}$ is the pump detuning, $\Delta_s = \omega_s - \omega_{23}$ is the signal detuning and $\Delta_2 = \Delta_p - \Delta_s$ is the two-photon detuning of the pump and signal. Since the dephasing rates $\tilde{\gamma}_{\mu\nu}$ in Eq. (3.4) are large, we can adiabatically eliminate the coherences [40], which leads to a rate equation for the excited state population

$$\dot{\sigma}_{22} = B_p(\Delta_p)|E_p|^2\left(\sigma_{11} - \sigma_{22}\right) + B_s(\Delta_s)|E_s|^2\left(\sigma_{33} - \sigma_{22}\right) - \left(\gamma_{23} + \gamma_{21}\right)\sigma_{22}, \tag{3.6}$$

where

$$B_p = \frac{2\tilde{\gamma}_{21}|\mu_{12}|^2}{\hbar^2\left(\tilde{\gamma}_{21}^2 + \Delta_p^2\right)} \quad \text{and} \quad B_s = \frac{2\tilde{\gamma}_{23}|\mu_{32}|^2}{\hbar^2\left(\tilde{\gamma}_{23}^2 + \Delta_s^2\right)}. \tag{3.7}$$

Analogous to the McCumber theory [41], we assume that the two lower states remain in thermal equilibrium. Denoting the total population of the two lower states as $\rho_1 = \sigma_{11} + \sigma_{33}$ and the excited state population as $\rho_2 = \sigma_{22}$, we arrive at a rate equation for the excited state population. In the steady-state, this equation becomes

$$\rho_2(r,z) = \frac{\sigma_{ap}\Phi_p(z) + \sigma_{as}\Phi_s(r,z)}{\left(\sigma_{ap} + \sigma_{ep}\right)\Phi_p(z) + \left(\sigma_{as} + \sigma_{es}\right)\Phi_s(r,z) + \gamma}, \tag{3.8}$$

where Φ_p and Φ_s denote the pump and signal photon flux density, respectively, and $\gamma = \gamma_{21} + \gamma_{23}$ is the total spontaneous emission rate of the excited state. In our simplified 3-level model, the absorption and emission cross sections at the signal wavelength, σ_{as} and σ_{es}, are given by

$$\sigma_{as}(\omega_s) = \frac{e^{-\Delta E/k_B T}}{1 + e^{-\Delta E/k_B T}}\frac{\hbar\omega_s B_s}{2\varepsilon_0 c n_c} \quad \text{and} \quad \sigma_{es}(\omega_s) = \frac{\hbar\omega_s B_s}{2\varepsilon_0 c n_c}, \tag{3.9}$$

while at the pump wavelength, the absorption and emission cross sections are

$$\sigma_{ap}(\omega_p) = \frac{1}{1 + e^{-\Delta E/k_B T}}\frac{\hbar\omega_p B_p}{2\varepsilon_0 c n_c} \quad \text{and} \quad \sigma_{ep}(\omega_p) = \frac{\hbar\omega_p B_p}{2\varepsilon_0 c n_c}. \tag{3.10}$$

Here ΔE is the energy difference between states 1 and 3.

The induced polarization at the signal wavelength is determined by the coherence σ_{23} and is given in terms of the signal field and population inversion as

$$p(r,z) = \frac{\varepsilon_0 n_c \rho_{Yb}(r)}{k_0} \left(i + \frac{\Delta_s}{\tilde{\gamma}_{23}} \right) \left[\sigma_{as} - (\sigma_{as} + \sigma_{es})\, \rho_2(r,z) \right] E_s(r,z), \quad (3.11)$$

where n_c is the core refractive index and ρ_{Yb} is the density of Yb^{3+} ions. As discussed in [37], this induced polarization can lead to a change in the refractive index which depends on the population inversion. In our simplified model this happens when the signal is detuned from resonance ($\Delta_s \neq 0$), and an estimate of the magnitude of this effect when $\Delta_s = \tilde{\gamma}_{23}/2$ and $\rho_2 = 0.5$ yields $\Delta\varepsilon \approx 10^{-6}$, which is quite small compared to the thermally induced changes in the refractive index. We therefore ignore this effect in our calculations.

Inserting Eq. (3.11) into Eq. (3.2) and assuming $|\Delta_s| \ll \tilde{\gamma}_{23}$ yields a beam propagation equation which includes the signal gain due to the Yb doping

$$\begin{aligned} \frac{\partial E_s}{\partial z} = {} & \frac{i}{2\beta} \left(\frac{\partial^2 E_s}{\partial r^2} + \frac{1}{r} \frac{\partial E_s}{\partial r} + \left(k_0^2 \left(\varepsilon + \Delta\varepsilon \right) - \beta^2 \right) E_s \right) \\ & + \frac{\sqrt{\varepsilon} k_0 \rho_{Yb}}{2\beta} \left(\sigma_{es} \rho_2 - (1 - \rho_2)\, \sigma_{as} \right) E_s. \end{aligned} \quad (3.12)$$

3.1.3 Split-operator method

The signal field can be propagated forward in z from an initial beam profile $E_s(0,r)$ using a split-operator approach

$$E_s(z + \Delta z, r) \approx \exp\left(\frac{\Delta z}{2} \hat{R} \right) \exp\left(\Delta z \hat{N} \right) \exp\left(\frac{\Delta z}{2} \hat{R} \right) E_s(z,r), \quad (3.13)$$

where the operators $\hat{R}$ and $\hat{N}$ are given by

$$\hat{R} E_s = \frac{i}{2\beta} \left(\frac{\partial^2 E_s}{\partial r^2} + \frac{1}{r} \frac{\partial E_s}{\partial r} \right), \quad (3.14)$$

$$\hat{N} E_s = \left[-\frac{\rho_{Yb}}{2} \sqrt{\frac{\varepsilon}{\varepsilon_{eff}}} \left(\sigma_{as} - (\sigma_{as} + \sigma_{es})\, \rho_2 \right) + \frac{i k_0^2}{2\beta} \left(\varepsilon + \Delta\varepsilon - \varepsilon_{eff} \right) \right] E_s, \quad (3.15)$$

and $\varepsilon_{eff} = \beta^2 / k_0^2$. The exponential of the $\hat{R}$ operator is approximated by the Padé approximant

$$\exp\left(\frac{\Delta z}{2} \hat{R} \right) \approx \frac{1 + \frac{\Delta z}{4} \hat{R}}{1 - \frac{\Delta z}{4} \hat{R}}. \quad (3.16)$$

The differential operators are discretized using a second order finite-difference scheme, and a transparent boundary condition [42] is applied at the outer surface of the fiber.

The input signal beam profile is taken to be the Gaussian

$$E_s(0,r) = \frac{P_s(0)}{\pi\varepsilon_0 c n_c w^2} e^{-r^2/w^2}, \tag{3.17}$$

where w is the characteristic radius of the input beam, which is chosen to be equal to the core radius, and $P_s(0)$ is the input signal power.

3.1.4 Thermal nonlinearity

To calculate the relative permittivity perturbation $\Delta\varepsilon$ due to heating of the fiber under high-power operation, we solve the steady-state heat equation under the assumption that the longitudinal temperature gradient is much smaller than the radial temperature gradient

$$\frac{\partial^2 \Delta T}{\partial r^2} + \frac{1}{r}\frac{\partial \Delta T}{\partial r} = -\frac{Q}{\kappa}. \tag{3.18}$$

Here ΔT is the temperature increase relative to the temperature of the coolant, κ is the thermal conductivity of the fiber and the thermal load Q is given by

$$Q = \rho_{Yb}\hbar\left(\omega_p - \omega_s\right)\left(\Phi_s\left(\sigma_{es}\rho_2 - \sigma_{as}\rho_1\right) + \gamma_{23}\rho_2\right), \tag{3.19}$$

where ω_p is the pump angular frequency. The first term in this expression represents heat generated by non-radiative relaxation following stimulated emission of signal photons and is the dominant heat source, whereas the last, much smaller, term is due to non-radiative relaxation following spontaneous emission at the signal wavelength. We assume uniform efficient water cooling of the fiber and thus apply a simple Dirichlet boundary condition $\Delta T = 0$ at the outer boundary when solving the heat equation. The temperature induced change of the refractive index of the fiber is given by the simple linear relationship $\Delta\varepsilon = \eta\Delta T$, where the thermo-optic coefficient[1] $\eta = 3.5 \times 10^{-5}$ K^{-1}.

3.1.5 Pump propagation equation

Since we are modeling cladding pumped fiber amplifiers, we assume that the pump intensity is constant over the core. We can thus model the propagation

[1] The thermo-optic coefficient is conventionally defined as $\Delta n = \eta\Delta T$. The non-standard definition used here is more convenient in this work.

of the pump by the simple ordinary differential equation

$$\frac{\mathrm{d}P_p}{\mathrm{d}z} = \pm\frac{2\pi}{A_{cl}} P_p(z) \int_0^{R_c} \rho_{Yb}(r) \left[(\sigma_{ap} + \sigma_{ep})\, \rho_2(r,z) - \sigma_{ap}\right] r \mathrm{d}r, \tag{3.20}$$

where P_p is the pump power, A_{cl} is the area of the inner cladding and R_c is the radius of the doped core. The positive sign applies to forward pumping whereas the negative sign applies to backward pumping. The pump power can thus be propagated in the z direction from its initial value $P_p(0)$ by the equation

$$P_p(z + \Delta z) \approx P_p(z) \pm \frac{2\pi}{A_{cl}} P_p(z) \Delta z \int_0^{R_c} \rho_{Yb} \left[(\sigma_{ap} + \sigma_{ep})\, \rho_2 - \sigma_{ap}\right] r \mathrm{d}r. \tag{3.21}$$

The BPM algorithm can be summarized by the following steps:

1. Compute the excited state population ρ_2 from Eq. (3.8).
2. Compute ΔT by solving Eq. (3.18) and calculate $\Delta\varepsilon$.
3. Propagate the signal field one step in z by applying Eq. (3.13).
4. Propagate the pump field one step in z by applying Eq. (3.21).

These steps are carried out until the signal has been propagated the desired distance. In the case of backward pumping an initial guess for the initial condition of the pump power $P_p(0)$ must be provided, and the entire BPM algorithm is run iteratively until the desired input pump power $P_p(L)$ is obtained. After each run the pump initial condition $P_p(0)$ is adjusted according to a simple secant method [43]. With a tolerance of 1% of the desired input pump power and a reasonable estimate of the pump initial condition, only a few iterations of the BPM algorithm are required.

3.2 Numerical results

We have used our numerical model to investigate two important effects of the radial thermal gradient produced in the fiber under high-power operation. The first effect is thermal lensing, which leads to focusing of the signal beam, and the second is the thermally induced multimode behavior of the amplifier. Although we are considering double-clad fibers, we have chosen to model the fibers as SIFs without the large index contrast associated with the pump cladding, and simply assume that the pump light is confined to a given inner cladding diameter. This is done in order to allow any signal radiation modes to escape the computational domain via the transparent boundary condition and thereby obtain an ideal

picture of the guided signal field. In actual double-clad fibers, these radiation modes would predominantly be cladding modes which can interfere with the guided signal, but since such cladding modes are only weakly amplified due to their small overlap with the Yb-doped core, their influence on the guided signal is small. In double-clad PCF amplifiers, the pump light is confined by large air holes. While it is not clear that such a structure can be adequately approximated by a step-index model, we believe that its influence on the guided signal is negligible, provided that the pump cladding diameter is sufficiently large to prevent a significant overlap between the guided signal and the air holes.

3.2.1 Thermal lensing

One of the main advantages of LMA fiber amplifiers is the lower intensity of the guided mode, which allows for a higher signal power before detrimental nonlinear effects such as SPM becomes a limiting factor. These effects are most important in pulsed operation where the peak power is high. Although our model assumes CW operation, we can use the model to estimate the thermal lensing effect induced during pulsed operation at high repetition rates. We quantify the thermal lensing effect by calculating the so-called B-integral as it has been demonstrated to give a useful estimate of the severity of nonlinear effects such as SPM [29]. It is given by

$$B = \frac{2\pi n_2}{\lambda_s} \int_0^L \frac{P_s(z)}{A_{eff}(z)} \mathrm{d}z, \tag{3.22}$$

where n_2 is the nonlinear refractive index of silica, P_s is the average signal power and A_{eff} is the effective area of the signal beam

$$A_{eff}(z) = 2\pi \frac{\left(\int_0^\infty |E(z,r)|^2 r \mathrm{d}r\right)^2}{\int_0^\infty |E(z,r)|^4 r \mathrm{d}r}. \tag{3.23}$$

We have simulated a 1 m long double-clad fiber amplifier, in the following referred to as Fiber A, with a core diameter of 40 μm, an inner cladding diameter of 200 μm and an outer diameter of 400 μm. The core-cladding index step is 10^{-4}, which gives $V \approx 2.08$ at the signal wavelength of 1030 nm, and the Yb density in the core is 10^8 $\mu\mathrm{m}^{-3}$. The fiber is cladding pumped at 975 nm, and we have varied the input pump power between approximately 50 W - 5 kW. The signal input power was kept fixed at 1 W, and both forward and backward pumping was simulated. Figure 3.2 shows the pump and signal power as a function of distance along the fiber for forward and backward pumping with 1 kW input pump power and 1 W input signal power. The pump is efficiently

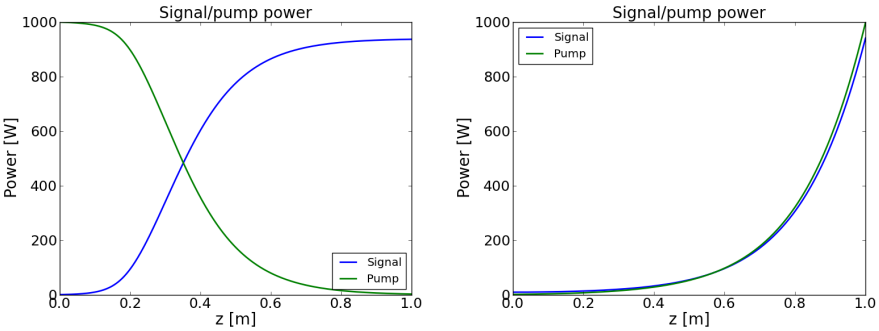

(a) Forward pumping (b) Backward pumping

Figure 3.2: Signal and pump power as a function of z for (a) forward pumping and (b) backward pumping of Fiber A.

depleted due to the high Yb doping which results in a high efficiency close to the quantum limit.

Figure 3.3 shows the excited state population ρ_2 of Yb as a function of longitudinal and radial distance for Fiber A at 1 kW pump power. The effect of transverse hole burning (THB) is clearly seen, especially in the backward pumped case.

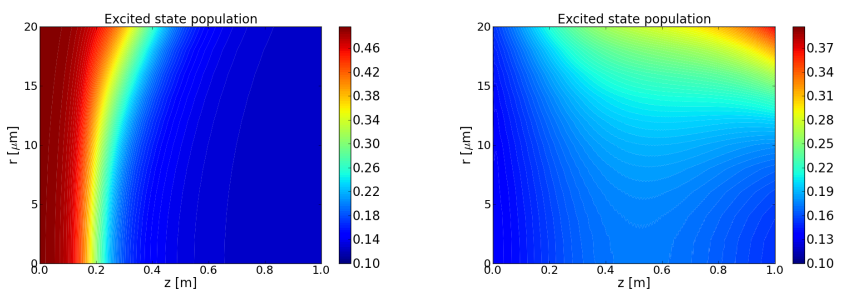

(a) Forward pumping (b) Backward pumping

Figure 3.3: Excited state population as a function of z and r for (a) forward pumping and (b) backward pumping of Fiber A at 1 kW pump power and 1 W input signal power.

The heating of the fiber occurs where the stimulated emission is largest.

This is clearly evident from Fig. 3.4, which shows the temperature increase as a function of z and r for Fiber A at 1 kW pump power. The heating of the core creates a large radial thermal gradient in the fiber, which leads to a thermal lensing effect that causes the beam area to decrease, as shown in Fig. 3.5. It is also clear from Fig. 3.4 that the temperature increase is much larger in the backward pumped case due to the large gain near the output end of the fiber.

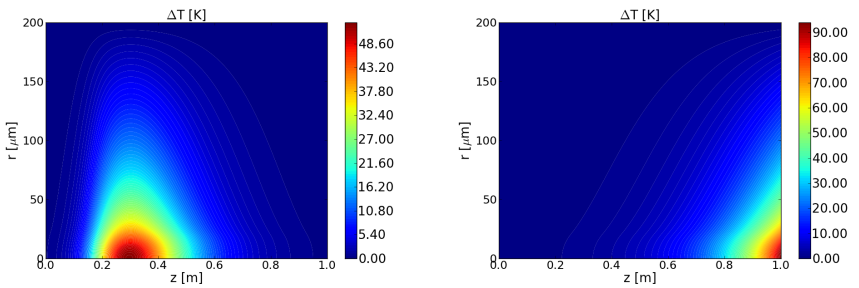

(a) Forward pumping (b) Backward pumping

Figure 3.4: Temperature increment as a function of z and r for (a) forward pumping and (b) backward pumping of Fiber A at 1 kW pump power and 1 W input signal power.

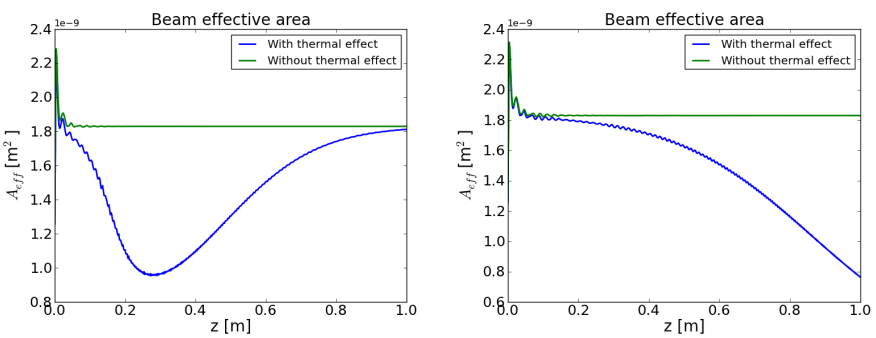

(a) Forward pumping (b) Backward pumping

Figure 3.5: Beam effective area as a function of z for (a) forward pumping and (b) backward pumping of Fiber A at 1 kW pump power and 1 W input signal power.

As is clear from Eq. (3.22), the self-focusing of the beam results in a higher value of the B-integral. In Fig. 3.6 we show the B-integral as a function of input pump power for both forward and backward pumped configurations. The dashed lines show the result when the thermal sensitivity η is set to zero. For comparison, we have also simulated a fiber (Fiber B), identical to Fiber A except that the core, inner cladding and outer diameters are 80 μm, 400 μm and 800 μm, respectively. It can be seen that as operating power on the order of 1

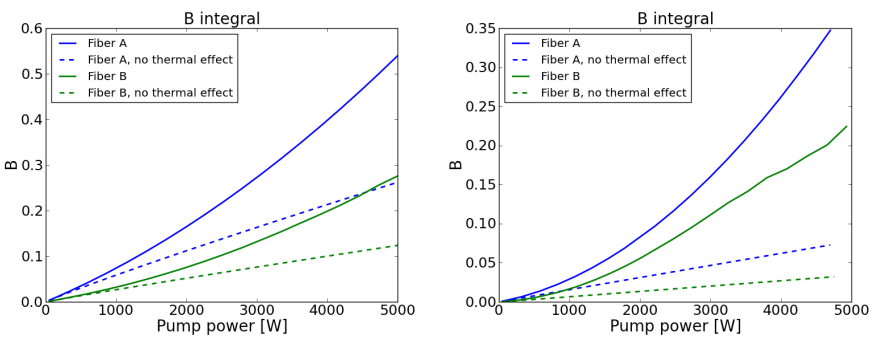

(a) Forward pumping (b) Backward pumping

Figure 3.6: B integral as a function of pump power for (a) forward pumping and (b) backward pumping of Fiber A and B with 1 W input signal power. The dashed lines show the results with the thermal sensitivity η set to zero.

kW is reached, the thermal lensing effect starts to have a significant impact on the beam area and hence the severity of undesirable non-linear optical effects such as SPM, in particular for the backward pumped case, which is preferred over the forward pumped case due to the overall lower value of the B-integral and hence smaller impact of the aforementioned effects. Furthermore, the thermal lensing effect changes the pump power dependence of the B integral from linear to super-linear. Comparing Fiber A to Fiber B, we see that the B integral for Fiber B, when the thermal lensing effect is taken into account, can exceed the expected B integral of Fiber A in the absence of thermal lensing, despite the fact that Fiber B has a core area 4 times larger than Fiber A. This occurs at a pump power of approximately 4.5 kW for forward pumping and 1 kW for backward pumping. However, it is also clear that even in the presence of a strong thermal lensing effect, increasing the core diameter still results in a significant reduction of the B integral and hence the severity of SPM.

3.2.2 Thermally induced multimode behavior

Another consequence of the thermally induced change in the refractive index of the fiber is that an otherwise single-mode fiber can be rendered effectively multimode. Such multimode behavior can have a negative impact on the output beam quality due to an uncontrollable drift of the relative phase between the excited modes [44]. It is also clear that the thermally induced multimode behavior will only occur beyond a certain power threshold, since the induced index change must be large enough to allow multiple guided modes to exist. Furthermore, once a HOM is excited, the beating between the FM and HOM will create a thermally induced grating in the fiber. As discussed in [37, 38], such a grating couples the two modes such that power may be transferred from the FM to the HOM.

Here we present the results of simulations that clearly show the above mentioned effects. We consider a 1 m long LMA SIF (Fiber C) with core, inner cladding and outer diameters of 80 μm, 400 μm and 800 μm, respectively. The index step between core and cladding is $\Delta n = 3 \times 10^{-5}$. While such a small index step is difficult to achieve in actual SIFs, it is obtainable using PCFs. The Yb density is 5×10^7 μm^{-3} and the pump and signal wavelength are 975 nm and 1030 nm. With these parameters, the V parameter for the SIF is 2.28 and the fiber is thus single-mode by design. The pump power is 5 kW and the input signal power is 50 W. Figure 3.7 shows the signal and pump power as a function of z for both forward and backward pumping. The lower Yb density compared to the simulations of Fiber A and B in section 3.2.1 reduces the efficiency of the amplifier. We also note the presence of small oscillations of the signal power near the output, which are likely due to excitation of radiation modes.

Considering the effective area of the beam as a function of z shown in Fig. 3.8, we observe strong oscillations of the effective area, which would not occur if the signal was guided by a single mode and which therefore are a direct consequence of thermally induced multimode behavior. These oscillations are also seen in the temperature, shown in Fig. 3.9, and the excited state population, shown in Fig. 3.10.

To provide additional insight into the nature of these oscillations, we decompose the signal field in local modes at each z position by solving the eigenvalue problem

$$\frac{\partial^2 \Psi}{\partial r^2} + \frac{1}{r}\frac{\partial \Psi}{\partial r} + k_0^2 \left[\varepsilon(r) + \Delta\varepsilon(r,z)\right] \Psi(r,z) = \beta^2(z)\Psi(r,z), \tag{3.24}$$

and computing the overlap between the normalized modes Ψ and the signal

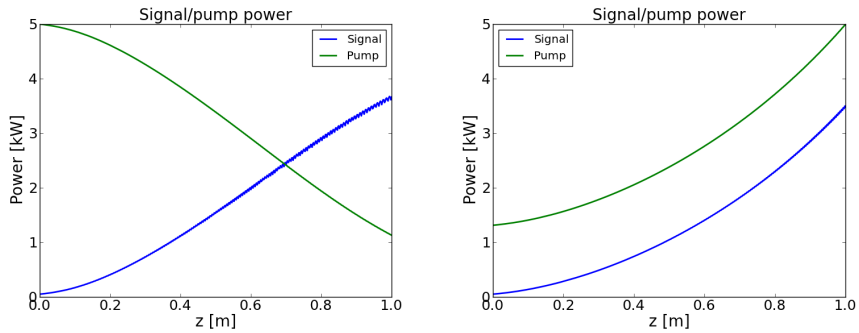

(a) Forward pumping (b) Backward pumping

Figure 3.7: Signal and pump power as a function of z for (a) forward pumping and (b) backward pumping of Fiber C.

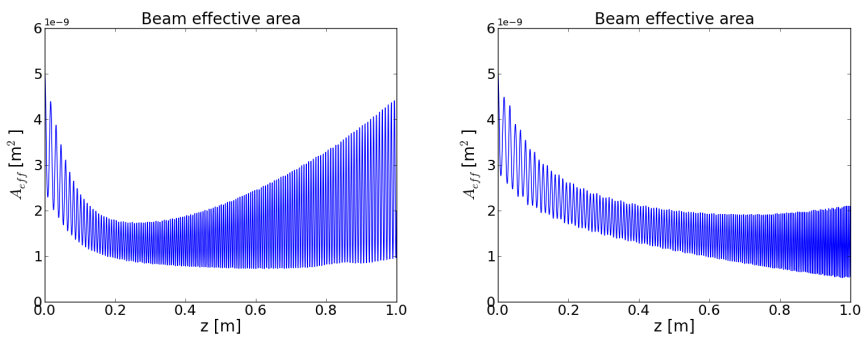

(a) Forward pumping (b) Backward pumping

Figure 3.8: Beam effective area as a function of z for (a) forward pumping and (b) backward pumping of Fiber C at 5 kW pump power and 50 W input signal power.

field. This overlap is given by

$$a_i(z) = \langle \Psi_i | E_s \rangle, \tag{3.25}$$

where the inner product is defined as

$$\langle \Psi | \Phi \rangle = \int_0^\infty \Psi^*(r)\Phi(r) r \mathrm{d}r. \tag{3.26}$$

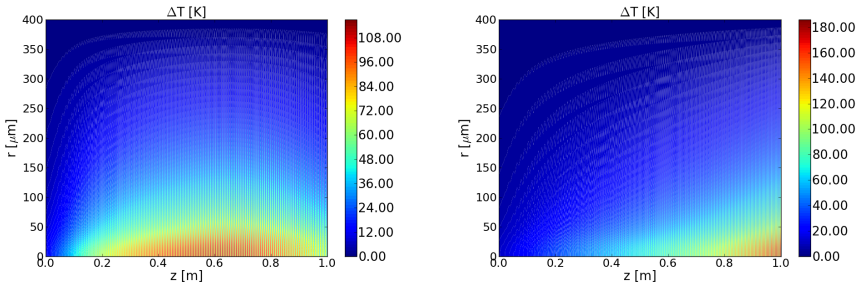

(a) Forward pumping (b) Backward pumping

Figure 3.9: Temperature increment as a function of z and r for (a) forward pumping and (b) backward pumping of Fiber C at 5 kW pump power and 50 W input signal power.

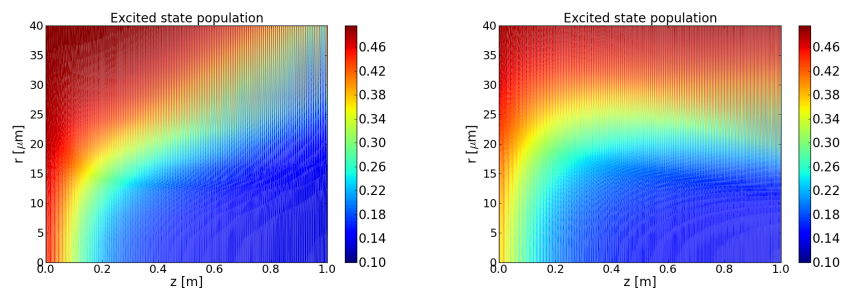

(a) Forward pumping (b) Backward pumping

Figure 3.10: Excited state population as a function of z and r for (a) forward pumping and (b) backward pumping of Fiber C at 5 kW pump power and 50 W input signal power.

The radial profiles of the local modes at a given distance along Fiber C are calculated numerically from Eq. (3.24) using the thermally perturbed refractive index profiles, examples of which are shown in Fig. 3.11. The initial ($z = 0$ m) mode profiles, plotted in Fig. 3.12, clearly show that several guided modes are present at the signal input. The launched signal can thus excite these local HOMs and the fiber is effectively multimode. The number of guided local modes may of course vary along the z axis as the temperature profile, and thus the refractive index perturbation, changes. Since our model is limited to

cylindrically symmetric fields, we do not consider non-symmetric local modes, although such modes would certainly be expected to become guided under the present conditions. For comparison, we also plot the local mode profiles at the output end ($z = 1$ m) of the fiber in Fig. 3.13. In the backward pumped case, the modes are more strongly confined due to the strong thermal lensing effect compared to the forward pumped case.

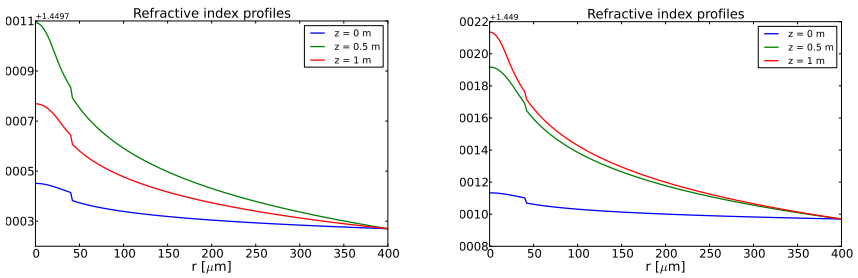

(a) Forward pumping (b) Backward pumping

Figure 3.11: Thermally perturbed refractive index profiles at various z for (a) forward pumping and (b) backward pumping of Fiber C at 5 kW pump power and 50 W input signal power.

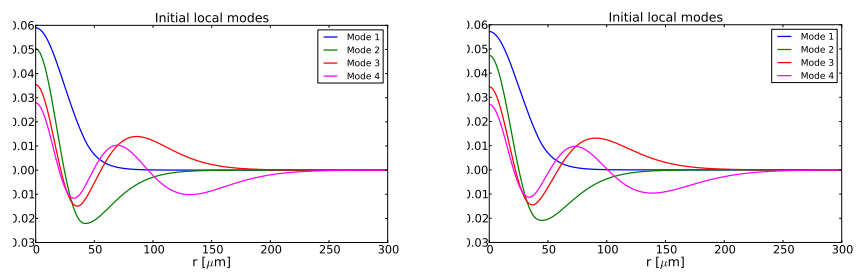

(a) Forward pumping (b) Backward pumping

Figure 3.12: Initial ($z = 0$) local modes for (a) forward pumping and (b) backward pumping of Fiber C at 5 kW pump power and 50 W input signal power.

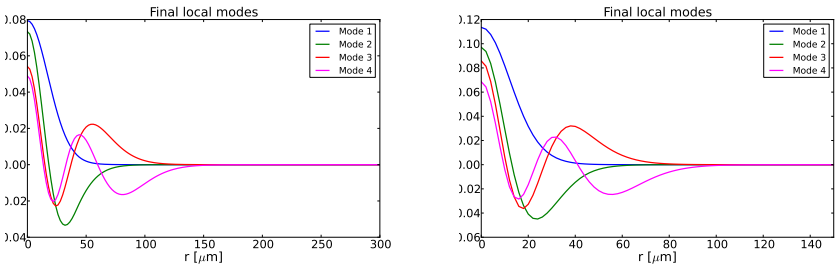

(a) Forward pumping (b) Backward pumping

Figure 3.13: Final ($z = 1$ m) local modes for (a) forward pumping and (b) backward pumping of Fiber C at 5 kW pump power and 50 W input signal power.

The local mode content $A_i(z)$ of the signal field is then defined to be

$$A_i(z) = \frac{|a_i(z)|^2}{\langle E_s|E_s\rangle} \tag{3.27}$$

and is plotted in Fig. 3.14. It is clear that in both the forward and backward pumped configurations, the input signal excites a small amount of the first local HOM. The beating of these two modes creates the oscillations seen in the beam effective area shown in Fig. 3.8, and the associated intensity variation leads to the periodic variation of the population inversion seen in Fig. 3.10. Since the thermal load, given by Eq. (3.19), also depends on the signal intensity and population inversion, the temperature also exhibits a periodic variation as seen in Fig. 3.9. This temperature variation results in an index grating with a local period that matches the local beat length of the two local modes, and therefore provides coupling between the local modes. As is evident from Fig. 3.14, this leads to transfer of power from the local FM to the HOM. It is possible that this effective multimode behavior of the fiber amplifier under high-power operation can cause significant degradation of the output beam quality, since uncontrollable external perturbations such as temperature fluctuations and mechanical vibrations could conceivably change the relative phase of the local modes leading to significant changes in the output beam, as discussed in [44]. However, the HOM content at the output is still modest, and the effect occurs only at very high power, whereas the TMI threshold powers reported in [16] are considerable lower.

It is argued in [38] that the thermally induced refractive index grating, caused by mode beating in a multimode fiber, cannot lead to coherent power

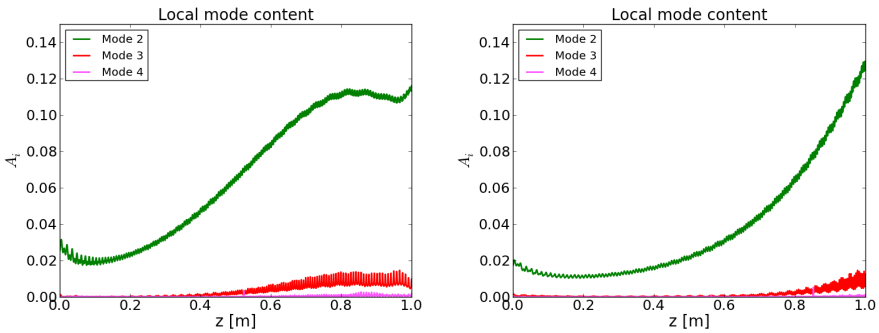

(a) Forward pumping (b) Backward pumping

Figure 3.14: Local mode content as a function of z for (a) forward pumping and (b) backward pumping of Fiber C at 5 kW pump power and 50 W input signal power.

transfer between two modes in a steady-state model of the thermal effect. The argument hinges on the left/right mirror symmetry of the mode interference pattern and the induced refractive index grating, and claims that a phase lag, which can be caused by the non-zero thermal diffusion time, is required to allow power transfer between the modes. Considering this argument, it is surprising that power transfer between the local modes in our model is observed, since our model is a steady-state model. While the argument presented in [38] is correct, we note that it does not strictly apply to the situation we are considering here. This is because the temperature changes significantly over a short distance, as is evident from Fig. 3.9, and hence the local modes and their associated propagation constants change significantly over a short distance, as can be seen by comparing Fig. 3.12 and Fig. 3.13. This causes the periodicity of the induced refractive index grating to vary with z, and therefore breaks the left/right mirror symmetry which is the core of the argument in [38]. Power transfer between the local modes of the fiber thus cannot be ruled out at high operating power, even with a steady-state model, and indeed the results presented in Fig. 3.14 clearly show power transfer from the local FM to the first local HOM.

To investigate the impact of gain saturation and pump depletion on the effective multimode behavior, we have simulated a fiber amplifier (Fiber D) with the same design as Fiber C, except that the Yb density is increased to 10^8 μm^{-3} and the length of the fiber is increased to 1.5 m. The input pump and signal power is 2000 W and 50 W, respectively. As can be seen from the plots of the

signal and pump power, shown in Fig. 3.15, the pump is completely depleted in both the forward and backward pumped cases. An interesting observation is

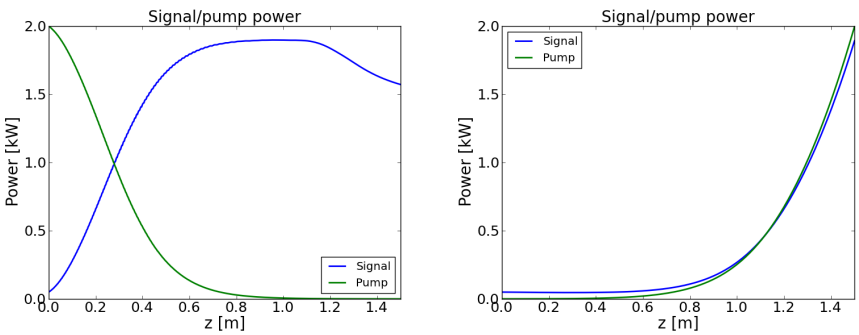

(a) Forward pumping (b) Backward pumping

Figure 3.15: Signal and pump power as a function of z for (a) forward pumping and (b) backward pumping of Fiber D.

that the signal power decreases significantly beyond 1 m in the forward pumped case. To understand the mechanism responsible for this decrease, we again consider the decomposition of the signal field into local modes, shown in Fig. 3.16, and the temperature distribution of the fiber, shown in Fig. 3.17. It is clear

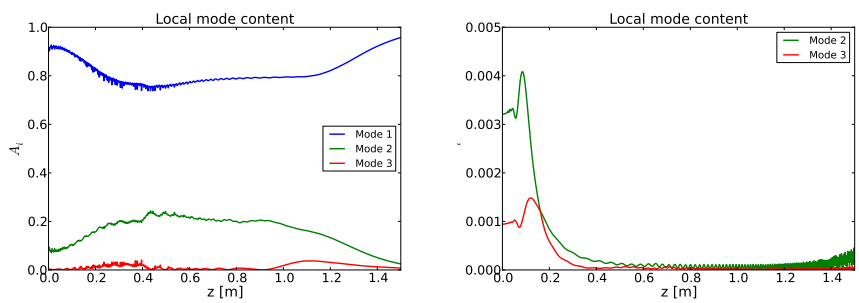

(a) Forward pumping (b) Backward pumping

Figure 3.16: Local mode content as a function of z for (a) forward pumping and (b) backward pumping of Fiber D at 2 kW pump power and 50 W input signal power.

that the first local HOM is strongly excited in the forward pumped case, but

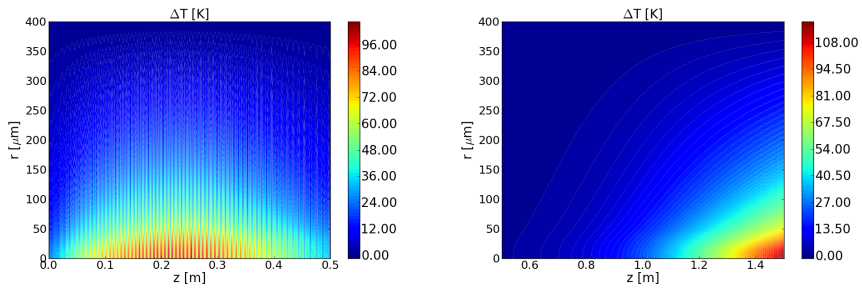

(a) Forward pumping (b) Backward pumping

Figure 3.17: Temperature increment as a function of z and r for (a) forward pumping and (b) backward pumping of Fiber D at 2 kW pump power and 50 W input signal power.

also that the signal gradually returns to the FM beyond 1 m, which coincides with the decrease in signal power and temperature. Recalling that we have employed a transparent boundary condition in our algorithm and considering the definition of the local mode content given in Eq. (3.27), it is clear that the reason for the loss of signal power is due to the fact that the local HOM evolves from a guided mode into a radiation mode as the radial temperature gradient decreases. The local HOM content of the signal is thus lost beyond 1 m. Another source of the loss of signal power beyond 1 m is of course spontaneous emission from the excited state of the Yb^{3+} ions. However, this loss is quite small due to the relatively long lifetime of the excited state. It has been verified that the signal power loss is dominated by the evolution of the local HOM from guided to non-guided by simulating Fiber D without the thermal effect, which shows negligible signal power loss.

In the backward pumped configuration, there is practically no thermal gradient at the signal input, since the pump is depleted, and hence there is only one guided local mode, with HOMs being non-guided. The signal is thus coupled into this single guided mode, and consequently no beating pattern is created. As the temperature gradient increases along with the signal power, multiple guided local modes appear, but the signal is seen to adiabatically follow the local FM, with only negligible excitation of HOMs. Ideally, the output beam quality should thus be comparable to a true single-mode fiber in this case.

Finally, we have investigated the power dependence of the effective multimode behavior by calculating the local mode content at the output of Fiber C for varying input pump and signal power in a forward pumped configuration.

The pump power is varied from 100 W to 5 kW, with an input signal power of 1% of the pump power. The results are shown in Fig. 3.18 which shows the local HOM content at the output as a function of pump power. We find that the first

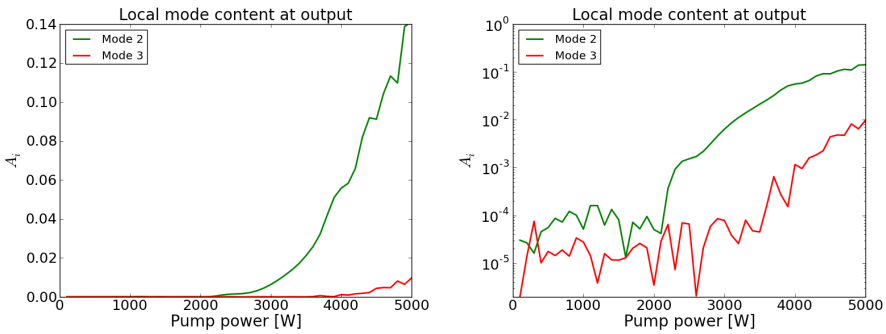

(a) Linear scale (b) Log scale

Figure 3.18: Local mode content at the output as a function of pump power for Fiber C on (a) linear scale and (b) log scale.

local HOM content increases at pump powers greater than 2 kW, with a corresponding input signal power of 20 W. Beam instability issues in large core fiber amplifiers have been reported to occur at power levels from a few hundred W to around 1 kW average power [14, 16]. These fibers are, however, not strictly single-mode, which can lead to thermally induced coupling between the FM and HOMs, as discussed in [37, 38], without the need for a sufficiently strong thermal effect to create effective multimode behavior. Furthermore, our model can only describe symmetric local modes, and we expect that non-symmetric local modes become guided at much lower power. Our results thus show that even under the idealized conditions of true single-mode fiber design and a perfectly symmetric input signal beam profile, which prevents excitation of any asymmetric higher-order local modes, the output signal can be contaminated by HOMs at sufficiently high operating power.

3.3 Conclusion

We have developed a BPM model of high-power Yb-doped fiber amplifiers. The heating of the fiber due to the quantum defect associated with the gain medium, as well as THB, is taken fully into account. The model is limited to circularly symmetric signal fields, leading to a very fast implementation that

permits efficient simulation of backward pumped amplifiers, but at the cost of generality of the model. The model was used to study the thermo-optical effects in LMA single-mode amplifiers, and it was found that the large radial temperature gradient results in a thermal lensing effect, which significantly decreases the effective area of the beam, leading to higher peak intensity and thereby increased nonlinear effects. Furthermore, it was found that the thermal effect can become large enough to induce an effective multimode behavior in nominally single-mode fibers, which was quantified by decomposing the signal beam profile into local modes. If a local HOM is excited at the signal input, the mode beating between the local FM and HOM can set up a periodic longitudinal temperature variation, leading to a refractive index grating which can transfer power from the FM to the HOM. As discussed in [44], the excitation of HOMs may be detrimental to the output beam quality, and fiber amplifier designs should seek to avoid such behavior. Our results show that it is possible to reduce the thermally induced local HOM content in nominally single-mode fibers if the thermal load is weak enough at the signal input. This may be possible to achieve in backward pumped fiber amplifiers with sufficient length and Yb doping to effectively absorb the pump. Our results also indicate that as the thermal effect diminishes due to gain saturation in a forward pumped amplifier, any signal power contained in a local HOM will remain in that mode as it turns into a non-guided mode. Finally, we investigated the power dependence of the thermally-induced multimode behavior and found that the local HOM content increases with operating power beyond a certain threshold power. This threshold power is, however, significantly above what is found experimentally. Since our model is limited to circularly symmetric fields, we cannot investigate a situation in which the input beam profile is shifted or tilted relative to the symmetry axis of the fiber, which could lead to excitation of asymmetric local HOMs. We therefore expect the threshold power obtained by our model to be an upper threshold, applicable under idealized conditions in which no excitation of asymmetric local HOMs occurs. Furthermore, our model assumes a steady-state behavior of the thermal nonlinearity, which may not be appropriate.

Chapter 4

Fourier expansion beam propagation method

The BPM algorithm presented in chapter 3 is limited in its applicability due to the central assumption of a circularly symmetric electric field. This prevented the investigation of the interaction between the FM and any non-symmetric HOMs. Since multimode fibers can guide non-symmetric modes, an adequate description of field propagation in such fibers requires an algorithm which does not impose circular symmetry on the electric field. Furthermore, it was shown that the thermo-optic effect can be strong enough to render nominally single-mode fibers effectively multimode, which will introduce non-symmetric guided local modes, and the circularly symmetric BPM algorithm is not sufficient to fully describe even single-mode fibers at high gain.

A simple way to remove the limitation of circular symmetry is to formulate the BPM algorithm in full 3D by discretizing the transverse profile of the relevant quantities on a 2D grid. Such codes are, however, numerically quite intensive [37], and it is therefore highly desirable to seek a more efficient formulation of the problem.

In this chapter, we shall formulate a BPM algorithm which takes the azimuthal dependence of the field into account in an efficient way by a Fourier expansion. This leads to an algorithm that is 3D, yet still numerically efficient. This code has been used to consider propagation through a slightly multimode fiber with parameters comparable to realistic experimental conditions under which TMI has been observed.

4.1 Numerical method

4.1.1 Beam propagation equation

As in chapter 3, we write the electric field of the signal in terms of a slowly varying field E

$$\mathbf{E}(\mathbf{r},t) = \mathbf{u}_s E(\mathbf{r}) e^{i(\beta z - \omega_s t)} + \text{c.c.}, \tag{4.1}$$

where, as in chapter 3, $\mathbf{u}_s$ is the polarization unit vector, ω_s is the carrier angular frequency of the field and β is an estimate of the propagation constant of the FM. We impose no restrictions on the spatial dependence of E, but do restrict ourselves to considering circularly symmetric fibers, such that the relative permittivity depends only on the radial coordinate r. In the scalar approximation, the slowly varying electric field E obeys the beam propagation equation

$$\frac{\partial E}{\partial z} = \frac{i}{2\beta}\left[\nabla_\perp^2 E(\mathbf{r}) + \left(k_0^2\left[\varepsilon(r) + \Delta\varepsilon(\mathbf{r})\right] - \beta^2\right) E(\mathbf{r}) + \mu_0 \omega_s^2 p(\mathbf{r})\right], \tag{4.2}$$

where $k_0 = \omega_s/c$, $\Delta\varepsilon$ is the perturbation of the relative permittivity due to changes in temperature and p is the slowly varying polarization due to the Yb dopants.

We now take advantage of the fact that we are considering circularly symmetric fibers by expressing the azimuthal dependence of the slowly varying electric field and polarization in a truncated Fourier series

$$E(\mathbf{r}) = \sum_{m=-M}^{M} E_m(r,z) e^{im\phi}, \quad p(\mathbf{r}) = \sum_{m=-M}^{M} p_m(r,z) e^{im\phi}. \tag{4.3}$$

The perturbation $\Delta\varepsilon$ is expanded in a similar fashion

$$\Delta\varepsilon(\mathbf{r}) = \sum_{m=-2M}^{2M} \Delta\varepsilon_m(r,z) e^{im\phi}, \tag{4.4}$$

where the Fourier series is truncated at $|m| = 2M$ to be consistent with the truncation of the Fourier series for the electric field. Inserting Eqs. (4.3) and (4.4) into Eq. (4.2) yields a set of $2M+1$ differential equations for each Fourier component $E_n(r,z)$

$$\begin{aligned}\frac{\partial E_n}{\partial z} = \frac{i}{2\beta}\Bigg[&\frac{\partial^2 E_n}{\partial r^2} + \frac{1}{r}\frac{\partial E_n}{\partial r} + \left(k_0^2\varepsilon(r) - \beta^2 - \frac{n^2}{r^2}\right) E_n(r,z) \\ &+ k_0^2 \sum_{m=-M}^{M} \Delta\varepsilon_{n-m}(r,z) E_m(r,z) + \mu_0\omega_s^2 p_n(r,z)\Bigg].\end{aligned} \tag{4.5}$$

The polarization $p(\mathbf{r})$ induced by the interaction between the Yb ions and the signal and pump light is determined by the steady-state solution to the density matrix equations given by Eq. (3.4). The excited state population $\rho_2(\mathbf{r})$ is expanded in the Fourier series

$$\rho_2(\mathbf{r}) = \sum_{m=-2M}^{2M} \rho_{2,m}(r,z)e^{im\phi}, \tag{4.6}$$

which leads to a set of $4M+1$ linear equations for the $4M+1$ Fourier components

$$\left(\Phi_p\left(\sigma_{ap}+\sigma_{ep}\right)+\gamma\right)\rho_{2,n} + \frac{2\varepsilon_0 c n_c}{\hbar\omega_s}\left(\sigma_{as}+\sigma_{es}\right)\sum_{m=-2M}^{2M}\rho_{2,m}\times \sum_{l=-M}^{M} E_l^* E_{l+n-m} = \frac{2\varepsilon_0 c n_c}{\hbar\omega_s}\sigma_{as}\sum_{m=-M}^{M} E_m^* E_{m+n} + \Phi_p\sigma_{ap}\delta_{n,0}. \tag{4.7}$$

The Fourier components of the induced polarization due to the Yb ions are then given by

$$p_n = \frac{\varepsilon_0 n_c \rho_{Yb}}{k_0}\left(i+\frac{\Delta_s}{\tilde{\gamma}_{23}}\right)\left(\sigma_{as}E_n - \left(\sigma_{es}+\sigma_{as}\right)\sum_{m=-M}^{M} E_m\rho_{2,n-m}\right), \tag{4.8}$$

which is inserted into Eq. (4.5). As in chapter 3, the signal field is propagated forward in z using the split-operator approach

$$E_n(z+\Delta z, r) \approx \exp\left(\frac{\Delta z}{2}\hat{R}\right)\exp\left(\Delta z\hat{N}\right)\exp\left(\frac{\Delta z}{2}\hat{R}\right)E_n(z,r), \tag{4.9}$$

where the operators $\hat{R}$ and $\hat{N}$ are given by

$$\hat{R}E_n = \frac{i}{2\beta}\left(\frac{\partial^2 E_n}{\partial r^2} + \frac{1}{r}\frac{\partial E_n}{\partial r} - \frac{n^2}{r^2}E_n\right), \tag{4.10a}$$

$$\hat{N}E_n = -\frac{\rho_{Yb}n_c k_0}{2\beta}\left(1-i\frac{\Delta_s}{\tilde{\gamma}_{23}}\right)\left(\sigma_{as}E_n - \left(\sigma_{es}+\sigma_{as}\right)\sum_{m=-M}^{M}E_m\rho_{2,n-m}\right) + \frac{i}{2\beta}\left[\left(\varepsilon k_0^2-\beta^2\right)E_n + k_0^2\sum_{m=-M}^{M}\Delta\varepsilon_{n-m}E_m\right] \tag{4.10b}$$

The exponential of the $\hat{R}$ operator is approximated by the Padé approximant

$$\exp\left(\frac{\Delta z}{2}\hat{R}\right) \approx \frac{1+\frac{\Delta z}{4}\hat{R}}{1-\frac{\Delta z}{4}\hat{R}}. \tag{4.11}$$

The $\hat{N}$ operator is split into a "diagonal" part $\hat{D}$ and a "coupling" part $\hat{C}$ such that $\hat{N} = \hat{D} + \hat{C}$, where the diagonal operator is given by

$$\hat{D}E_n = -\frac{\rho_{Yb} n_c k_0}{2\beta}\left(1 - i\frac{\Delta_s}{\tilde{\gamma}_{23}}\right)\sigma_{as}E_n + \frac{i}{2\beta}\left(\varepsilon k_0^2 - \beta^2\right)E_n, \tag{4.12}$$

and the coupling operator is given by

$$\begin{aligned}\hat{C}E_n = {} & \frac{\rho_{Yb} n_c k_0}{2\beta}\left(1 - i\frac{\Delta_s}{\tilde{\gamma}_{23}}\right)(\sigma_{es} + \sigma_{as})\sum_{m=-M}^{M} E_m \rho_{2,n-m} \\ & + \frac{ik_0^2}{2\beta}\sum_{m=-M}^{M}\Delta\varepsilon_{n-m}E_m.\end{aligned} \tag{4.13}$$

We then approximate the exponential of the $\hat{N}$ operator by

$$\exp\left(\Delta z\hat{N}\right) \approx \exp\left(\Delta z\hat{D}\right)\left(1 + \Delta z\hat{C}\right). \tag{4.14}$$

4.1.2 Input signal field

We assume that the input signal field at $z = 0$ has a Gaussian profile which is shifted along the x axis relative to the center of the fiber, and with a propagation direction which is tilted around the y axis relative to the z axis of the fiber. The input signal field profile is then given by

$$E(x,y) = E_0 \exp\left(-\frac{(x-x_0)^2\cos^2\theta + y^2}{w^2}\right)\exp\left(ik_0\left(x - x_0\right)\sin\theta\right) \tag{4.15}$$

where x_0 is the x coordinate of the center of the beam profile and θ is the tilt angle of the propagation direction relative to the z axis. To first order in θ we have

$$E \approx \exp\left(-\frac{r^2 + x_0^2}{w^2} - ik_0 x_0 \sin\theta\right)\exp\left[\left(\frac{2x_0 r}{w^2} + ik_0 r\sin\theta\right)\cos\phi\right], \tag{4.16}$$

and using the identity

$$e^{u\cos\phi} = \sum_{m=-\infty}^{\infty} I_m(u)e^{im\phi}, \tag{4.17}$$

where I_n is the modified Bessel function of the first kind, we obtain the Fourier expansion for the input signal field

$$E_n(r,0) \approx E_0 \exp\left(-\frac{r^2+x_0^2}{w^2} - ik_0 x_0 \sin\theta\right) I_n\left[\left(\frac{2x_0}{w^2} + ik_0 \sin\theta\right) r\right]. \quad (4.18)$$

4.1.3 Thermal nonlinearity

To calculate the thermal profile at a given z, we solve the steady-state heat equation

$$\nabla_\perp^2 \Delta T(\mathbf{r}) = -\frac{Q}{\kappa} \quad (4.19)$$

subject to the Dirichlet boundary condition $\Delta T(R) = 0$. Expanding the temperature increment $\Delta T(\mathbf{r})$ and the thermal load $Q(\mathbf{r})$ in a Fourier series

$$\Delta T(\mathbf{r}) = \sum_{m=-2M}^{2M} \Delta T_m(r,z) e^{im\phi}, \quad Q(\mathbf{r}) = \sum_{m=-2M}^{2M} Q_m(r,z) e^{im\phi} \quad (4.20)$$

yields the set of $4M+1$ differential equations for the Fourier components ΔT_n

$$\frac{\partial^2 \Delta T_n}{\partial r^2} + \frac{1}{r}\frac{\partial \Delta T_n}{\partial r} - \frac{n^2}{r^2}\Delta T_n(r,z) = -\frac{Q_n(r,z)}{\kappa}. \quad (4.21)$$

The thermal load Q is given by Eq. (3.19), which can be rewritten using the steady-state equation for the excited state population ρ_2 into

$$Q(\mathbf{r}) = \rho_{Yb}\hbar\left(\omega_p - \omega_s\right)\left(\Phi_p\left(\sigma_{ap} - \left(\sigma_{ep} + \sigma_{ap}\right)\rho_2\right) - \gamma_{21}\rho_2\right). \quad (4.22)$$

Inserting Fourier expansions for the relevant quantities yields the Fourier components of the thermal load

$$Q_n(r,z) = \rho_{Yb}\hbar\left(\omega_p - \omega_s\right)\left(\Phi_p\left(\sigma_{ap}\delta_{n,0} - \left(\sigma_{ep} + \sigma_{ap}\right)\rho_{2,n}\right) - \gamma_{21}\rho_{2,n}\right). \quad (4.23)$$

The set of equations given by Eq. (4.21) are solved by a standard finite-difference discretization of the differential operators, and the refractive index perturbation is found from the relation $\Delta\varepsilon = \eta\Delta T$.

4.1.4 Pump propagation equation

As in chapter 3, we assume that the pump intensity is uniform over the core and model the propagation of the pump by the simple ordinary differential equation

$$\frac{\mathrm{d}P_p}{\mathrm{d}z} = \pm\frac{1}{A_{cl}} P_p(z) \int_0^{2\pi}\int_0^{R_c} \rho_{Yb}(r)\left(\sigma_{ep}\rho_2(\mathbf{r}) - \sigma_{ap}\rho_1(\mathbf{r})\right) r\mathrm{d}r\mathrm{d}\phi. \quad (4.24)$$

Inserting the Fourier expansion for ρ_2 and using $\rho_1 + \rho_2 = 1$ yields

$$\frac{\mathrm{d}P_p}{\mathrm{d}z} = \pm\frac{2\pi}{A_{cl}} P_p(z) \int_0^{R_c} \rho_{Yb}(r) \left[\left(\sigma_{ap} + \sigma_{ep} \right) \rho_{2,0}(r,z) - \sigma_{ap} \right] r \mathrm{d}r, \qquad (4.25)$$

which is easily propagated in the z direction from the initial value $P_p(0)$.

The entire BPM algorithm proceeds exactly as described in chapter 3. Since we are interested in simulating only slightly multimode fibers, we need only include the first few terms in the Fourier expansions, because a fiber with a low V parameter does not guide modes with high values of m. This is the great advantage of the Fourier expansion formulation of the BPM algorithm over the simpler cartesian grid formulation used in e.g. [37].

4.2 Numerical results

The numerical model described in section 4.1 has been used to study the interaction between the FM and HOMs in a slightly multimode LMA fiber. While it is in principle possible to manufacture single-mode PCFs with very large cores, the extremely low NA of such fibers renders them impractical due to their extreme sensitivity to bending loss and longitudinal inhomogeneities [45]. A very low NA also makes coupling light into the core very difficult. For these reasons, LMA fibers are often designed with a slightly higher NA, but as a consequence the fibers are then no longer strictly single-mode.

The simulated fiber, in the following referred to as Fiber E, is a double-clad SIF with a core diameter of 80 μm, an inner cladding diameter of 270 μm and an outer diameter of 800 μm. The core index $n_c = 1.45$ and the cladding index $n_{cl} = 1.4499$, which gives $V \approx 4.16$ at the signal wavelength $\lambda_s = 1030$ nm. The Yb density in the core is $\rho_{Yb} = 3 \times 10^7$ $\mu\mathrm{m}^{-3}$ and the fiber is pumped at 975 nm with a pump power of 1 kW. Both forward and backward pumping has been simulated. The simulated fiber is comparable to typical rod-type fibers, which are known to be susceptible to TMI at operating powers much lower than what is simulated here [46].

10 W of signal power is launched into the fiber with the Gaussian profile given by Eq. (4.15). The spot radius $w = 40$ μm, the beam displacement $x_0 = 0$ and the beam tilt $\theta = 0.1°$. This small beam tilt results in a small excitation of the cosine LP_{11} mode, and we can thus study the interaction between the FM and this HOM.

As in chapter 3, we decompose the signal field in a set of local modes for each z position. Since we no longer consider circularly symmetric fields, we encounter the added complication that the thermal permittivity perturbation $\Delta\varepsilon$ is no longer circularly symmetric. Strictly speaking, the local modes of the

fiber, as defined by the eigenvalue equation

$$\nabla_\perp^2 \Psi + k_0^2 \left[\varepsilon(r) + \Delta\varepsilon(\mathbf{r}_\perp, z)\right] \Psi(\mathbf{r}_\perp, z) = \beta(z)^2 \Psi(\mathbf{r}_\perp, z), \tag{4.26}$$

can no longer be written as a product of a function of the radial coordinate r and a function of the azimuthal angle ϕ. To overcome this difficulty, we calculate the local modes using a ϕ averaged value of $\Delta\varepsilon$. Using the Fourier expansion of $\Delta\varepsilon$, the approximate local modes are then calculated by solving the eigenvalue equation

$$\nabla_\perp^2 \Psi + k_0^2 \left[\varepsilon(r) + \Delta\varepsilon_0(r, z)\right] \Psi(\mathbf{r}_\perp, z) = \beta(z)^2 \Psi(\mathbf{r}_\perp, z), \tag{4.27}$$

which results in local modes that can be written as

$$\Psi_m(r, \phi, z) = R_m(r, z) \cos(m\phi). \tag{4.28}$$

Here, R_m is the radial function of the local mode Ψ_m, and only the cosine modes are included due to the symmetry of the input signal field.

4.2.1 Forward pumping

We consider first forward pumping of Fiber E. The signal and pump power as a function of z and the local mode content A_i of the signal as a function of z is plotted in Fig. 4.1.

From the plot of the signal and pump power in Fig. 4.1a we see that the pump is not completely absorbed at the signal output, which reduces the efficiency of the amplifier. A longer piece of fiber is required to fully absorb the pump, but rod-type fibers such as the one simulated here are usually not much longer than about 1 m due to their sensitivity to bending loss.

The plot of the local mode content, shown in Fig. 4.1b, shows that the small tilt of the input signal beam leads to about 4% excitation of the local LP_{11} mode. In addition, 2% of the signal power is coupled into the local LP_{02} mode. The rest of the input power is found in the local FM, with only negligible contributions from other modes. As the signal power grows, the HOM content is seen to oscillate with z, especially for the LP_{11} local mode. This is most likely due to the fact that the mode decomposition is done with respect to the approximate local modes discussed above, rather than the true local modes. From the plot we also see that the z averaged HOM content decreases with increasing signal power. This is due to preferential gain of the FM. We thus see no sign of TMI, even at the very high operating power simulated here.

A plot of the amplitude of the signal electric field, normalized to the peak value of the input signal field, in the xz and yz planes is shown in Fig. 4.2. As discussed above, the input signal beam propagation axis is tilted about the y

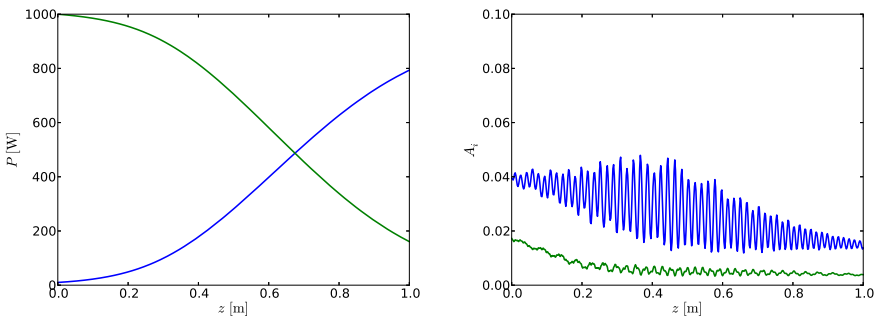

(a) Signal and pump power

(b) Local mode content

Figure 4.1: (a) Signal (blue curve) and pump (green curve) power for forward pumping of Fiber E as a function of z, and (b) local mode content of the first $m = 1$ local mode (blue curve) and the second $m = 0$ local mode (green curve) as a function of z.

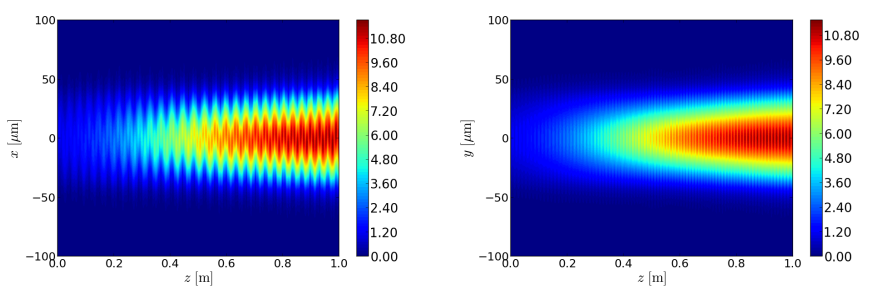

(a) xz plane

(b) yz plane

Figure 4.2: Normalized amplitude of the signal field in the (a) xz plane and the (b) yz plane for forward pumping of Fiber E.

axis, and therefore only the cosine LP_{11} local mode is excited. Consequently, the beating between the FM and LP_{11} cannot be seen in the plot of the yz plane, since the cosine LP_{11} mode has a node in this plane. On the other hand, the signal field in the xz plane, shown in Fig. 4.2a, clearly shows the effect of the beating between the LP_{01} and LP_{11} modes, which results in the zigzag motion of the field amplitude. Even with the preferential gain of the FM, which reduces the LP_{11} mode content to less than 2% at the output, the

mode beating is still visible. Close inspection of the signal field amplitude in the yz plane, shown in Fig. 4.2b, reveals the effect of mode beating between the local LP_{01} and LP_{02} modes. The beat length is shorter compared to the beat length of the LP_{01}-LP_{11} beating, which is due to the larger difference in mode effective index. The LP_{01}-LP_{02} beating is also visible upon close inspection in the xz plane, superimposed on the stronger LP_{01}-LP_{11} beat pattern.

As in the circularly symmetric cases considered in chapter 3, the beat pattern of the signal field leads to a corresponding pattern in the temperature of the fiber. This is shown in Fig. 4.3 for the xz and yz planes. As expected,

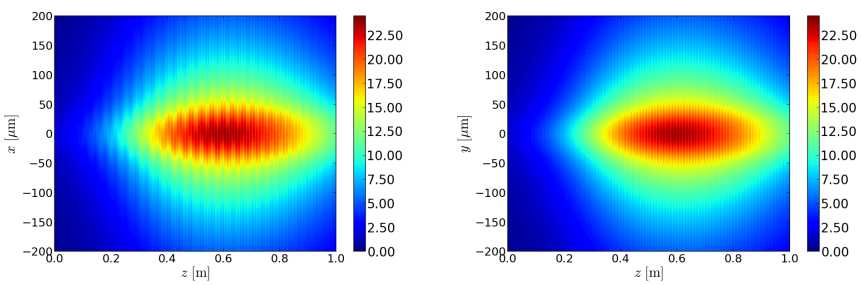

(a) xz plane (b) yz plane

Figure 4.3: Temperature variation ΔT in the (a) xz plane and the (b) yz plane for forward pumping of Fiber E.

the temperature pattern mirrors the mode beating pattern of the signal field. Since we are considering a steady-state situation with a monochromatic field, the temperature pattern, and hence the refractive index perturbation, is in phase with the signal beat pattern. The long beat length of the signal also justifies the approximation of neglecting the longitudinal heat flow when calculating the temperature variation.

The mode beating also leads to a spatially varying excited state population, which is shown in Fig. 4.4. By comparison with Fig. 4.2, we see that where the signal amplitude is large, the excited state population is reduced, which creates a THB pattern that mirrors the signal amplitude, in addition to the overall THB of the population inversion. By considering the expression for the heat load Q given in Eq. (3.19), we see that this THB pattern counteracts the mode beating pattern of the signal, which results in a weaker temperature pattern than if the population inversion was fixed. However, as is clearly evident from Fig. 4.3, this effect is not strong enough to remove the temperature pattern.

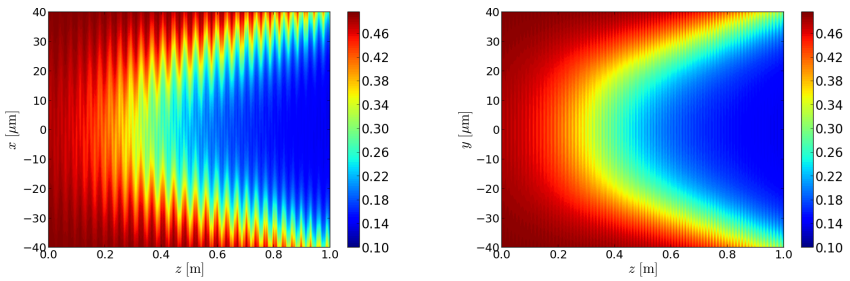

(a) xz plane (b) yz plane

Figure 4.4: Excited state population ρ_2 in the (a) xz plane and the (b) yz plane for forward pumping of Fiber E.

4.2.2 Backward pumping

In chapter 3 we discussed how a strong longitudinal temperature gradient may lead to a transfer of power between the local FM and HOM. This longitudinal temperature gradient is typically larger in backward pumped amplifiers, which is also the preferred pumping scheme. For this reason, we simulate backward pumping of Fiber E to see if this pumping configuration results in a transfer of power to a HOM.

The pump and signal power as well as the local mode content of the signal as a function of z is plotted in Fig. 4.5. The plot of the signal and pump power in Fig. 4.5a shows a more rapid increase of signal power with z compared to the forward pumped case. This should result in a greater longitudinal temperature gradient compared to the forward pumped case. From the plot of the local HOM content we see that 4% of the signal power is coupled into the local LP_{11} mode and slightly less than 2% is coupled into the local LP_{02} mode at the signal input, which is the same as in the forward pumped case. The preferential gain of the FM again leads to a decreasing local HOM content with z, and we see no sign of any nonlinear power transfer between the FM and the HOMs.

The normalized signal amplitude in both the xz and yz planes is plotted in Fig. 4.6. As in the forward pumped case, we see the beat pattern from the LP_{01}-LP_{11} mode beating clearly in the xz plane with the weaker LP_{01}-LP_{02} beating superimposed. As mentioned above, the signal intensity increases rapidly over a shorter distance compared to the forward pumped case, which tends to break the periodicity of the mode beating pattern.

The resulting temperature variation in the xz and yz planes of the fiber is shown in Fig. 4.7. Compared to the forward pumped case, the peak tem-

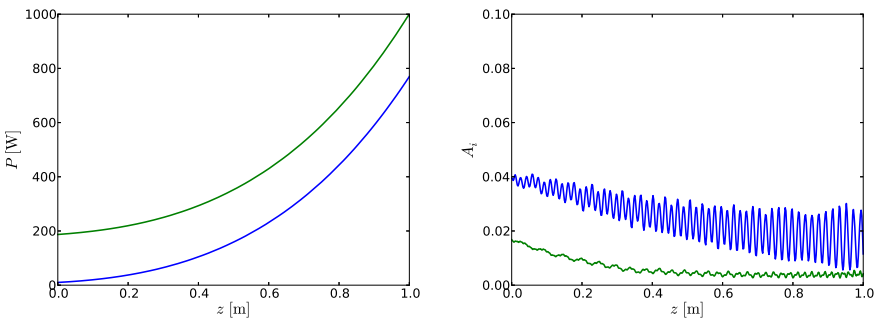

(a) Signal and pump power (b) Local mode content

Figure 4.5: (a) Signal (blue curve) and pump (green curve) power for backward pumping of Fiber E as a function of z, and (b) local mode content of the first $m = 1$ local mode (blue curve) and the second $m = 0$ local mode (green curve) as a function of z.

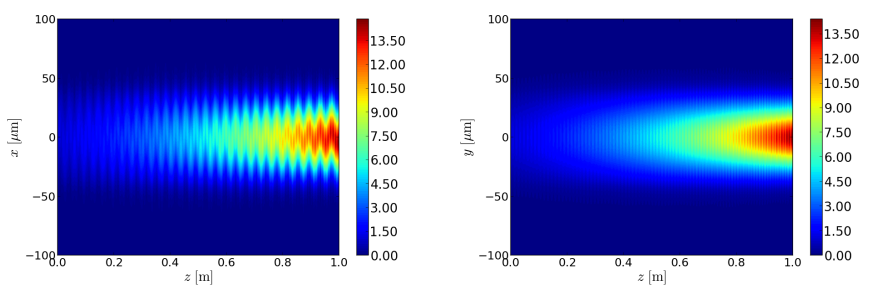

(a) xz plane (b) yz plane

Figure 4.6: Normalized amplitude of the signal field in the (a) xz plane and the (b) yz plane for backward pumping of Fiber E.

perature increment is almost twice as large for the backward pumped case. The larger depth of the resulting refractive index perturbation is apparently insufficient to cause a transfer of power from the FM to the HOMs.

Finally, we compare the spatial variation of the excited state population to the forward pumped case. It is plotted in both the xz and yz planes in Fig. 4.8. Compared to the forward pumped case, we note that the gain saturation is more evenly distributed along the length of the fiber, but otherwise displays similar

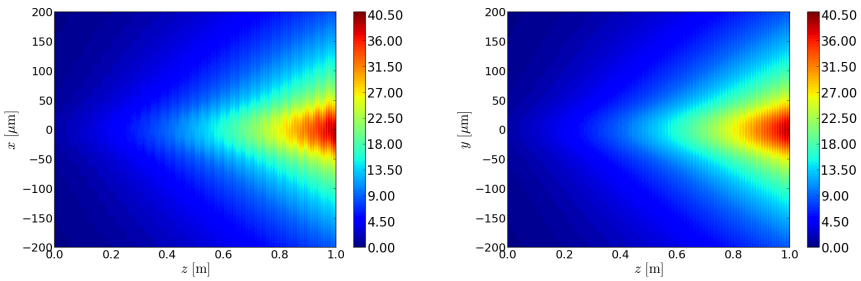

(a) xz plane (b) yz plane

Figure 4.7: Temperature variation ΔT in the (a) xz plane and the (b) yz plane for backward pumping of Fiber E.

features.

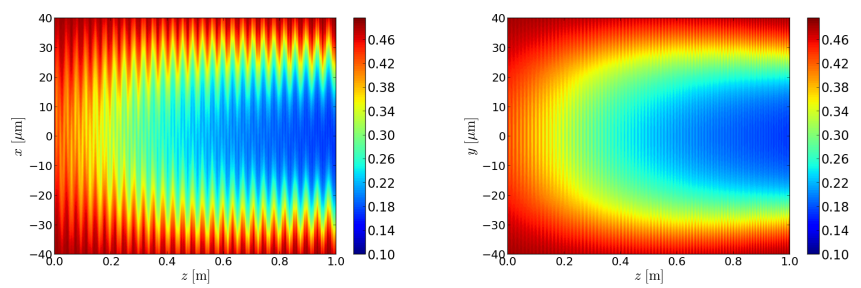

(a) xz plane (b) yz plane

Figure 4.8: Excited state population ρ_2 in the (a) xz plane and the (b) yz plane for backward pumping of Fiber E.

4.3 Conclusion

The 2D BPM algorithm developed in chapter 3 has been extended to a 3D model by expanding the azimuthal dependence of the dynamical variables in a Fourier series. For slightly multimode fibers, only the first few terms in the series are required for an accurate representation, since the fiber does not guide modes with a high value of m. This fact makes the Fourier expansion BPM

algorithm numerically very efficient.

The analysis of the signal field by a decomposition into local modes was facilitated by calculating approximate local modes, based on a ϕ averaged value of the relative permittivity perturbation. This allowed the approximate local modes to be separable into a radial and an azimuthal part, which made the comparison with modes of a SIF easy.

Applying the method to a slightly multimode LMA rod-type fiber operating at very high average power, we found no sign of TMI in either forward or backward pumped operation. The fiber parameters were chosen to be representative of typical LMA fiber amplifiers for which TMI has been observed experimentally at much lower average operating power than was simulated. The numerical results by Jauregui *et al.* [37] showed an efficient transfer of power from the FM to the HOM at much lower operating power than was simulated here, using a very similar 3D BPM approach, but these results were later retracted as a result of a too coarse longitudinal discretization [47]. Our results thus indicate that a steady-state model of the thermal nonlinearity cannot adequately explain the phenomenon of TMI, and that a dynamical model, which takes the finite response time of the thermal nonlinearity into account, is required, as suggested by Smith and Smith [38].

Chapter 5

Semi-analytic model of transverse mode instability

In the previous two chapters, the results of a BPM model of the thermal nonlinear effects in LMA fiber amplifiers were discussed. However, this model failed to provide an adequate description of the recently observed phenomenon of TMI, as the simulated operating power under which any significant transfer of power between modes occurred, was much higher than what has been observed experimentally [16]. As pointed out in [38], the reason for the inefficiency of the mode coupling in the model is most likely due to the assumption of steady-state behavior of the thermal nonlinearity. Using a BPM model which included the temporal dynamics of the thermal nonlinearity, the authors were able to show an efficient thermally induced transfer of power from the FM to a HOM of the simulated fiber, provided that the HOM was seeded with a small amount of light which was redshifted a few kHz relative to the light in the FM. This redshift causes the mode beating pattern to move along the fiber. The thermally induced index grating also moves along the fiber, but since the thermal response time is finite, the index grating lags behind the mode beating pattern, which permits efficient coupling between the two modes.

While the presence of a slightly redshifted frequency component in a HOM was thus shown in [38] to lead to TMI, no definite conclusion was drawn as to the origin of this seeding. The unintentional coupling of a small fraction of the signal into a HOM at the input of a multimode fiber amplifier is unavoidable in practice, but it was not clear in [38] what the cause of the small redshift could be in reality. This redshift is essential, since without it the mode beating pattern would be stationary, and no phase-lag would exist between it and the thermally induced index grating. Furthermore, a BPM model which includes

the temporal dynamics of the problem is numerically very demanding, and it is therefore of considerable interest to seek a simplified model of the problem, which nonetheless captures the essential physics of TMI.

In this chapter, we shall consider a semi-analytic coupled-mode model of TMI and show how the seeding required to initiate the instability may arise from quantum noise. By applying the mode to various SIF designs, we shall study how the TMI threshold power depends on various fiber design parameters. We shall also discuss how the model can be applied to PCF designs.

5.1 Coupled-mode equations

We assume that the electric field in the scalar approximation can be written as a superposition of two normalized modes $\psi_1(x,y)$ and $\psi_2(x,y)$ with propagation constants β_1, β_2 and angular frequencies ω_1, ω_2

$$E = a_1(z)\psi_1 e^{i(\beta_1 z-\omega_1 t)} + a_2(z)\psi_2 e^{i(\beta_2 z-\omega_2 t)} + c.c., \tag{5.1}$$

where ψ_1 is the FM, ψ_2 is the HOM and a_i are the slowly varying complex mode amplitudes. This field expansion is inserted into the scalar wave equation

$$\frac{\partial^2 E}{\partial z^2} + \nabla_\perp^2 E(\mathbf{r},t) - \frac{\varepsilon(\mathbf{r},t)}{c^2}\frac{\partial^2 E}{\partial t^2} = 0, \tag{5.2}$$

where the relative permittivity is given by

$$\varepsilon(\mathbf{r},t) = \varepsilon_f(\mathbf{r}_\perp) - i\frac{g(\mathbf{r})\sqrt{\varepsilon_f}}{k} + \Delta\varepsilon(\mathbf{r},t). \tag{5.3}$$

Here ε_f is the real relative permittivity of the fiber, g is the bulk gain coefficient due to the rare-earth doping, k is the vacuum wavenumber, taken to be the same for both field components, and the subscript $\perp$ denotes the transverse coordinates x, y. $\Delta\varepsilon = \eta\Delta T$ is the thermally induced perturbation, where ΔT is the increase in temperature relative to a given reference temperature, which is typically the temperature of the cooling fluid, and η is the thermo-optic coefficient of the fiber material.

Our goal is to obtain coupled-mode equations for the mode amplitudes $a_i(z)$. To obtain the coupling coefficients, we need to calculate the perturbation $\Delta\varepsilon$ and therefore consider the heat equation under the assumption of a slow longitudinal variation of the temperature

$$\rho C\frac{\partial \Delta T}{\partial t} - \kappa\nabla_\perp^2 \Delta T(\mathbf{r},t) = Q(\mathbf{r},t), \tag{5.4}$$

where ρ is the density, C is the specific heat capacity and κ is the thermal conductivity of the fiber material. The heat load Q is related to the intensity I by

$$Q(\mathbf{r},t) = \left(\frac{\lambda_s}{\lambda_p} - 1\right) g(\mathbf{r}) I(\mathbf{r},t), \tag{5.5}$$

where λ_s and λ_p are the signal and pump wavelengths, respectively. Inserting the field expansion given by Eq. (5.1), the intensity reads

$$\begin{aligned} I(\mathbf{r},t) = 2\sqrt{\varepsilon_f}\varepsilon_0 c \Big(& |a_1|^2 \psi_1^2 + |a_2|^2 \psi_2^2 \\ & + a_1 a_2^* \psi_1 \psi_2 e^{i(\Delta\beta z - \Delta\omega t)} + a_1^* a_2 \psi_1 \psi_2 e^{-i(\Delta\beta z - \Delta\omega t)} \Big), \end{aligned} \tag{5.6}$$

where $\Delta\beta = \beta_1 - \beta_2$ is the difference in the propagation constants and $\Delta\omega = \omega_1 - \omega_2$ is the difference in angular frequency.

Fourier transforming Eq. (5.4) with respect to time yields

$$\nabla_\perp^2 \Delta\tilde{T}(\mathbf{r},\omega) - q(\omega)\Delta\tilde{T}(\mathbf{r},\omega) = -\frac{\tilde{Q}(\mathbf{r},\omega)}{\kappa}, \tag{5.7}$$

where $q = i\rho C\omega/\kappa$. This equation can be solved by the appropriate Green's function [48]:

$$\Delta\tilde{T}(\mathbf{r},\omega) = \frac{1}{\kappa} \iint G[\mathbf{r}_\perp, \mathbf{r}'_\perp, q(\omega)] \tilde{Q}(\mathbf{r}',\omega) \mathrm{d}^2\mathbf{r}'_\perp. \tag{5.8}$$

The Green's function $G(\mathbf{r}_\perp, \mathbf{r}'_\perp, \omega)$ satisfies the differential equation

$$\nabla_\perp^2 G(\mathbf{r}_\perp, \mathbf{r}'_\perp, \omega) - q(\omega) G(\mathbf{r}_\perp, \mathbf{r}'_\perp, \omega) = -\delta(\mathbf{r}_\perp - \mathbf{r}'_\perp), \tag{5.9}$$

where the transverse Laplacian is taken with respect to the unprimed coordinates. As boundary condition for ΔT, we assume the simple Dirichlet boundary condition $\Delta T = 0$ at the fiber surface, which should be a reasonable boundary condition for the case of efficiently water-cooled amplifiers.

Fourier transforming Eq. (5.5) with respect to time, we can obtain $\Delta\tilde{T}$ from Eq. (5.8). Inverting the Fourier transform then yields $\Delta T(\mathbf{r},t)$, which gives the permittivity perturbation

$$\Delta\varepsilon(\mathbf{r},t) = \Delta\varepsilon_0(\mathbf{r}) + \Delta\varepsilon_+(\mathbf{r}) e^{i(\Delta\beta z - \Delta\omega t)} + \Delta\varepsilon_-(\mathbf{r}) e^{-i(\Delta\beta z - \Delta\omega t)}, \tag{5.10}$$

where the static part of the perturbation is given by

$$\begin{aligned} \Delta\varepsilon_0 = \frac{2 n_c \varepsilon_0 c \eta g}{\kappa} \left(\frac{\lambda_s}{\lambda_p} - 1\right) \Bigg(& |a_1|^2 \iint_{\Omega_d} G(\mathbf{r}_\perp, \mathbf{r}'_\perp, 0) \psi_1(\mathbf{r}')^2 \mathrm{d}^2\mathbf{r}'_\perp \\ & + |a_2|^2 \iint_{\Omega_d} G(\mathbf{r}_\perp, \mathbf{r}'_\perp, 0) \psi_2(\mathbf{r}')^2 \mathrm{d}^2\mathbf{r}'_\perp \Bigg) \end{aligned} \tag{5.11}$$

and the dynamic part is given by

$$\Delta\varepsilon_+ = \frac{2n_c\varepsilon_0 c\eta g}{\kappa}\left(\frac{\lambda_s}{\lambda_p}-1\right)a_1 a_2^* \iint_{\Omega_d} G(\mathbf{r}_\perp,\mathbf{r}'_\perp,-\Delta\omega)\psi_1(\mathbf{r}'_\perp)\psi_2(\mathbf{r}'_\perp)\mathrm{d}^2\mathbf{r}'_\perp \tag{5.12}$$

$$\Delta\varepsilon_- = \frac{2n_c\varepsilon_0 c\eta g}{\kappa}\left(\frac{\lambda_s}{\lambda_p}-1\right)a_1^* a_2 \iint_{\Omega_d} G(\mathbf{r}_\perp,\mathbf{r}'_\perp,\Delta\omega)\psi_1(\mathbf{r}'_\perp)\psi_2(\mathbf{r}'_\perp)\mathrm{d}^2\mathbf{r}'_\perp \tag{5.13}$$

In the calculation of $\Delta\varepsilon$ we have assumed that the transverse profile of the gain coefficient g is uniform on the domain Ω_d, and zero outside. We are thus ignoring any effects of THB here. As we saw in chapter 3 and 4, THB can be quite severe in fiber amplifiers, so ignoring it's effect can be a rather crude approximation. On the other hand, THB is not believed to be the cause of TMI, and since our purpose is to formulate a simplified description of this effect, we shall ignore any effects that are not crucial to understanding the fundamental dynamics of TMI. Note, however, that we allow g to have a slow z dependence, which may be inherent to the fiber or due to saturation of the gain. We have also assumed that the refractive index of the fiber has the constant value n_c on Ω_d, which is the case for SIFs and most PCFs.

Inserting Eq. (5.10) into the wave equation, we can derive a set of coupled-mode equations for the mode amplitudes

$$\frac{\mathrm{d}a_1}{\mathrm{d}z} = iC_1\left(A_{11}\left|a_1\right|^2 + A_{12}\left|a_2\right|^2 + B_{12}\left|a_2\right|^2\right)a_1 + \frac{\Gamma_1}{2}ga_1, \tag{5.14a}$$

$$\frac{\mathrm{d}a_2}{\mathrm{d}z} = iC_2\left(A_{22}\left|a_2\right|^2 + A_{21}\left|a_1\right|^2 + B_{21}\left|a_1\right|^2\right)a_2 + \frac{\Gamma_2}{2}ga_2, \tag{5.14b}$$

where

$$C_i = \frac{n_c\varepsilon_0 ck^2\eta g}{\beta_i\kappa}\left(\frac{\lambda_s}{\lambda_p}-1\right), \tag{5.15}$$

and the coupling coefficients are given by

$$A_{ij} = \iint \psi_i(\mathbf{r}_\perp)^2 \iint_{\Omega_d} G(\mathbf{r}_\perp,\mathbf{r}'_\perp,0)\psi_j(\mathbf{r}'_\perp)\mathrm{d}^2\mathbf{r}'_\perp\mathrm{d}^2\mathbf{r}_\perp \tag{5.16}$$

$$B_{21} = \iint \psi_2(\mathbf{r}_\perp)\psi_1(\mathbf{r}_\perp) \iint_{\Omega_d} G(\mathbf{r}_\perp,\mathbf{r}'_\perp,\Delta\omega)\psi_1(\mathbf{r}'_\perp)\psi_2(\mathbf{r}'_\perp)\mathrm{d}\mathbf{r}'_\perp\mathbf{r}_\perp \tag{5.17}$$

$$B_{12} = \iint \psi_2(\mathbf{r}_\perp)\psi_1(\mathbf{r}_\perp) \iint_{\Omega_d} G(\mathbf{r}_\perp,\mathbf{r}'_\perp,-\Delta\omega)\psi_1(\mathbf{r}'_\perp)\psi_2(\mathbf{r}'_\perp)\mathrm{d}\mathbf{r}'_\perp\mathbf{r}_\perp \tag{5.18}$$

From the definition of the Green's function given in Eq. (5.9) we see that it obeys the relation $G(\mathbf{r}_\perp,\mathbf{r}'_\perp,-\omega) = G(\mathbf{r}_\perp,\mathbf{r}'_\perp,\omega)^*$, by which it follows that

$B_{12} = B_{21}^*$ since the mode functions are assumed real. Finally, the overlap of a mode with the doped region is quantified by the overlap integral

$$\Gamma_i = \frac{k}{\beta_i} \iint_{\Omega_d} \sqrt{\varepsilon_f(\mathbf{r}_\perp)} \psi_i(\mathbf{r}_\perp)^2 \mathrm{d}^2\mathbf{r}_\perp, \tag{5.19}$$

In the derivation of the coupled-mode equations, we have neglected any spatio-temporal oscillations of the gain coefficient g, which occur if the signal intensity becomes comparable to the saturation intensity of the gain medium. As we discussed in chapter 4 such oscillations will tend to reduce the oscillations in the heat load and hence the thermally induced refractive index grating, leading to a weaker coupling between the modes. By neglecting this effect, our model will thus overestimate the mode coupling.

The power in each mode is given by $P_i = 2n_c\varepsilon_0 c\,|a_i|^2$ and obey the coupled-mode equations

$$\frac{\mathrm{d}P_1}{\mathrm{d}z} = -\chi_1(\Delta\omega) g(z) P_2 P_1 + \Gamma_1 g(z) P_1, \tag{5.20a}$$

$$\frac{\mathrm{d}P_2}{\mathrm{d}z} = \chi_2(\Delta\omega) g(z) P_2 P_1 + \Gamma_2 g(z) P_2, \tag{5.20b}$$

where the coupling constants χ_i are given by

$$\chi_{1,2}(\Delta\omega) = \frac{\eta k^2}{\kappa\beta_{1,2}} \mathrm{Im}\left[B_{21}(\Delta\omega)\right] \left(1 - \frac{\lambda_s}{\lambda_p}\right). \tag{5.21}$$

This quantity can be calculated numerically for any given fiber design for which the Green's function and mode functions can be determined. From the property of the Green's function $G(\mathbf{r}_\perp, \mathbf{r}'_\perp, -\omega) = G(\mathbf{r}_\perp, \mathbf{r}'_\perp, \omega)^*$, we find the important property of the coupling constant

$$\chi_i(-\Delta\omega) = -\chi_i(\Delta\omega). \tag{5.22}$$

It is evident from Eqs. (5.20) that a positive coupling constant χ_2 will lead to a nonlinear gain of the light in the HOM. However, for $\Delta\omega = 0$, we see from Eq. (5.22) that $\chi_i(0) = 0$ so that no transfer of power between the modes occurs in this case. This is what we expect, since in this case the mode beating pattern is stationary and hence no phase-lag exists between it and the thermally induced refractive index grating.

5.2 TMI threshold of a SIF amplifier

In this section we consider a simple water-cooled SIF amplifier for which analytical expressions for the Green's function and the fiber modes are known.

The modes of a SIF were discussed in chapter 2, and the Green's function for this problem is given by the expansion

$$G(\mathbf{r}_\perp, \mathbf{r}'_\perp, \omega) = \frac{1}{2\pi} \sum_{m=-\infty}^{\infty} g_m(r, r', \omega) e^{im(\phi-\phi')}. \tag{5.23}$$

The radial Green's functions can be found by standard methods [49] to be

$$g_n(r, r', \omega) = \begin{cases} I_n(\sqrt{q}r)[K_n(\sqrt{q}r') - D_n I_n(\sqrt{q}r')] & \text{for } 0 \leq r < r' \\ I_n(\sqrt{q}r')[K_n(\sqrt{q}r) - D_n I_n(\sqrt{q}r)] & \text{for } r' < r \leq R \end{cases} \tag{5.24}$$

where I_n and K_n are the modified Bessel functions of the first and second kind, respectively, and

$$D_n = \frac{K_n(\sqrt{q}R)}{I_n(\sqrt{q}R)}, \tag{5.25}$$

where R is the outer radius of the fiber. Using the analytical expressions for the modes of a SIF and the Green's function, the 2D integrals in Eq. (5.17) can be reduced to 1D integrals and evaluated by standard numerical methods.

5.2.1 Calculation of the coupling constant

We consider first a fiber with a V parameter of 3 and calculate the coupling constant between the LP_{01} and LP_{11} modes for varying core sizes R_c and a fixed outer radius R of 500 μm. The core refractive index is taken to be 1.45 and the signal and pump wavelengths are assumed to be 1030 nm and 975 nm, respectively. Fig. 5.1 shows the coupling constant χ_1, which is indistinguishable from χ_2, as a function of $\Delta f = \Delta\omega/2\pi$ for core radii of 10 μm, 20 μm and 40 μm.

As expected, the coupling constant vanishes for $\Delta f = 0$. However, for a small frequency difference on the order of a kHz, depending on core size, the coupling constant is positive and a transfer of power from LP_{01} to LP_{11} can occur. Interestingly, the maximum value of the coupling constant is largely insensitive to the core size, and only the position and width of the peak varies significantly.

We now investigate the dependence of the coupling constant on the V parameter of the fiber by calculating χ for a fixed $R_c = 20$ μm and varying V with all other parameters the same as before. The results are shown in Fig. 5.2. Here we see a significant increase in χ as V increases. This can be understood by considering Eq. (5.17) from which it is clear that the coupling constant depends on the overlap of the two modes. For $V = 2.5$, which is just above cut-off

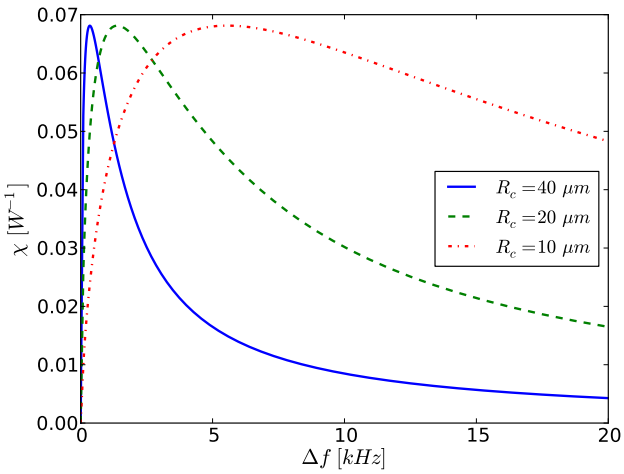

Figure 5.1: Coupling constant χ for LP_{01}-LP_{11} coupling as a function of Δf for varying R_c and $V = 3$.

for LP_{11}, the overlap between the two modes is small, and as V increases, the overlap, and hence the coupling constant, increases as well.

Finally, we investigate the dependence of the coupling constant on the size of the rare-earth doped region. We do this by considering a fiber with fixed $V = 3$ and $R_c = 20$ μm but varying radius of the doped region of the core R_{Yb}. The results are shown in Fig. 5.3. It is seen that reducing the size of the doped region causes a significant reduction in the coupling constant, which again is expected from Eq. (5.17), since the inner integral is taken over the decreasing doped region while the mode functions remain unchanged.

5.2.2 Solution of the coupled-mode equations

To study the onset of TMI in the fiber amplifiers, we solve Eqs. (5.20) under the assumption $P_2 \ll P_1$. We thus obtain

$$\frac{P_2(L)}{P(L)} \approx \frac{P_2(0)}{P_1(0)} \exp\left(\frac{\chi(\Delta\omega)}{\Gamma_1}\Delta P - \Delta\Gamma g_{av} L\right), \tag{5.26}$$

where $P_i(L)$ is the output power in mode i, $P_i(0)$ is the input power in mode i, $P = P_1 + P_2$ is the total power, $\Delta P = P(L) - P(0)$, $\Delta\Gamma = \Gamma_1 - \Gamma_2$ and g_{av}

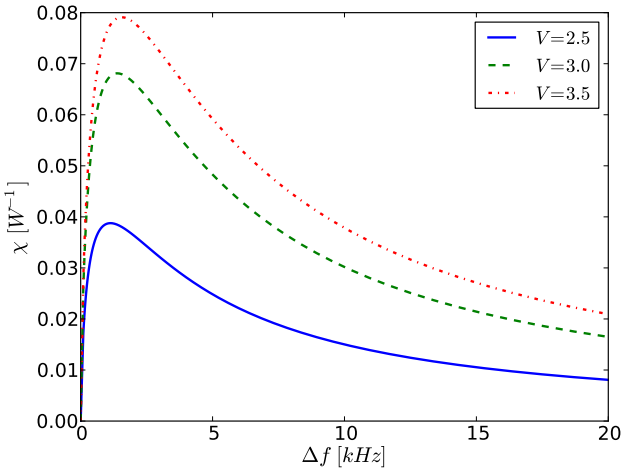

Figure 5.2: Coupling constant χ for LP_{01}-LP_{11} coupling as a function of Δf for varying V and $R_c = 20$ μm.

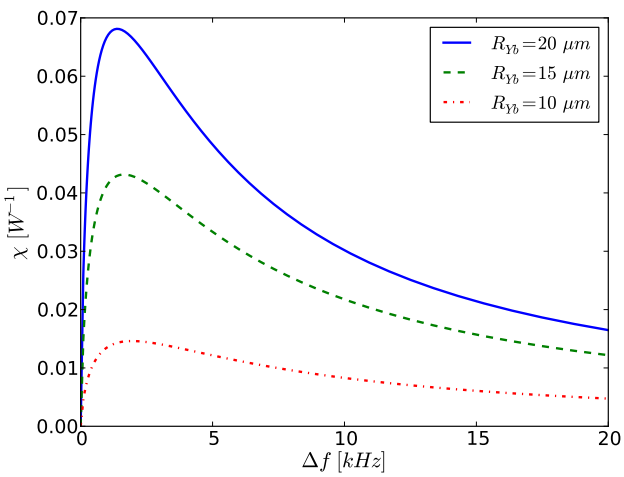

Figure 5.3: Coupling constant χ for LP_{01}-LP_{11} coupling as a function of Δf for varying R_{Yb} and $R_c = 20$ μm, $V = 3$.

is the gain averaged over the length of the fiber L

$$g_{av} = \frac{1}{L}\int_0^L g(z)\mathrm{d}z. \tag{5.27}$$

Note that the solution depends only on the total gain $g_{av}L$ and not on the precise z dependence of g, which is influenced by gain saturation and thus not known a priori. As discussed above, the coupling constant χ vanishes for $\Delta\omega = 0$. We therefore assume that the seed responsible for the mode instability is quantum noise. To obtain the power in the HOM, we assume that the equivalent input power spectral density (PSD) of the quantum noise is $\hbar\omega$ [30, 50] and integrate Eq. (5.26) over all frequencies to obtain the HOM content at the output $x_o = P_2(L)/P(L)$:

$$x_o \approx \frac{e^{-\Delta\Gamma g_{av}L}}{P_1(0)}\int_{-\infty}^{\infty}\hbar\omega\exp\left(\frac{\Delta P}{\Gamma_1}\chi(\omega_1-\omega)\right)\mathrm{d}\omega. \tag{5.28}$$

The integral in Eq. (5.28) can be approximated by Laplace's method, which yields the following approximate expression for the HOM content

$$x_o \approx \hbar\omega_1\sqrt{\frac{2\pi\Gamma_1}{|\chi''(\omega_0)|}}\frac{P(L)^{\left(\frac{\Gamma_2}{\Gamma_1}-\frac{3}{2}\right)}}{P_1(0)^{\frac{\Gamma_2}{\Gamma_1}}}\exp\left(\frac{\chi_0}{\Gamma_1}P(L)\right) \tag{5.29}$$

where χ_0 and ω_0 are the maximum value of χ and the corresponding frequency, χ'' is the second derivative of χ and we have assumed $\Delta P \approx P$. Given a threshold value x_{th} of the HOM content, Eq. (5.29) can be solved numerically for the corresponding threshold power P_{th}.

We have calculated the threshold power for a threshold HOM content $x_{th} = 0.05$ for the various values of the design parameters of the SIF models considered in this section. The input power $P_1(0)$ was taken to be 1 W in all cases. The results are summarized in Table 5.1 and show a significant variation of the threshold power with fiber design. Lowering the V parameter to reduce the overlap between LP_{01} and LP_{11} is clearly effective in increasing the power threshold. Similarly, reducing the area of the doped region is effective in reducing the mode instability. The variation of the threshold power with core size is quite small. This is at odds with recent experiments with LMA fibers, which show a decreasing TMI threshold with increasing core size [46]. It is important to note, however, that our model does not take the thermally induced change of the mode functions ψ into account. This effect can be significant for very-large-mode fibers with very small index contrasts, and will lead to stronger confinement and overlap of the mode functions [1], thus increasing the nonlinear coupling constant and decreasing the power threshold.

Table 5.1: Power thresholds of various SIFs.

R_c [μm]	R_{Yb} [μm]	V	P_{th} [W]
10	10	3	440
20	20	3	458
40	40	3	479
20	20	3.5	401
20	20	2.5	813
20	15	3	586
20	10	3	1035

5.3 TMI threshold of a PCF amplifier

The method presented in section 5.1 can be applied to any fiber design for which the mode functions and thermal Green's function can be determined, either analytically or numerically. Jørgensen *et al.* have applied the method to several PCF amplifier designs [6, 7], and we shall review two examples in this section: a commercially available LMA PCF amplifier, and a so-called large pitch fiber (LPF) design [15].

We assumed in [6, 7] that the thermal Green's function for the PCF fiber structure could be well approximated by an infinite boundary Green's function. This assumption was checked by varying the outer radius R in the SIF model considered in section 5.2. It was found that the precise value of the outer radius made no noticeable difference in the results, provided that the outer radius was not unrealistically close to the core. In the infinite boundary case, the Green's function can be written

$$G(\mathbf{r}_\perp, \mathbf{r}'_\perp, \omega) = G(\mathbf{r}_\perp - \mathbf{r}'_\perp, \omega), \tag{5.30}$$

and is thus a function of the difference between the primed and unprimed coordinates only. This allows us to write the expression for B_{21} given in Eq. (5.17) as

$$B_{21} = \iint \psi_2(\mathbf{r}_\perp)\psi_1(\mathbf{r}_\perp) \iint G(\mathbf{r}_\perp - \mathbf{r}'_\perp, \Delta\omega)\psi_1(\mathbf{r}'_\perp)\psi_2(\mathbf{r}'_\perp)f(\mathbf{r}'_\perp)\mathrm{d}\mathbf{r}'_\perp \mathbf{r}_\perp, \tag{5.31}$$

where $f(\mathbf{r}_\perp) = 1$ if $\mathbf{r} \in \Omega_d$ and zero otherwise. The inner integral is seen to be a convolution, which can be efficiently evaluated numerically using a fast Fourier transform (FFT). The outer integral can then be easily evaluated numerically using standard numerical quadrature methods. The infinite boundary Green's

function is given by [49]

$$G(\mathbf{r}_\perp - \mathbf{r}'_\perp, \Delta\omega) = \frac{1}{2\pi} K_0 \left(\sqrt{q(\Delta\omega)}\, |\mathbf{r}_\perp - \mathbf{r}'_\perp| \right), \tag{5.32}$$

where K_0 is the zeroth-order modified Bessel function of the second kind.

The first fiber considered is the Yb-doped double-clad active fiber DC-200/40-PZ-Yb from NKT Photonics A/S. The inner cladding consists of a triangular array of airholes as well as two stress-applying parts (SAPs) which introduce birefringence in the fiber. This is done to make the fiber polarization-maintaining (PM). The pitch of the triangular array is $\Lambda = 10.3$ μm and the hole-diameter-to-pitch ratio $d/\Lambda = 0.21$ for the simulated fiber. The Yb-doped core of the fiber consists of a 7-cell defect, which gives a core diameter of approximately 40 μm. The outer cladding consists of a ring of large airholes with a diameter of 200 μm. The fiber design is illustrated in Fig. 5.4. The

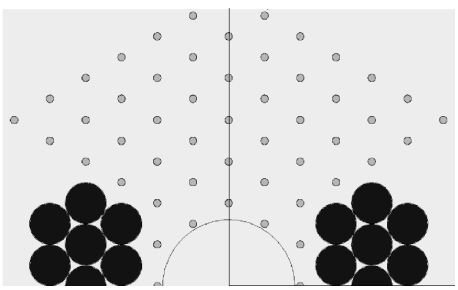

Figure 5.4: Fiber design of the DC-200/40 fiber. The large black elements on both sides of the core are SAPs. The image is adopted from [51].

guided modes for this fiber were calculated by the FEM using the software package COMSOL. The normalized scalar mode functions for the FM and the first HOM are shown in Fig. 5.5. These mode functions are qualitatively vary similar to the LP_{01} and LP_{11} modes of the SIF. Unlike the SIF, however, the LP_{11}-like modes are not degenerate, and the coupling between the FM and each LP_{11}-like mode will thus be slightly different. Here we consider the HOM which gives the lowest value of the TMI threshold.

The second fiber we consider is also an Yb-doped double-clad LPF called LPF30 [46]. The inner cladding is a triangular array of airholes, but without any SAPs. The pitch of the cladding structure is $\Lambda = 30$ μm, and is thus considerably larger compared to the DC-200/40 fiber. The hole-diameter-to-pitch ratio is $d/\Lambda = 0.22$, which is very close to the DC-200/40 fiber. The Yb-doped core of the LPF consists of a single-cell defect, giving a core diameter of approximately 53 μm. As for the DC-200/40 fiber, the outer cladding consists

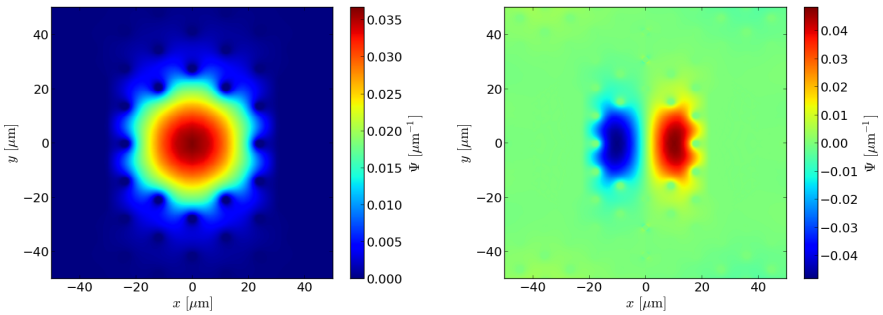

(a) FM (b) HOM

Figure 5.5: Calculated normalized scalar mode functions for the (a) FM and (b) HOM of the DC-200/40 fiber.

of a ring of large airholes which has a diameter of 170 μm. The fiber design is illustrated in Fig. 5.6

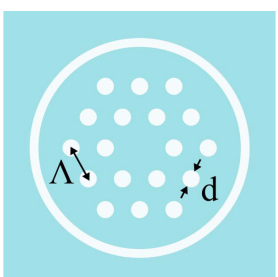

Figure 5.6: Fiber design of the LPF30 fiber. The image is adopted from [15].

The normalized scalar mode functions for the LPF30 fiber that give rise to the lowest TMI threshold are shown in Fig. 5.7. Visually comparing the mode profiles of the two fiber designs, we see that the HOM of the LPF30 fiber appears to be significantly more delocalized compared to the HOM of the DC-200/40 fiber. From the analysis of the SIF, which showed that an increasing overlap between the modes and the doped region of the core led to a lower TMI threshold, we expect the LPF30 to have the higher TMI threshold. Calculating the mode coupling constant χ for both fibers, shown in Fig. 5.8, we do indeed see that the LPF30 fiber has a lower maximum value of the coupling constant. Considering an input signal power $P_1(0) = 1$ W and a

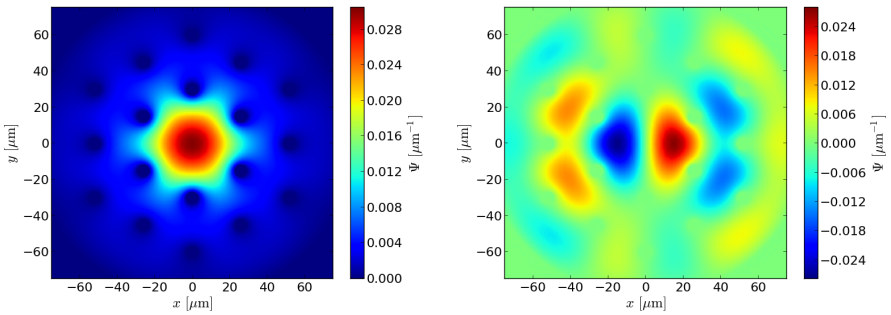

(a) FM (b) HOM

Figure 5.7: Calculated normalized scalar mode functions for the (a) FM and (b) HOM of the LPF30 fiber.

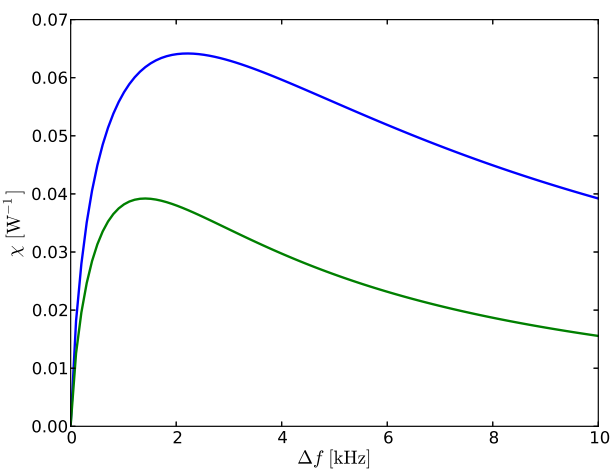

Figure 5.8: Coupling constant χ as a function of Δf for DC-200/40 (blue curve) and LPF30 (green curve). The LPF30 fiber has a weaker coupling between the FM and the HOM compared to the DC-200/40 fiber due to its more delocalized HOM.

threshold HOM content $x_{th} = 0.05$, we found a TMI threshold power of 438 W for the DC-200/40 fiber and 610 W for the LPF30 fiber. We note, however,

that the DC-200/40 fiber is actually intended to be coiled, which is not taken into account in the calculation of the modes. Bending the fiber is likely to have a significant impact on the HOM profile, which could impact the result of the threshold calculation. Also, at the threshold powers predicted here, the mode profiles can be perturbed by the strong radial thermal gradients, as we discussed in chapter 3, and this thermal perturbation of the mode profiles is likely to be more severe with increasing core size due to the weak guiding in such fibers.

5.4 Conclusion

In summary, we have formulated a simple semi-analytical model of thermally induced mode coupling in multimode rare-earth doped fiber amplifiers. The model clearly shows that the thermal nonlinearity of a fiber amplifier may lead to TMI seeded by quantum noise. It also predicts that the TMI threshold is strongly influenced by the combined overlap of the FM and HOM profiles and the doped region of the core. Fiber designs which reduce this overlap should thus be less susceptible to TMI. Due to the approximations made in the derivation of the model, in particular with regards to gain saturation and thermal perturbations of the mode profiles, the predicted threshold power should not be expected to be in perfect agreement with experiments, but the model could provide a good basis for comparing the performance of different fiber designs. The model presented in this chapter also does not allow us to study the temporal dynamics of TMI or its behaviour at signal powers above the threshold, nor have we considered other sources of instability seeding, such as e.g. noise in the input signal.

Chapter 6

Coupled-mode model of transverse mode instability

6.1 Introduction

The semi-analytical model presented in chapter 5 provides a plausible explanation of TMI as a thermally-induced mode coupling seeded by quantum noise. In this chapter, the basic ideas behind this model will be used to formulate a full coupled-mode model of thermally-induced TMI. This model will allow us to study the temporal dynamics of this phenomenon, as well as its behaviour as the signal power is increased above the TMI threshold. We shall also consider seeding of TMI by signal intensity noise, and the effect of amplitude modulation of the input signal.

A number of recent publications have presented detailed experimental studies of the properties and dynamics of TMI. We shall summarize these findings here so that we can compare them to the results of the coupled-mode model presented in this chapter.

- Eidam *et al.* [16] found that the output power did not decrease as the TMI threshold was reached, and that it could be increased beyond the threshold power.
- A study by Jansen *et al.* [46] comparing LPFs with different core diameters found that the TMI threshold power decreased with increasing core diameter.
- Stutzki *et al.* [52] presented a modal decomposition of the output signal during TMI in a LPF and showed that the mode amplitudes and phases

fluctuated in a chaotic fashion on a ms timescale.

- A comparison of TMI in LMA fibers with different core diameters by Otto *et al.* [53] showed that the timescale of TMI depends on the core diameter of the fiber.

- The same study by Otto *et al.* [53] found that only the first HOM was excited by TMI, except for fibers with vary large cores.

- It was found by Otto *et al.* [53] and Ward *et al.* [54] that the dynamics of TMI at output powers close to the threshold was harmonic, developing into chaotic behaviour at higher power. However, a very similar experiment by Karow *et al.* [55] found no such harmonic transition region.

- The signal launching condition was found by Ward *et al.* [54] and Karow *et al.* [55] to have only a small impact on the TMI threshold power.

- The experiments by Ward *et al.* [54] showed an increase in the TMI threshold power when the fiber was efficiently cooled, compared to passive cooling in air.

- Ward *et al.* [54] also found that the linewidth of the input signal had a negligible impact on the TMI threshold.

While the model presented in this chapter makes a number of simplifying assumptions, we shall see that it explains most of the important features of TMI mentioned above.

The chapter is organized as follows: In section 6.2 we derive the theoretical model and discuss the approximations made. In section 6.3 we consider operation at the threshold and derive an approximate analytic solution of the coupled mode equations, which is valid when the HOM is only weakly excited. Using this approximate solution, we consider seeding of TMI by quantum noise and signal intensity noise. Through a numerical solution, we investigate the temporal and spectral features of TMI near the threshold, as well as the dependence of the threshold power on the spectral width of the signal. In section 6.4 we consider operation beyond the stability threshold, and study the temporal and spectral dynamics in this case, as well as investigate how the average HOM content of the output signal varies as power is increased. Finally, in section 6.5, we consider an amplitude modulated input signal and show how the thermally induced nonlinear interaction between the modes leads to the generation of additional sidebands in the spectral characteristics of the TMI phenomenon.

6.2 Theory

6.2.1 Coupled mode equations

The quasi-monochromatic electric field of the signal propagating in the fiber is written in terms of a slowly-varying envelope

$$\mathbf{E}(\mathbf{r},t) = \frac{1}{2}\mathbf{u}\left(E(\mathbf{r},t)e^{i\omega_0 t} + c.c.\right), \tag{6.1}$$

where $\mathbf{u}$ is the polarization unit vector, E is the temporally slowly-varying field envelope and ω_0 is the carrier angular frequency of the signal. Using an analogous expression for the induced polarization, the frequency domain wave equation in the scalar approximation can be written as

$$\nabla^2 E(\mathbf{r},\omega-\omega_0) + \frac{\omega^2}{c^2}\varepsilon(\mathbf{r})E(\mathbf{r},\omega-\omega_0) = -\mu_0\omega^2 P_{NL}(\mathbf{r},\omega-\omega_0), \tag{6.2}$$

where $E(\mathbf{r},\omega)$ is the Fourier transform of $E(\mathbf{r},t)$, ε is the complex relative permittivity of the fiber and $P_{NL}(\mathbf{r},\omega)$ is the slowly-varying nonlinear induced polarization due to the heating of the fiber. The relative permittivity is written in terms of its real and imaginary parts as

$$\varepsilon(\mathbf{r}) = \varepsilon_f(\mathbf{r}_\perp) - i\frac{g(\mathbf{r})\sqrt{\varepsilon_f(\mathbf{r}_\perp)}}{k_0}, \tag{6.3}$$

where ε_f is the real relative permittivity of the fiber, g is the bulk gain coefficient due to the rare-earth doping of the fiber core, $k_0 = \omega_0/c$ is the vacuum wave number and the subscript $\perp$ denotes the transverse coordinates x, y. We have disregarded material dispersion of the fiber, since we shall restrict ourselves to considering signals with a linewidth of less than a few tens of kHz.

The nonlinear induced polarization is related to the change in temperature of the fiber ΔT and the electric field by

$$P_{NL}(\mathbf{r},t) = \varepsilon_0\eta\Delta T(\mathbf{r},t)E(\mathbf{r},t), \tag{6.4}$$

where η is a thermo-optic coefficient, which relates the change in relative permittivity of the fiber to the change in temperature through

$$\Delta\varepsilon(\mathbf{r},t) = \eta\Delta T(\mathbf{r},t). \tag{6.5}$$

Taking the Fourier transform of Eq. (6.4) and inserting the result into Eq. (6.2) yields

$$\nabla^2 E(\mathbf{r},\Omega) + k^2\varepsilon(\mathbf{r})E(\mathbf{r},\Omega) = -\frac{\eta k^2}{2\pi}\int_{-\infty}^{\infty}\Delta T(\mathbf{r},\Omega')E(\mathbf{r},\Omega-\Omega')\mathrm{d}\Omega', \tag{6.6}$$

where $\Omega = \omega - \omega_0$ and $k = \omega/c$. The change in temperature ΔT obeys the heat equation

$$\rho C \frac{\partial \Delta T}{\partial t} - \kappa \nabla_\perp^2 \Delta T(\mathbf{r}, t) = Q(\mathbf{r}, t), \tag{6.7}$$

where ρ is the density, C is the specific heat capacity, and κ is the thermal conductivity of the fiber material, all of which are assumed to be constant throughout the fiber cross section and independent of temperature. We have assumed that the longitudinal heat diffusion is negligible compared to the transverse heat diffusion, and hence we have omitted the z derivative part of the Laplacian in the heat equation. The heat source is due to the quantum defect associated with the gain medium, and the heat power density Q is related to the signal intensity I by

$$Q(\mathbf{r}, t) = \left(\frac{\lambda_s}{\lambda_p} - 1 \right) g(\mathbf{r}) I(\mathbf{r}, t), \tag{6.8}$$

where λ_s and λ_p are the signal and pump wavelengths, respectively. Fourier transforming Eq. (6.7) with respect to time yields

$$\nabla_\perp^2 \Delta T(\mathbf{r}, \omega) - q(\omega) \Delta T(\mathbf{r}, \omega) = -\frac{Q(\mathbf{r}, \omega)}{\kappa}, \tag{6.9}$$

where $q = i\rho C\omega/\kappa$. Eq. (6.9) can be solved by an appropriate Green's function G [48], and ΔT in the frequency domain is given by

$$\Delta T(\mathbf{r}, \omega) = \frac{1}{\kappa} \iint G(\mathbf{r}_\perp, \mathbf{r}'_\perp, \omega) Q(\mathbf{r}', \omega) \mathrm{d}^2 \mathbf{r}'_\perp, \tag{6.10}$$

where the Green's function satisfies the differential equation

$$\nabla_\perp^2 G(\mathbf{r}_\perp, \mathbf{r}'_\perp, \omega) - q(\omega) G(\mathbf{r}_\perp, \mathbf{r}'_\perp, \omega) = -\delta(\mathbf{r}_\perp - \mathbf{r}'_\perp). \tag{6.11}$$

The signal intensity is given by the slowly varying electric field as

$$I(\mathbf{r}, t) = \frac{1}{2} \sqrt{\varepsilon_f(\mathbf{r}_\perp)} \varepsilon_0 c E(\mathbf{r}, t) E(\mathbf{r}, t)^*, \tag{6.12}$$

which upon insertion into Eq. (6.8) and taking the Fourier transform yields

$$\begin{aligned} \Delta T(\mathbf{r}, \omega) = \frac{n_c \varepsilon_0 c}{4\pi\kappa} \left(\frac{\lambda_s}{\lambda_p} - 1 \right) g(z) \iint_{S_d} G(\mathbf{r}_\perp, \mathbf{r}'_\perp, \omega) \times \\ \int_{-\infty}^{\infty} E(\mathbf{r}'_\perp, \omega + \omega') E(\mathbf{r}', \omega')^* \mathrm{d}\omega' \mathrm{d}\mathbf{r}'_\perp. \end{aligned} \tag{6.13}$$

In the derivation of Eq. (6.13) we have assumed that the gain coefficient g is independent of time, and that it is uniform within the rare-earth doped region of the fiber core, which we denote S_d. Both these assumptions are approximations, since g is given by the population inversion of the gain medium, which depends on the signal intensity. If the signal field is composed of multiple transverse modes and frequency components, the intensity will oscillate in both space and time, and this will result in spatio-temporal oscillations in g if the signal intensity is high compared to the saturation intensity of the gain medium as shown in [37, 1]. It is clear that the minima of g will coincide with the maxima of I, and by considering Eq. (6.8) we see that neglecting the spatio-temporal oscillations of g leads to an overestimate of the oscillations in ΔT. Including the effects of gain saturation in our model leads to a much more complicated formalism, which is beyond the scope of this thesis. Nevertheless, we shall see that our simplified model explains the major qualitative features of TMI, and also provides quantitative predictions that agree reasonably well with experiments.

To derive coupled mode equations, we expand the electric field in a set of orthogonal transverse modes

$$E(\mathbf{r},\Omega) = \sum_m A_m(z,\Omega)\psi_m(\mathbf{r}_\perp)e^{-i\beta_{0,m}z}, \tag{6.14}$$

where the A_m are the slowly-varying mode amplitudes, $\beta_{0,m}$ are the propagation constants of the modes at $\omega = \omega_0$ and the normalized mode functions satisfy the eigenvalue equation

$$\nabla_\perp^2\psi_m(\mathbf{r}_\perp) + k^2\varepsilon_f(\mathbf{r}_\perp)\psi_m(\mathbf{r}_\perp) = \beta_m(\omega)^2\psi_m(\mathbf{r}_\perp), \tag{6.15}$$

where $\beta_m(\omega)$ is the propagation constant for mode m. By inserting the mode expansion in Eq. (6.14) into Eq. (6.6) and Eq. (6.13) and invoking the paraxial approximation, we can obtain a set of coupled mode equations for the mode amplitudes

$$\begin{aligned} 2i\beta_{0,n}\frac{\partial A_n}{\partial z} &= \beta_{1,n}\Omega A_n(z,\Omega) + ik_0\sum_m \alpha_{nm}A_m(z,\Omega)e^{i\Delta\beta_{nm}z} \\ &\quad + B\sum_{klm} e^{i(\Delta\beta_{nm}-\Delta\beta_{kl})z}\int_{-\infty}^{\infty} A_m(z,\Omega-\Omega')G_{nmkl}(\Omega') \\ &\quad \times \int_{-\infty}^{\infty} A_k(z,\Omega'+\Omega'')A_l(z,\Omega'')^*\mathrm{d}\Omega''\mathrm{d}\Omega'. \end{aligned} \tag{6.16}$$

In this expression, we have introduced the quantities $\Delta\beta_{nm} = \beta_{0,n} - \beta_{0,m}$ and the inverse group velocity $\beta_{1,n} = 1/v_{g,n}$. Terms involving the GVD and higher-order dispersion are neglected, since we consider signals of narrow linewidth.

Furthermore, we have introduced

$$\alpha_{nm} = n_c g(z) \iint_{S_d} \psi_n(\mathbf{r}_\perp)^* \psi_m(\mathbf{r}_\perp) \mathrm{d}^2\mathbf{r}_\perp \tag{6.17}$$

and

$$B(z) = \frac{\eta k_0^2 n_c \varepsilon_0 c}{8\pi^2 \kappa} \left(\frac{\lambda_s}{\lambda_p} - 1 \right) g(z). \tag{6.18}$$

Finally we have introduced the coupling coefficients defined by

$$G_{nmkl}(\Omega) = \iint \psi_n(\mathbf{r}_\perp)^* \psi_m(\mathbf{r}_\perp) \iint_{S_d} G(\mathbf{r}_\perp, \mathbf{r}'_\perp, \Omega) \psi_k(\mathbf{r}'_\perp) \psi_l(\mathbf{r}'_\perp)^* \mathrm{d}\mathbf{r}'_\perp \mathrm{d}\mathbf{r}_\perp, \tag{6.19}$$

where the outer integral is over the entire fiber cross section. These coupling coefficients can be evaluated numerically using standard quadrature methods for any given set of modes.

Although our model can include an arbitrary number of transverse modes, the detailed experimental analysis of TMI has shown that only the FM and the first HOMs of LMA fibers are involved, except for fibers with very large mode areas [53]. We therefore include only the fundamental LP_{01} mode and one of the two degenerate LP_{11} modes of a simple SIF. We also assume that the fiber is water cooled and the appropriate boundary condition for the heat equation at the fiber surface is therefore

$$\kappa \frac{\partial \Delta T}{\partial r} + h_q \Delta T = 0, \tag{6.20}$$

where h_q is the convection coefficient for the cooling fluid. The Green's function G is in this case given by the expansion

$$G(\mathbf{r}_\perp, \mathbf{r}'_\perp, \Omega) = \frac{1}{2\pi} \sum_{m=-\infty}^{\infty} g_m(r, r', \Omega) e^{im(\phi - \phi')}. \tag{6.21}$$

Here r, ϕ are the usual cylinder coordinates and the radial Green's functions g_m are given by

$$g_n(r, r', \Omega) = \begin{cases} I_n(\sqrt{q}r)[C_n I_n(\sqrt{q}r') + K_n(\sqrt{q}r')] & \text{for } 0 \le r < r' \\ I_n(\sqrt{q}r')[C_n I_n(\sqrt{q}r) + K_n(\sqrt{q}r)] & \text{for } r' < r \le R \end{cases}, \tag{6.22}$$

where I_n and K_n are the modified Bessel functions of the first and second kind, respectively, $q = i\rho C\Omega/\kappa$ and the coefficients C_n are given by

$$C_n = \frac{K_{n+1}(\sqrt{q}R) + K_{n-1}(\sqrt{q}R) - aK_n(\sqrt{q}R)}{I_{n+1}(\sqrt{q}R) + I_{n-1}(\sqrt{q}R) + aI_n(\sqrt{q}R)}, \tag{6.23}$$

with R being the outer radius of the fiber and $a = 2h_q/\sqrt{q}\kappa$.

Introducing scaled mode amplitudes $p_i = \sqrt{n_c\varepsilon_0 c/2}A_i$ and keeping only phase-matched terms, we obtain the coupled mode equations

$$\begin{aligned}\frac{\partial p_1}{\partial z} = &\left(\frac{n_c\Gamma_1 g}{2n_{eff,1}} - \frac{i\Omega}{v_{g,1}}\right)p_1(z,\Omega) - iK_1 g \times \Bigg(\\ &\int_{-\infty}^{\infty} p_1(z,\Omega-\Omega')G_{1111}(\Omega')C_{11}(z,\Omega')\mathrm{d}\Omega' + \\ &\int_{-\infty}^{\infty} p_1(z,\Omega-\Omega')G_{1122}(\Omega')C_{22}(z,\Omega')\mathrm{d}\Omega' + \\ &\int_{-\infty}^{\infty} p_2(z,\Omega-\Omega')G_{1212}(\Omega')C_{12}(z,\Omega')\mathrm{d}\Omega'\Bigg),\end{aligned} \tag{6.24}$$

$$\begin{aligned}\frac{\partial p_2}{\partial z} = &\left(\frac{n_c\Gamma_2 g}{2n_{eff,2}} - \frac{i\Omega}{v_{g,2}}\right)p_2(z,\Omega) - iK_2 g \times \Bigg(\\ &\int_{-\infty}^{\infty} p_2(z,\Omega-\Omega')G_{2222}(\Omega')C_{22}(z,\Omega')\mathrm{d}\Omega' + \\ &\int_{-\infty}^{\infty} p_2(z,\Omega-\Omega')G_{2211}(\Omega')C_{11}(z,\Omega')\mathrm{d}\Omega' + \\ &\int_{-\infty}^{\infty} p_1(z,\Omega-\Omega')G_{2121}(\Omega')C_{21}(z,\Omega')\mathrm{d}\Omega'\Bigg),\end{aligned} \tag{6.25}$$

where we have introduced the effective index $n_{eff,n} = \beta_{0,n}/k_0$ and the overlap integrals

$$\Gamma_n = \iint_{S_d} \psi_n(\mathbf{r}_\perp)^*\psi_n(\mathbf{r}_\perp)\mathrm{d}^2\mathbf{r}_\perp. \tag{6.26}$$

The constants K_n are given by

$$K_n = \frac{\eta\,(\lambda_s - \lambda_p)}{4\pi\kappa n_{eff,n}\lambda_s\lambda_p}, \tag{6.27}$$

and C_{ij} are given by the correlations

$$C_{ij}(z,\Omega) = \int_{-\infty}^{\infty} p_i(z,\Omega+\Omega')p_j(z,\Omega')^*\mathrm{d}\Omega'. \tag{6.28}$$

The first nonlinear term on the rhs. of Eq. (6.24) and Eq. (6.25) gives rise to intra-modal effects such as SPM and FWM. Both of these effects are governed by the real part of G_{nnnn}. The imaginary part of G_{nnnn} is responsible for a nonlinear gain on the Stokes side of the spectrum. Due to the long response

time of the thermal nonlinearity, caused by the slow heat diffusion in the fiber, the spectrum of G_{nnnn} is extremely narrow, typically on the order of 100 Hz or less, depending on fiber design.

The second nonlinear term gives rise to a cross-phase modulation (XPM) effect between the light in the two modes, and the last term is responsible, through the imaginary part of G_{nmnm}, for transfer of power between the modes, as we shall see later. Interestingly, it turns out that G_{nmnm} has a significantly wider spectrum compared to the other Green's function overlap integrals, typically on the order of a kHz, again depending on fiber design.

We note that by keeping only phase-matched terms in the coupled mode equations, we have neglected the effect of a FWM interaction between the modes, which could also potentially transfer power between them. However, this effect is highly suppressed since the GVD is far too low to provide phase-matching for the narrow-band signals we are considering.

6.2.2 Steady-state solution

It is easy to see that the coupled mode equations admit a steady-state solution given by

$$p_n(z,\Omega) = 2\pi\sqrt{P_{0,n}}\exp\left(\frac{n_c\Gamma_n}{2n_{eff,n}}\int_0^z g(z')\mathrm{d}z'\right)e^{i\Phi_n(z)}\delta(\Omega), \tag{6.29}$$

where $P_{0,n}$ is the initial power in mode n. Φ_n is the nonlinear phase

$$\Phi_1(z) = \Phi_1(0) - \left[\gamma_{11}\left(P_1(z) - P_{0,1}\right) + \gamma_{12}\left(P_2(z) - P_{0,2}\right)\right], \tag{6.30}$$

$$\Phi_2(z) = \Phi_2(0) - \left[\gamma_{22}\left(P_2(z) - P_{0,2}\right) + \gamma_{21}\left(P_1(z) - P_{0,1}\right)\right], \tag{6.31}$$

with P_n being the power in mode n

$$P_n(z) = P_{0,n}\exp\left(\frac{n_c\Gamma_n}{n_{eff,n}}\int_0^z g(z')\mathrm{d}z'\right) \tag{6.32}$$

and the nonlinear parameters γ_{nm} are given by

$$\gamma_{11} = \frac{4\pi^2 K_1 n_{eff,1}}{n_c\Gamma_1}G_{1111}(0), \tag{6.33a}$$

$$\gamma_{22} = \frac{4\pi^2 K_2 n_{eff,2}}{n_c\Gamma_2}G_{2222}(0), \tag{6.33b}$$

$$\gamma_{12} = \frac{4\pi^2 K_1 n_{eff,2}}{n_c\Gamma_2}\left[G_{1122}(0) + G_{1212}(0)\right], \tag{6.33c}$$

$$\gamma_{21} = \frac{4\pi^2 K_2 n_{eff,1}}{n_c\Gamma_1}\left[G_{2211}(0) + G_{2121}(0)\right]. \tag{6.33d}$$

From Eq. (6.11) it is seen that $G(\mathbf{r}_\perp, \mathbf{r}'_\perp, -\omega) = G(\mathbf{r}_\perp, \mathbf{r}'_\perp, \omega)^*$, from which it immediately follows that the nonlinear parameters γ_{nm} are all real. It is therefore clear that there is no transfer of power between the modes in our steady-state solution, and the only effect of the thermal nonlinearity is to cause SPM and XPM. One might therefore naively expect that our simple model is unable to explain TMI, and that more elaborate models with fewer approximations or additional physical mechanisms are required. However, as we shall show in the following, the steady-state solution is not stable, and the presence of amplitude noise will lead to a nonlinear transfer of power between the modes.

The steady-state solution given in Eq. (6.29) is of course highly idealized in the sense that the bandwidth of the signal is infinitesimally small. Actual CW laser sources have a finite bandwidth, and it is therefore of interest to examine whether a steady-state solution with a finite bandwidth exists. We consider a solution which in the time domain has the form

$$p_n(z,t) = \sqrt{P_{0,n}} \exp\left(\frac{n_c \Gamma_n}{2n_{eff,n}} \int_0^z g(z')\mathrm{d}z'\right) e^{i[\Phi_n(z)+\theta(t)]}, \tag{6.34}$$

where $\theta(t)$ is a stochastic phase which gives rise to a finite bandwidth of the CW field. It is easy to show that Eq. (6.34) is indeed a solution to the coupled mode equations, where the deterministic phase Φ_n is given by Eqs. (6.30) and (6.31). Phase noise alone is thus not sufficient to rule out a steady-state solution, but when amplitude noise is included, it is no longer possible to find a stable steady-state solution, and we therefore expect that amplitude noise, either due to quantum fluctuations or due to intensity noise of the seed laser, is responsible for TMI.

6.3 Operation at threshold

In this section, we derive approximate analytical solutions of the coupled mode equations, which are valid in cases where the average output power does not exceed the threshold for TMI. These solutions show that both quantum noise and intensity noise of the input signal can act as a seed for TMI, and thus lead to transfer of power between the FM and a HOM of the fiber. By solving the coupled mode equations numerically, we verify the validity of the approximate analytical solutions and also study the temporal dynamics of TMI.

6.3.1 Quantum noise seeding

We first consider the case where a perfectly monochromatic signal is launched in the FM of the fiber amplifier, with no signal launched in the HOM. We can

then show by solving Eqs. (6.24) and (6.25) to first order in p_2 that the presence of quantum noise in the HOM leads to a nonlinear transfer of power from the FM to the HOM, and that this transfer exhibits a threshold-like dependence on output power. In the following we have assumed that $n_{eff,1} \approx n_{eff,2} \approx n_c$ and $v_{g,1} \approx v_{g,2}$, in which case the coupled mode equations to first order in p_2 become

$$\frac{\partial p_1}{\partial z} = \frac{\Gamma_1}{2} g(z) p_1(z,\Omega) - iKg(z) \int_{-\infty}^{\infty} p_1(z,\Omega-\Omega') G_{1111}(\Omega') C_{11}(z,\Omega') \mathrm{d}\Omega', \tag{6.35}$$

$$\frac{\partial p_2}{\partial z} = \frac{\Gamma_2}{2} g(z) p_2(z,\Omega) - iKg(z) \Bigg(\int_{-\infty}^{\infty} p_2(z,\Omega-\Omega') G_{2211}(\Omega') C_{11}(z,\Omega') \mathrm{d}\Omega' + \int_{-\infty}^{\infty} p_1(z,\Omega-\Omega') G_{2121}(\Omega') C_{21}(z,\Omega') \mathrm{d}\Omega' \Bigg), \tag{6.36}$$

where $K = K_1 \approx K_2$ and the group velocity term has been transformed away by shifting to a frame moving with the group velocity. We take the solution of Eq. (6.35) to be the CW solution given by Eq. (6.29). Inserting this solution into Eq. (6.36) we obtain

$$\frac{\partial |p_2|^2}{\partial z} = \left[\Gamma_2 + \chi(\Omega) P_1(z) \right] g(z) |p_2(z,\Omega)|^2, \tag{6.37}$$

where $\chi(\Omega) = 4\pi^2 K \mathrm{Im}[G_{2121}(\Omega)]$ and $P_1(z)$ is given by Eq. (6.32). We can solve this differential equation to obtain the energy spectral density in the HOM at the output

$$|p_2(L,\Omega)|^2 = |p_2(0,\Omega)|^2 \exp\left(\Gamma_2 g_{av} L\right) \exp\left[\frac{\chi(\Omega)}{\Gamma_1} \left(P_1(L) - P_{0,1} \right) \right], \tag{6.38}$$

where L is the length of the fiber and the average gain coefficient is given by

$$g_{av} = \frac{1}{L} \int_0^L g(z) \mathrm{d}z. \tag{6.39}$$

It is clear from the solution given by Eq. (6.38) that any frequency components present in the HOM for which $\chi > 0$ will experience a nonlinear gain in addition to the gain provided by the rare-earth doping. While we have assumed that no signal is launched into the HOM, quantum fluctuations of the field will always be present, and certain frequency components of this quantum noise can thus

experience nonlinear gain. Writing the solution in terms of the power spectral density (PSD) S_n of mode n, we have

$$S_2(L,\Omega) = S_2(0,\Omega)\exp\left(\Gamma_2 g_{av} L\right)\exp\left[\frac{\chi(\Omega)}{\Gamma_1}\left(P_1(L) - P_{0,1}\right)\right]. \tag{6.40}$$

To model the influence of quantum noise, we use the approach in [30] and define an equivalent input PSD of the quantum noise as $S_2(0,\Omega) = \hbar(\omega_0 + \Omega)$. The total output power in the HOM is thus given by

$$P_2(L) = \exp\left(\Gamma_2 g_{av} L\right)\int_{-\infty}^{\infty} \hbar(\omega_0+\Omega)\exp\left[\frac{\chi(\Omega)}{\Gamma_1}\left(P_1(L) - P_{0,1}\right)\right]\mathrm{d}\Omega. \tag{6.41}$$

As a specific example, we consider an Yb-doped SIF with a core radius $R_c = 20$ μm, a core refractive index $n_c = 1.45$ and with a V parameter of 3. This fiber thus supports the fundamental LP_{01} mode as well as the degenerate LP_{11} modes. Although actual double-clad fiber amplifiers have both an inner and outer cladding, we assume for simplicity that the radius of the inner cladding is sufficiently large that the index step associated with the inner/outer cladding boundary has a negligible impact on the modes guided in the core. The outer radius of the fiber $R = 500$ μm and the convection coefficient of the cooling fluid $h_q = 1000$ W/(m^{2}K). Since we are considering an Yb-doped fiber amplifier, we take the pump wavelength to be 975 nm and the launched signal wavelength to be 1032 nm. We shall refer to this fiber amplifier as Fiber A, and the parameters are summarized in Table 6.1.

Table 6.1: Parameters of Fiber A.

R_c	20 μm
R	500 μm
n_c	1.45
V	3
λ_s	1032 nm
λ_p	975 nm
h_q	1000 W/(m^{2}K)
η	3.5×10^{-5} K^{-1}
κ	1.4 W/(Km)
ρC	1.67×10^6 J/(Km^3)

To calculate the nonlinear coupling coefficient χ we insert $\psi_1(r,\phi) = R_1(r)$ and $\psi_2(r,\phi) = R_2(r)\cos\phi$ into Eq. (6.19), where R_1 and R_2 are the radial mode functions for the LP_{01} and LP_{11} modes, respectively. Using the expansion for

the Green's function given in Eq. (6.21) we obtain an expression for G_{2121}

$$G_{2121}(\Omega) = \pi \int_0^R R_1(r) R_2(r) r \int_0^{R_c} R_1(r') R_2(r') g_1(r, r', \Omega) r' \mathrm{d}r' \mathrm{d}r. \quad (6.42)$$

This double integral is evaluated by standard numerical quadrature methods for a range of frequencies, and the nonlinear coupling coefficient χ is calculated using $\eta = 3.5 \times 10^{-5}$ K^{-1}, $\kappa = 1.4$ W/(Km) and $\rho C = 1.67 \times 10^6$ J/(Km^3). The result, shown in Fig. 6.1, shows that χ is positive for negative values of Ω and has a sharp peak at $\Omega/2\pi \approx 1$ kHz.

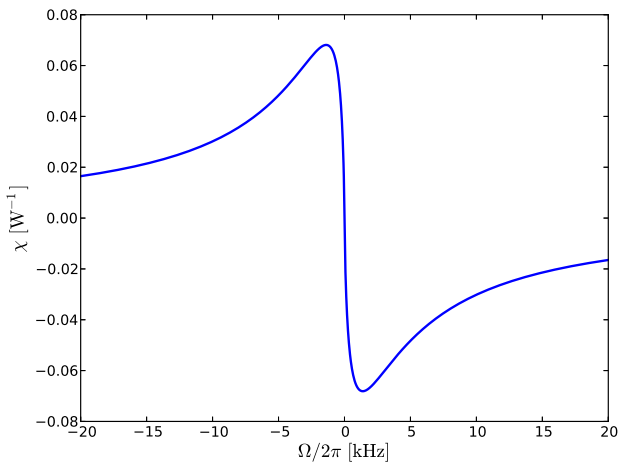

Figure 6.1: Nonlinear coupling coefficient χ for $LP_{01} - LP_{11}$ coupling as a function of Ω for Fiber A.

Defining the HOM content as $\xi = P_2/(P_1 + P_2)$ we find from Eq. (6.41)

$$\xi(L) \approx \frac{\hbar\omega_0}{P_{0,1}} \exp\left(-\Delta\Gamma g_{av} L\right) \int_{-\infty}^{\infty} \exp\left[\frac{\chi(\Omega)}{\Gamma_1}\left(P_1(L) - P_{0,1}\right)\right] \mathrm{d}\Omega, \quad (6.43)$$

where $\Delta\Gamma = \Gamma_1 - \Gamma_2$ and we have used the fact that the dominant contribution to the integral comes from the narrow region around the peak in χ to make the approximation $\omega_0 + \Omega \approx \omega_0$. This fact also allows us to use Laplace's method to evaluate the integral, which yields

$$\xi(L) \approx \hbar\omega_0 \sqrt{\frac{2\pi\Gamma_1}{|\chi''(\Omega_p)|}} \frac{P_1(L)^{(\Gamma_2/\Gamma_1 - 3/2)}}{P_{0,1}^{\Gamma_2/\Gamma_1}} \exp\left[\frac{\chi(\Omega_p)}{\Gamma_1}\left(P_1(L) - P_{0,1}\right)\right], \quad (6.44)$$

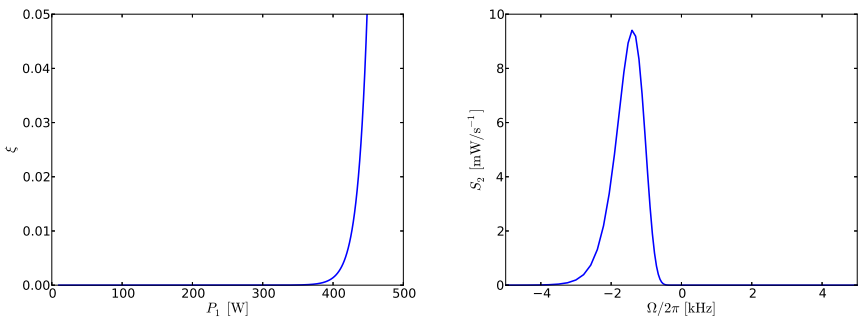

(a) HOM content (b) HOM power spectral density

Figure 6.2: (a) Output HOM content ξ as a function of output power in the FM P_1 and (b) output PSD of the HOM of Fiber A. The input power in the FM $P_1(0) = 1$ W.

where χ'' denotes the second derivative of χ with respect to Ω, and Ω_p denotes the frequency of the maximum of χ. Assuming an input power of 1 W in the FM, the HOM content is plotted as a function of output power in the FM in Fig. 6.2a and clearly shows a threshold-like behavior near a FM output power of approximately 450 W. Defining a threshold output power P_{th} as the output power for which $\xi = 0.05$, we find $P_{th} = 448$ W by a numerical solution of Eq. (6.44). The PSD of the output signal in the HOM is given by Eq. (6.40) and is shown in Fig. 6.2b for a FM output power $P_1(L) = P_{th}$. It is evident that the light is redshifted by approximately 1.5 kHz relative to the light in the FM, which corresponds to the peak in the nonlinear coupling coefficient χ.

Since the light generated in the HOM is redshifted and has a finite spectral width, both of which are determined by the shape of the spectrum of χ, the interference between the remaining light in the FM and the light in the HOM is expected to display a complicated temporal behavior. It is evident from Eq. (6.42) that the nonlinear coupling coefficient χ depends on the shape of the mode functions, and thus on the fiber design, and hence the temporal dynamics of TMI is different for different fiber amplifiers. The dependence of the spectral properties of χ on the core diameter and V parameter of a SIF was investigated in [2] where it was found that the frequency and width of the peak of χ decrease with increasing core diameter, and that the maximum value of χ decreases with decreasing V parameter. The temporal dynamics of TMI is therefore expected to be slower for fibers with larger core diameter, and the threshold is expected to be higher for fibers with lower V parameter.

To investigate the impact of cooling efficiency on TMI, we have calculated χ for $h_q = 10$ W/(m^{2}K), corresponding to passive air cooling, and $h_q = 10^4$ W/(m^{2}K), corresponding to very efficient water cooling. The results are indistinguishable from Fig. 6.1, which means that the TMI threshold and spectral properties are predicted to be exactly the same. This is a surprising result in light of experimental results presented in [54], which shows a higher threshold for an efficiently cooled fiber compared to an air-cooled fiber. We note that our calculations assume symmetric cooling of the fiber, which is not always the case experimentally. An asymmetric cooling of the fiber, such as e.g. when the fiber is attached to a heat sink, could lead to an overall temperature gradient, which would distort the mode profiles and thus alter the nonlinear coupling coefficient between the modes. Our calculations also assume that fiber parameters such as density, heat capacity, thermal conductivity and thermo-optic coefficient are temperature independent, and since the overall temperature of the fiber depends greatly on the cooling efficiency, this assumption may not be valid. In particular, the thermo-optic coefficient of fused silica may in fact increase with increasing temperature [56], leading to a reduction in TMI threshold.

6.3.2 Intensity noise seeding

While we have shown that pure phase noise in the input signal does not induce TMI, we will now show that the presence of intensity noise in the input signal can act as a seed for TMI, provided that a small amount of the signal is launched in the HOM. To do this, we consider the coupled mode equations to first order in p_2 given by Eq. (6.35) and Eq. (6.36). We assume that the signal launched into each mode is given in the time domain by

$$p_n(0,t) = \sqrt{P_{0,n}\left(1+\epsilon_N(t)\right)}e^{i\Phi_n(0)} \approx \sqrt{P_{0,n}}\left(1+\frac{1}{2}\epsilon_N(t)\right)e^{i\Phi_n(0)}, \quad (6.45)$$

where ϵ_N is a zero-mean random variable representing the intensity noise of the input signal, and we further assume that $|\epsilon_N| \ll 1$.

We again take the zeroth-order solution to the FM signal to be the CW solution given in Eq. (6.29) and can then derive the PSD of the output signal in the HOM, given by Eq. (6.40). The input PSD in the HOM is given by

$$S_2(0,\Omega) = \frac{1}{2\pi}\int_{-\infty}^{\infty}\langle p_2(0,t)p_2(0,t+t')^*\rangle e^{-i\Omega t'}\,\mathrm{d}t', \quad (6.46)$$

where $\langle p_2(0,t)p_2(0,t+t')^*\rangle$ is the autocorrelation function of the input signal in the HOM. Using Eq. (6.45) the PSD of the input signal in the HOM can be written as

$$S_2(0,\Omega) = P_{0,2}\delta(\Omega) + \frac{1}{4}R_N(\Omega)P_{0,2}, \quad (6.47)$$

where R_N is the relative intensity noise (RIN) of the input signal, and is given by

$$R_N(\Omega) = \frac{1}{2\pi}\int_{-\infty}^{\infty} \langle \epsilon_N(t)\epsilon_N(t+t')\rangle e^{-i\Omega t'}\,\mathrm{d}t'. \tag{6.48}$$

Inserting the input PSD given in Eq. (6.47) into Eq. (6.40) yields the output PSD in the HOM

$$S_2(L,\Omega) = P_{0,2}\exp\left(\Gamma_2 g_{av} L\right)\left[\delta(\Omega) + \frac{1}{4}R_N(\Omega)\exp\left(\frac{\Delta P_1}{\Gamma_1}\chi(\Omega)\right)\right], \tag{6.49}$$

where $\Delta P_1 = P_1(L) - P_{0,1}$. The total output power in the HOM $P_2(L)$ is then found by integrating $S_2(L,\Omega)$ over all frequencies. In terms of the HOM content ξ we find

$$\xi(L) = \xi(0)\exp\left(-\Delta\Gamma g_{av} L\right)\left(1 + \frac{1}{4}\int_{-\infty}^{\infty} R_N(\Omega)\exp\left(\frac{\Delta P_1}{\Gamma_1}\chi(\Omega)\right)\mathrm{d}\Omega\right). \tag{6.50}$$

Since the main contribution to the integral comes from the narrow frequency range around the maximum of χ, we can assume that the RIN is independent of frequency and use Laplace's method to evaluate the integral. This yields

$$\begin{aligned}\xi(L) \approx \xi(0)\left(\frac{P_{0,1}}{P_1(L)}\right)^{1-\frac{\Gamma_2}{\Gamma_1}} \times \\ \left[1 + \frac{1}{4}R_N(\Omega_p)\sqrt{\frac{2\pi\Gamma_1}{P_1(L)|\chi''(\Omega_p)|}}\exp\left(\frac{\Delta P_1}{\Gamma_1}\chi(\Omega_p)\right)\right],\end{aligned} \tag{6.51}$$

where we have used the approximation $\Delta P_1 \approx P_1(L)$ in the denominator in the second term. We have plotted the HOM content as a function of output power in the FM $P_1(L)$ for Fiber A in Fig. 6.3 assuming an initial HOM content $\xi(0) = 0.01$, an initial FM input power $P_{0,1} = 1$ W and three different values of the RIN R_N: 10^{-13} Hz^{-1}, 10^{-12} Hz^{-1} and 10^{-11} Hz^{-1}. In the same figure, we have plotted the HOM content for quantum noise seeding for comparison. The threshold powers for TMI in each case of intensity noise seeding are found to be 351 W, 320 W and 288 W, respectively, which is significantly lower than the 448 W found for the quantum noise seeded case, but still on the same order of magnitude.

From Eq. (6.51) we see that the threshold power has an approximately logarithmic dependence on the RIN, and measures taken to reduce the intensity noise of the input signal are therefore expected to result in only modest improvements in the TMI threshold. The same is true for the dependence of the TMI threshold on the initial HOM content $\xi(0)$, which explains why efforts to optimize the in-coupling of the signal are found to have little impact on the TMI threshold in experiments.

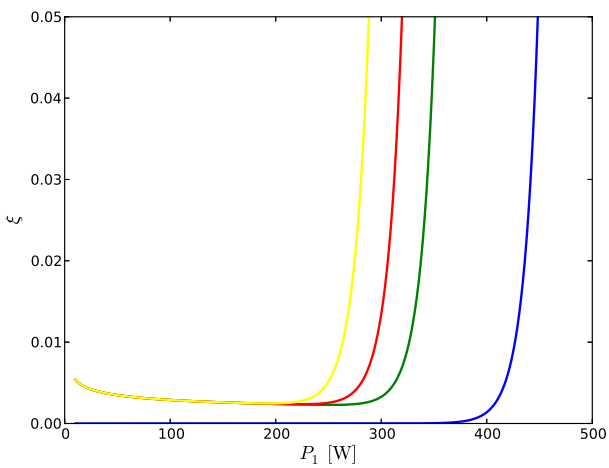

Figure 6.3: Output HOM content as a function of FM output power for intensity noise seeding of Fiber A with a RIN of 10^{-13} Hz^{-1} (green curve), 10^{-12} Hz^{-1} (red curve) and 10^{-11} Hz^{-1} (yellow curve). Quantum noise seeding (blue curve) is shown for comparison. The input power in the FM $P_{0,1} = 1$ W and the initial HOM content $\xi(0) = 0.01$.

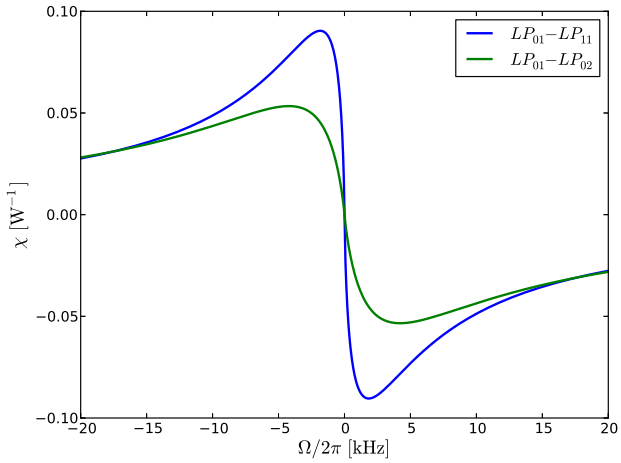

Figure 6.4: Nonlinear coupling coefficient χ for $LP_{01} - LP_{11}$ coupling (blue curve) and $LP_{01} - LP_{02}$ coupling (green curve) for a SIF with $V = 5$ and all other parameters the same as Fiber A. The peak value is seen to be higher for $LP_{01} - LP_{11}$ coupling, leading to a lower threshold power for this process.

6.3.3 $LP_{01} - LP_{02}$ coupling

So far we have only considered coupling between LP_{01} and LP_{11}. However, some large-core fibers may support additional guided modes, such as LP_{02}-like modes, in particular for operating powers for which the thermo-optic effect is strong enough to significantly alter the guiding properties of the fiber [1]. While the presence of an additional LP_{31} mode has been reported in TMI of a LPF with a mode field diameter of 75 μm [53], LP_{02}-like modes have as yet not been observed to take part. To investigate this, we have calculated the nonlinear coupling coefficients for both $LP_{01} - LP_{11}$ coupling and $LP_{01} - LP_{02}$ coupling for a SIF with a V parameter of 5 and all other parameters the same as Fiber A. The result is presented in Fig. 6.4 and clearly shows that the nonlinear gain of the $LP_{01} - LP_{02}$ coupling is much less than for the $LP_{01} - LP_{11}$ coupling in this case. Calculating the quantum noise seeded threshold power for a threshold HOM content $\xi_{th} = 0.05$, we find $P_{th} = 350$ W and $P_{th} = 608$ W for the two cases. It is thus not surprising that an LP_{02}-like mode has not been observed to take part in TMI, as the coupling to the LP_{11}-like modes must be expected to be much stronger.

6.3.4 Numerical results

The results presented so far are based on approximate solutions of the coupled mode equations, and it is therefore of interest to compare these solutions to a full numerical solution of the coupled mode equations. In particular, our semi-analytical results are based on the assumption of a perfectly monochromatic signal. As can be seen from Fig. 6.1 the nonlinear coupling coefficient χ has a very narrow spectrum on the order of a few kHz, which is comparable to the linewidth of typical single-frequency fiber laser sources. We shall therefore use a numerical solution to study the effect of a finite signal linewidth on the TMI threshold.

Our implementation of the numerical solution of the coupled mode equations, Eq. (6.24) and Eq. (6.25), is straightforward. We use a standard ODE integrator [57] to step the solution forward in z and the correlations are computed using fast Fourier transforms. While it would be possible in principle to include rate equations to determine the z-dependence of the gain coefficient $g(z)$, we have chosen to consider a simplified case in which $g(z)$ is constant. The analytical results derived in the previous sections showed that the power threshold for TMI was only dependent on the total gain. While this is only strictly true when rapid spatio-temporal oscillations of g can be neglected, we nevertheless believe that the numerical results derived with a constant gain are sufficiently accurate to provide valuable insight into the dynamics of the TMI phenomenon.

We consider a SIF with the same parameters as Fiber A for all the results in this section, and consider coupling between LP_{01} and one of the two degenerate LP_{11} modes. For the input signal, we assume a CW signal with only phase noise to which we add random quantum noise by injecting one photon per mode [30]. The phase noise of the input signal is modeled in the time domain as

$$p_n(0,t) = \sqrt{P_{0,n}} e^{i(\Phi_n(0)+\theta(t))}, \tag{6.52}$$

where $\theta(t)$ is the result of a Gaussian random walk. This phase noise model provides a signal with a constant amplitude but with a Lorentzian lineshape.

To investigate the influence of the signal bandwidth on the TMI threshold, we have run simulations for input signal bandwidths of 1 Hz, 1 kHz and 10 kHz (FWHM). In all cases, the input signal power $P_{0,1} = 1$ W for the FM and $P_{0,2} = 0$ W for the HOM. The fiber length $L = 1$ m and the gain coefficient $g = \ln(500)/(\Gamma_1 L)$. In the absence of any nonlinear mode coupling, the fiber amplifier should thus provide 27 dB gain. Fig. 6.5 shows the output PSD for the FM and HOM for all three simulations. The HOM spectrum for the 1 Hz case, plotted in Fig. 6.5b shows the presence of light redshifted relative to the FM by approximately 1.5 kHz, corresponding to the peak of the nonlinear

coupling coefficient shown in Fig. 6.1. The shape of the spectrum also agrees well with what is seen in Fig. 6.2b.

For the 1 kHz case, the HOM light is seen to experience a redshift of approximately 1.5 kHz as in the 1 Hz case, and is also spectrally broadened, although the latter effect is less visible due to the width of the input signal. The redshift is also present in the 10 kHz case, but is hardly noticeable on the plot due to the larger spectral width of the input signals.

The HOM content ξ and the average power in each mode as a function of z for the 10 kHz input signal linewidth case are plotted in Fig. 6.6 and shows that the TMI threshold is reached when the power in the FM reaches approximately 450 W, in good agreement with our semi-analytical result in the previous section. The results for the 1 Hz and 1 kHz cases are indistinguishable from this case, and are thus not shown.

In order to investigate the temporal dynamics of TMI, we plot the squared norm of the time-domain mode amplitudes at the output $|p_n(L,t)|^2$, which gives the instantaneous power in mode n. These are plotted in Fig. 6.7 for the 1 Hz input signal linewidth case and shows a rather chaotic fluctuation of power between the FM and the HOM on a timescale of a few ms, which is what would be expected from the width and redshift of the spectrum in Fig. 6.5b. It is also consistent with recent experimental findings [55], which showed that TMI in a Yb-doped PCF amplifier with a core diameter of 38 μm manifested itself as a chaotic oscillation of the beam intensity on a ms timescale. The results for the 1 kHz and 10 kHz cases display a similar behavior and are therefore not reproduced here.

Considering the results of our simulations, it appears that the bandwidth of the signal does not influence the TMI threshold or the temporal dynamics of the mode fluctuations to any great extent, which is also consistent with experiments [54].

6.4 Operation beyond threshold

We now investigate the behavior of the output signal when a fiber amplifier is operated above the TMI threshold. Since the perturbative approach presented in section 6.3 is invalid in cases where the power in the HOM becomes comparable to the power in the FM, we investigate this regime by numerically solving the coupled mode equations for 1 m of Fiber A, but with a higher gain coefficient $g = \ln(1000)/(\Gamma_1 L)$. We consider a case in which the input signal power is 1 W and the signal linewidth is 1 kHz. We further assume that the signal is launched into the FM, with no signal launched in the HOM, and add quantum noise to this signal.

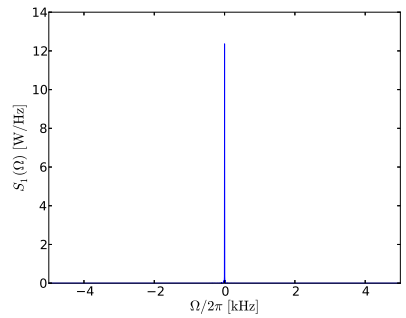

(a) FM spectrum, 1 Hz

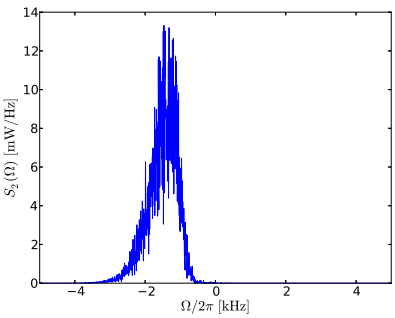

(b) HOM spectrum, 1 Hz

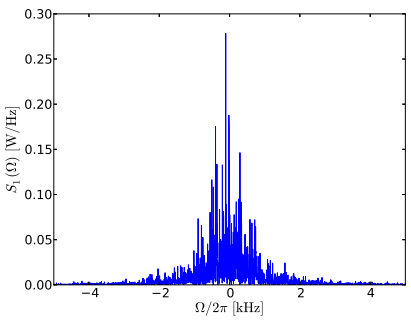

(c) FM spectrum, 1 kHz

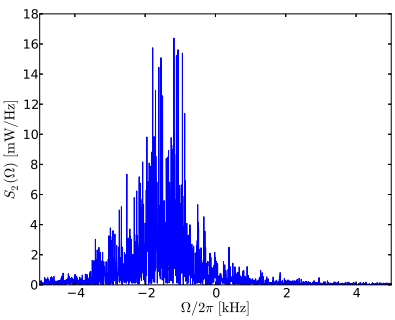

(d) HOM spectrum, 1 kHz

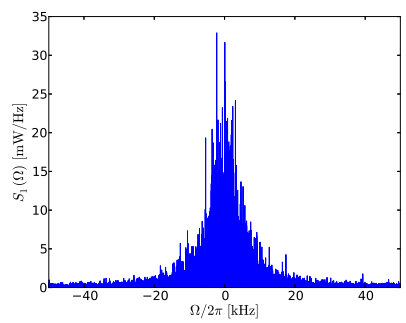

(e) FM spectrum, 10 kHz

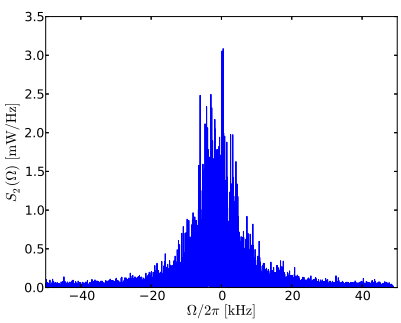

(f) HOM spectrum, 10 kHz

Figure 6.5: Output PSD of the light in LP_{01} and LP_{11} of 1 m of Fiber A with $g = \ln(500)/\Gamma_1$ m^{-1}. The input signal is a CW signal with a linewidth due to phase noise of 1 Hz (a,b), 1 kHz (c,d) and 10 kHz (e,f), and the input power in the FM is 1 W. Quantum noise acts as a seed for TMI, which is seen as the presence of the redshifted light in the HOM.

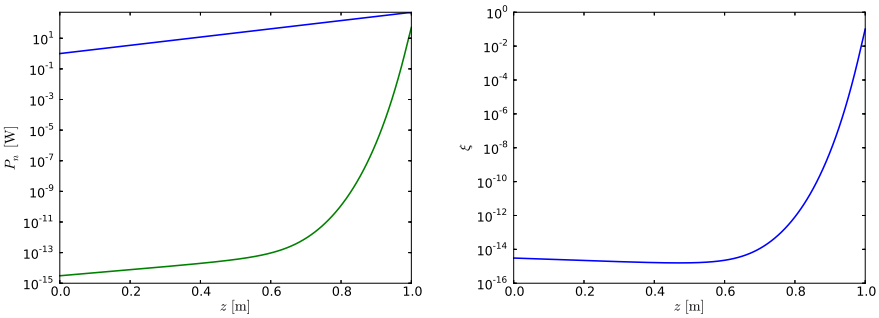

(a) Mode power (b) HOM content

Figure 6.6: (a) Average mode power P_n of the FM (blue curve) and HOM (green curve), and (b) HOM content ξ as a function of z for the fiber amplifier described in Fig. 6.5 with an input signal linewidth of 10 kHz. The results for the 1 Hz and 1 kHz cases are indistinguishable from the 10 kHz case.

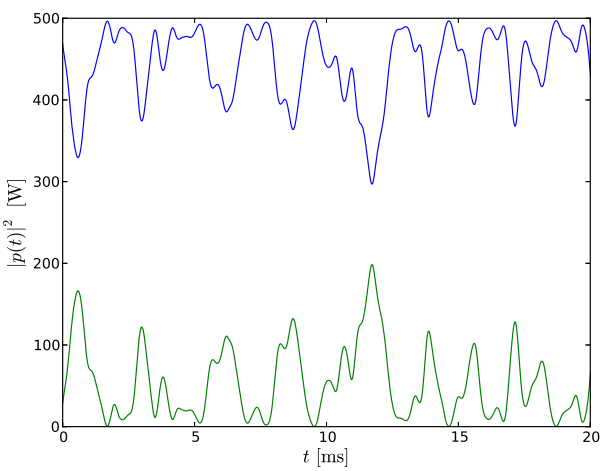

Figure 6.7: Instantaneous mode power at the fiber output $|p_n(L,t)|^2$ as a function of time for the fiber amplifier described in Fig. 6.5. The signal power is seen to fluctuate between the FM (blue curve) and HOM (green curve) in a chaotic fashion on a ms timescale.

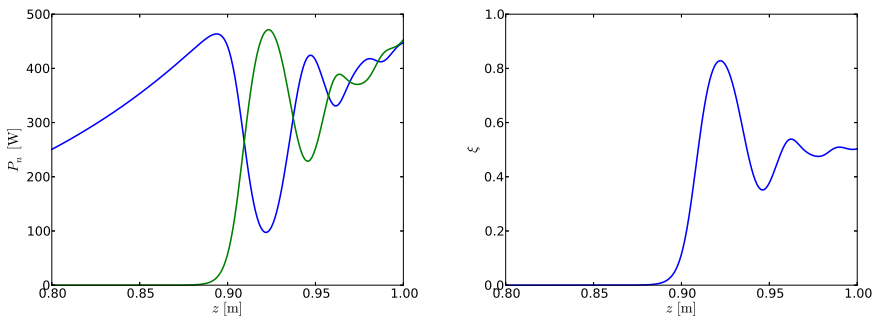

(a) Mode power

(b) HOM content

Figure 6.8: (a) Average mode power of the FM (blue curve) and HOM (green curve), and (b) HOM content as a function of z for Fiber A with $g = \ln(1000)/\Gamma_1$ m^{-1}. The input signal is a CW signal with a linewidth due to phase noise of 1 kHz, and the input power in the FM / HOM is 1 W / 0 W, with quantum noise added to both modes. The HOM content is seen to converge to 0.5 as the signal power increases beyond the TMI threshold.

Considering the average mode power and HOM content as a function of z, shown in Fig. 6.8, we see that the HOM content increases dramatically as the TMI threshold is reached. At this power level, power is thus transferred from the FM to the HOM. This transfer proceeds until the HOM content reaches approximately 0.8, at which point the process is reversed and power is transferred back to the FM from the HOM. The power flow between the modes quickly reverses again, however, and the HOM content appears to converge to 0.5 as the total signal power increases.

The output PSD of the light in the FM and HOM is shown in Fig. 6.9. It is seen that the light in both modes is now significantly redshifted relative to the input signal, and that the FM spectrum has undergone significant broadening. This broadening, which was absent in the simulations for the amplifier operating at the threshold power, can be explained by considering the power flow reversals between the modes described above. The light in the HOM is initially seeded by quantum noise and thus has a spectral width which is determined by the bandwidth of the nonlinear gain, since the bandwidth of the FM light is comparable to the nonlinear gain bandwidth. As the output power increases beyond the TMI threshold and the power flow between the modes reverses, the relatively broadband light in the HOM is coupled back into the nearly depleted FM. With each reversal of the power flow, the light is redshifted and also

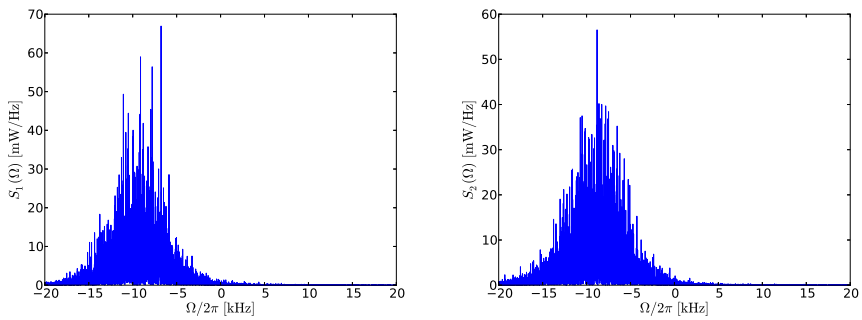

(a) FM spectrum (b) HOM spectrum

Figure 6.9: Output PSD of the light in (a) LP_{01} and (b) LP_{11} of the SIF amplifier descibed in Fig. 6.8. Quantum noise acts as a seed for TMI, and the multiple power flow reversals between the modes result in an additional redshift and spectral broadening of the output signal.

additionally broadened due to the nonlinear gain, and the end result is that the light in both modes is redshifted and spectrally broadened relative to the input. We have tested that the redshift is indeed due to the coupling between the modes by removing the quantum noise from the simulation, in which case no power transfer between the modes occurred and no spectral broadening was observed.

The temporal dynamics of the TMI is again studied by plotting the instantaneous mode power of each mode as a function of time, which is shown if Fig. 6.10. The mode fluctuations are chaotic and the characteristic timescale is somewhat shorter compared to the result for operation at the TMI threshold shown in Fig. 6.7. This shorter timescale of the mode fluctuations is most likely a result of the additional spectral broadening of the light, which we discussed above. We also note that a complete transfer between the modes can occur on a sub-ms timescale. Such a complete transfer of power between the modes has been experimentally observed in [52].

6.5 Amplitude modulated input signal

We shall now consider what happens if the input signal contains a small amplitude modulation with a modulation frequency close to the frequency of the peak of the nonlinear coupling coefficient. The modulation frequencies we con-

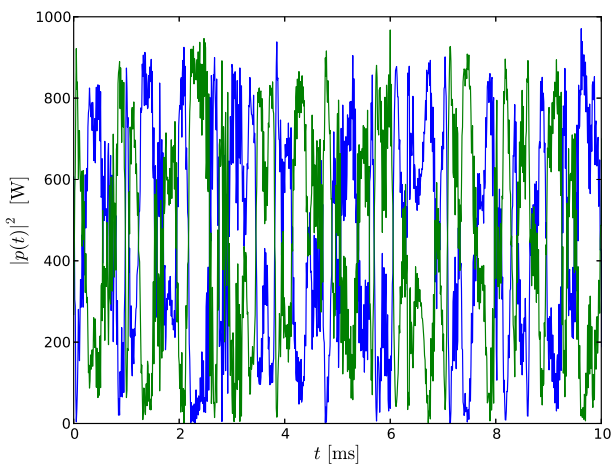

Figure 6.10: Instantaneous mode power at the fiber output $|p_n(L,t)|^2$ as a function of time for the fiber amplifier described in Fig. 6.8. The signal power is seen to fluctuate between the FM (blue curve) and HOM (green curve) in a chaotic fashion on a ms timescale. Note that a full transfer of power between the modes occurs on a sub-ms timescale.

sider would thus be in the range of a few 100 Hz to a few kHz, depending on the fiber core diameter [2]. Amplitude modulations in this frequency range can be caused by various external electrical or mechanical disturbances [58], and may also act as a seed for TMI.

6.5.1 Perturbative calculation

In terms of our coupled mode model, we consider input mode amplitudes in the time domain on the form

$$p_n(0,t) = \sqrt{P_{0,n}}\left[1 + a\sin(\Omega_m t)\right], \tag{6.53}$$

where a is the modulation depth relative to the average amplitude of the mode, Ω_m is the angular modulation frequency and we assume $a \ll 1$. We again employ the perturbative solution to the coupled mode equations used in section 6.3, with the output PSD in the HOM $S_2(L,\Omega)$ given by Eq. (6.40). We find the input PSD in the HOM $S_2(0,\Omega)$ by inserting Eq. (6.53) into Eq. (6.46) which gives

$$S_2(0,\Omega) = P_{0,2}\delta(\Omega) + \frac{P_{0,2}a^2}{4}\left[\delta\left(\Omega - \Omega_m\right) + \delta\left(\Omega + \Omega_m\right)\right]. \tag{6.54}$$

The harmonic modulation of the mode amplitude gives rise to sidebands in the spectrum which are offset from the carrier by Ω_m.

Inserting Eq. (6.54) into Eq. (6.40) and integrating over Ω yields the average output power in the HOM

$$P_2(L) \approx P_{0,2}\exp\left(\Gamma_2 g_{av} L\right)\left[1 + \frac{a^2}{4}\exp\left(\frac{\chi(-\Omega_m)}{\Gamma_1}\left(P_1(L) - P_{0,1}\right)\right)\right], \tag{6.55}$$

where we have ignored the term with $\chi(\Omega_m) = -\chi(-\Omega_m)$ arising from the first delta-function in Eq. (6.54), since this term is very small. Dividing by the total output power, we find the output HOM content

$$\xi(L) \approx \xi(0)\left(\frac{P_{0,1}}{P_1(L)}\right)^{1-\frac{\Gamma_2}{\Gamma_1}}\left[1 + \frac{a^2}{4}\exp\left(\frac{\chi(-\Omega_m)}{\Gamma_1}\left(P_1(L) - P_{0,1}\right)\right)\right]. \tag{6.56}$$

To investigate the sensitivity of the threshold power to the modulation depth a, we have calculated the threshold power for Fiber A for three different values of a: 10^{-4}, 10^{-5} and 10^{-6}. The corresponding TMI thresholds are: 309 W, 372 W, and 434 W. In all three cases, the modulation frequency $\Omega_m/2\pi = 1$ kHz, $\xi(0) = 0.01$ and $P_{0,1} = 1$ W. The threshold criterium was $\xi = 0.05$, the same as was used for quantum noise and RIN seeding. The output HOM content

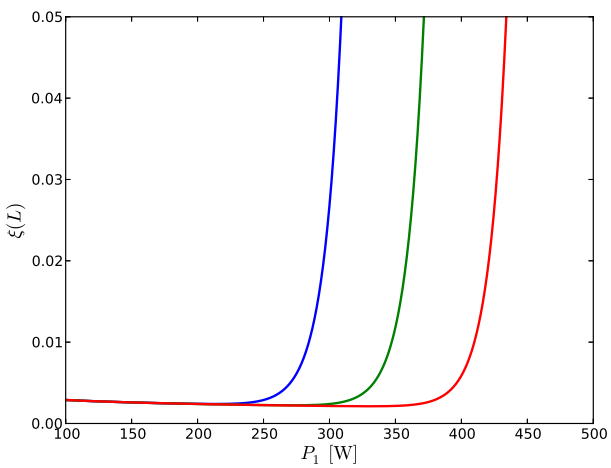

Figure 6.11: Output HOM content as a function of FM output power for Fiber A. The TMI is seeded by a sinusoidal modulation of the input mode amplitude with a modulation frequency $\Omega_m/2\pi = 1$ kHz and modulation depth a of: 10^{-4} (blue curve), 10^{-5} (green curve), 10^{-6} (red curve). The input HOM content $\xi(0) = 0.01$ and the input FM power $P_{0,1} = 1$ W.

as a function of FM output power for the three values of modulation depth is plotted in Fig. 6.11. From Eq. (6.56) it is clear that the TMI threshold has an approximately logarithmic dependence on the modulation depth, which is also seen in Fig. 6.11. As was the case for RIN seeding, the same is true for the dependence on the input HOM content $\xi(0)$.

6.5.2 Numerical results

To check the validity of the approximate solution given in Eq. (6.56) and to investigate the TMI behavior beyond threshold when the input signal contains a small harmonic amplitude modulation, we have solved the coupled mode equations numerically using the same method as in section 6.3.4. The input mode amplitudes in the time domain are given by

$$p_n(0,t) = \sqrt{P_{0,n}}\,[1 + a\sin(\Omega_m t)]\,e^{i[\Phi_n(0)+\theta(t)]}. \tag{6.57}$$

In addition to the signal, we added random quantum noise to the input mode amplitudes. The fiber parameters were those of Fiber A, but in order to accentuate the effects of the intensity modulation, we have chosen to model a signal with a very narrow linewidth of 1 Hz. In the simulations presented here, the modulation depth $a = 10^{-4}$ and the modulation frequency $\Omega_m/(2\pi) = 1$ kHz. The input signal powers were $P_{0,1} = 0.99$ W and $P_{0,2} = 0.01$ W.

We first performed a simulation in which the fiber amplifier is operating at the TMI threshold. The gain coefficient is therefore set to $g = \ln(350)/(\Gamma_1 L)$, which provides a gain sufficient to reach the threshold power. The mode power and HOM content as a function of z are plotted in Fig. 6.12 and shows that the TMI threshold is reached when the output FM power is approximately 325 W. The approximate semi-analytical calculation of 309 W thus slightly underestimates the threshold power in this case.

The output PSD of the FM and HOM are shown in Fig. 6.13. It is clear that the HOM Stokes sideband due to the amplitude modulation has acted as a seed for the TMI and experienced a significant nonlinear gain, since the strong FM carrier component is able to couple efficiently to this sideband and power is transferred from the FM carrier to the HOM Stokes sideband. On the other hand, the HOM anti-Stokes sideband is depleted, since it couples to the strong FM carrier, but the direction of the transfer of power is from the HOM to the FM. This additional transfer of power from the HOM to the FM is not taken into account in the approximate semi-analytical calculation, and may partly explain why this calculation underestimates the FM power at the TMI threshold.

We also see the appearance of an additional Stokes sideband at $\Omega = -2\Omega_m$ in the HOM. The seed for this additional sideband is most likely due to intra-

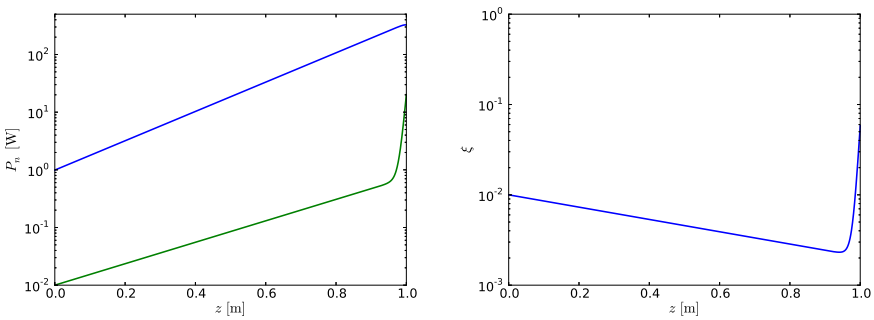

(a) Mode power (b) HOM content

Figure 6.12: (a) Average mode power P_n and (b) HOM content ξ as a function of z for 1 m of Fiber A with $g = \ln(350)/\Gamma_1$ m^{-1}. The input signal is an amplitude modulated signal with a linewidth due to phase noise of 1 Hz, a modulation depth $a = 10^{-4}$ and a modulation frequency $\Omega_m/(2\pi) = 1$ kHz. The input power in the FM / HOM is 0.99 W / 0.01 W.

modal FWM between the sidebands and carrier of the HOM. The FWM process can generate additional sidebands at $\Omega = \pm 2\Omega_m$, and the second Stokes sideband at $\Omega = -2\Omega_m$ can then be amplified by the nonlinear gain provided by the presence of the strong FM carrier. We have tested this hypothesis by simulating the amplitude modulated signal in the HOM only, without any quantum noise and no signal in the FM. The output signal in this case shows the presence of additional symmetrically distributed sidebands at the second harmonic of the modulation frequency.

Recent experiments have utilized a beam aperture measurement to investigate the temporal dynamics of TMI, in which the intensity in a small part of the output beam near field image is measured by a fast photo-diode [53, 54, 55]. The idea is that the temporal mode fluctuations result in an intensity variation, which is then recorded and analyzed. In the experiments by Otto *et al.* [53] and Ward *et al.* [54], a transition region was found in which the aperture intensity measurements showed a harmonic behavior when the fiber amplifier was operated close to the TMI threshold. On the other hand, no such behavior was found by Karow *et al.* [55].

To compare our simulations with these experiments, we calculate the intensity of the output beam at a fixed point in the beam profile and plot the corresponding normalized frequency spectrum $|I(\Omega)|/|I(0)|$. The intensity is calculated at a point located at $r = 20$ μm, $\phi = 0$, so that the interference be-

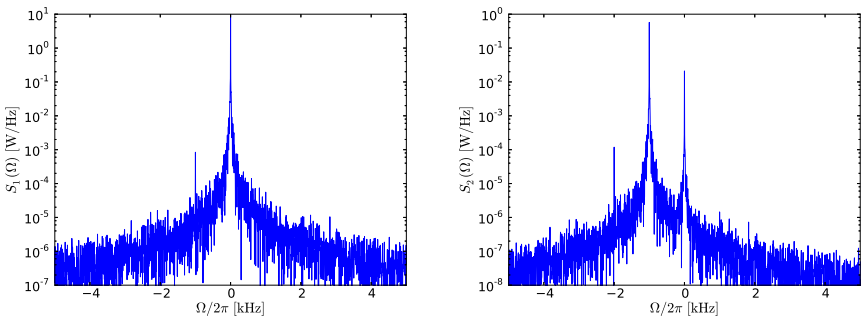

(a) FM spectrum (b) HOM spectrum

Figure 6.13: Output PSD of the light in (a) LP_{01} and (b) LP_{11} of the SIF amplifier described in Fig. 6.12 with an amplitude modulated input signal. The first Stokes sideband of the HOM acts as a seed for TMI and experiences nonlinear gain, while the anti-Stokes side band of the FM is depleted by coupling to the HOM carrier. The seed for the second Stokes sideband of the HOM is generated by an intra-modal FWM process between the initial frequency components.

tween LP_{01} and LP_{11} is strong. The result for the simulation discussed above is plotted in Fig. 6.14 and shows a single strong peak at $\Omega/(2\pi) = 1$ kHz and a much weaker peak at the second harmonic $\Omega/(2\pi) = 2$ kHz. This result is easily understood from the spectra shown in Fig. 6.13 as an interference between the FM carrier and the amplified Stokes sideband of the HOM.

We now consider the behavior of the fiber amplifier when operating above the TMI threshold. We therefore set the gain coefficient $g = \ln(400)/(\Gamma_1 L)$, with all other parameters being the same as above. From the mode power and HOM content plotted in Fig. 6.15 we see that a significant fraction of the power has been transferred from the FM to the HOM at this gain, with the output HOM content $\xi(L) \approx 0.69$.

From the output PSD, plotted in Fig. 6.16, we see that the Stokes sideband at $\Omega = -1$ kHz of the HOM has been amplified as expected. However, we also clearly see the presence of additional Stokes and anti-Stokes sidebands in the HOM spectrum, which are generated by the aforementioned FWM process. In the FM, the original carrier at $\Omega = 0$ has been depleted and a new Stokes sideband at $\Omega = -2\Omega_m$ has appeared, and the original anti-Stokes sideband, which was depleted at the lower gain, has been restored by the FWM process. The additional Stokes sidebands act as seeds for the nonlinear power transfer

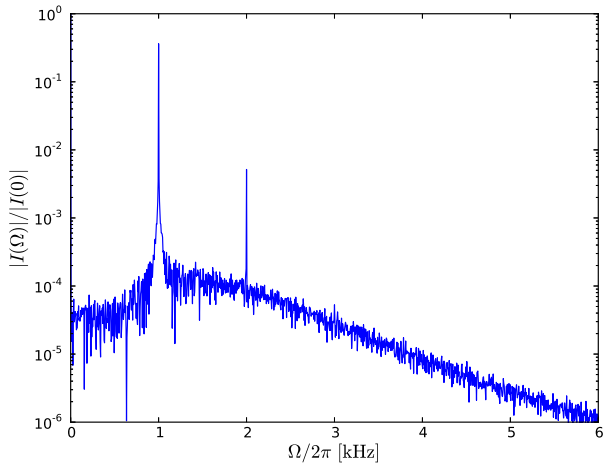

Figure 6.14: Spectrum of the output intensity at a point located at $r = 20$ μm, $\phi = 0$ of the SIF amplifier described in Fig. 6.12. The intensity fluctuations are harmonic with a strong component at 1 kHz and a much weaker component at 2 kHz. The peaks are due to interference between the FM carrier and the first and second Stokes sidebands of the HOM.

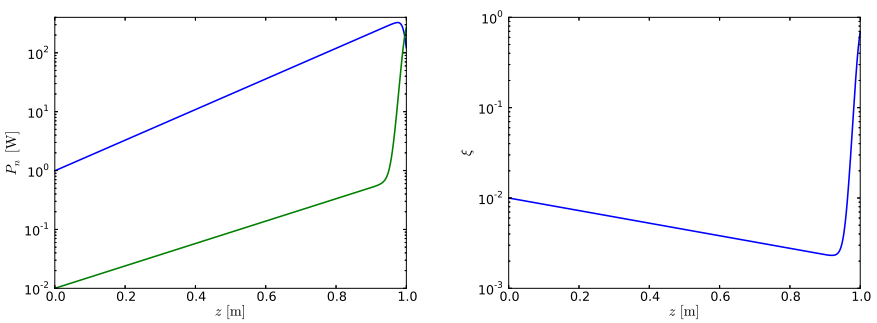

(a) Mode power

(b) HOM content

Figure 6.15: (a) Average mode power P_n and (b) HOM content ξ as a function of z for 1 m of Fiber A with $g = \ln(400)/\Gamma_1$ m^{-1}. The input signal is an amplitude modulated signal with a linewidth due to phase noise of 1 Hz, a modulation depth $a = 10^{-4}$ and a modulation frequency $\Omega_m/(2\pi) = 1$ kHz. The input power in the FM / HOM is 0.99 W / 0.01 W.

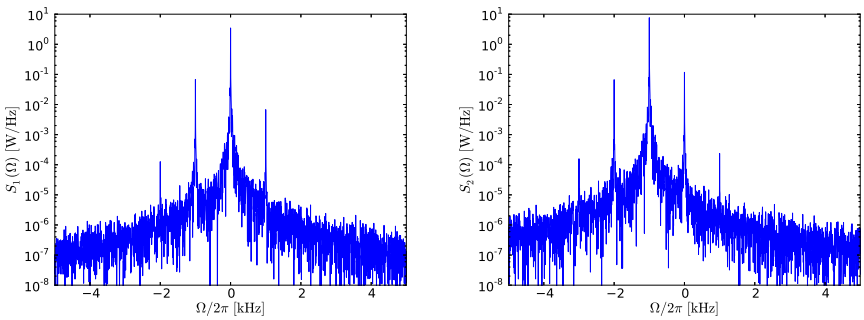

(a) FM spectrum (b) HOM spectrum

Figure 6.16: Output PSD of the light in (a) LP_{01} and (b) LP_{11} of the SIF amplifier described in Fig. 6.15 with an amplitude modulated input signal. The additional Stokes sidebands are generated by intra-modal FWM, and experience nonlinear gain in a cascade process.

between the modes. This cascading process continues as power is increased, generating and amplifying additional Stokes sidebands, until the power reaches the threshold for RIN or quantum noise induced TMI at which point the noise seeding will produce a broad spectrum which masks out the discrete sidebands.

We note that the cascade process described above requires that the modulation frequency is close to the frequency of the peak of the nonlinear gain. A modulation frequency much higher than the nonlinear gain peak frequency will lead to sidebands that do not experience significant nonlinear gain. Intensity modulations of lower modulation frequencies may lead to a larger gain of higher-order sidebands, generated by FWM, compared to the lowest-order sideband if the frequency offset of the higher-order sidebands match the nonlinear gain peak frequency, depending on the relative strength of the sidebands.

We again plot the intensity spectrum of the output beam, shown in Fig. 6.17, from which we can identify the presence of the second, third and fourth harmonic of the modulation frequency in the output intensity. These harmonics are caused by interference between the different Stokes sidebands of the FM and HOM output.

Finally, we consider operation well above the TMI threshold, setting the gain coefficient $g = \ln(700)/(\Gamma_1 L)$. The average mode power and HOM content as a function of z are plotted in Fig. 6.18 and shows the average power being transferred between the modes after the TMI threshold is reached. The

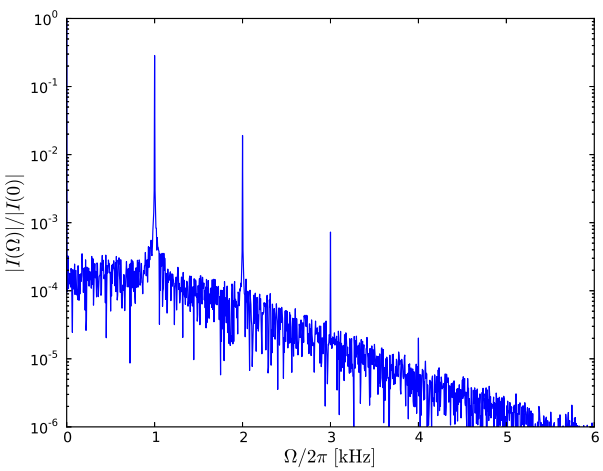

Figure 6.17: Spectrum of the output intensity at a point located at $r = 20$ μm, $\phi = 0$ of the SIF amplifier described in Fig. 6.15. The second, third and fourth harmonics of the modulation frequency of 1 kHz are clearly visible, and are due to interference between different spectral components of the FM and HOM.

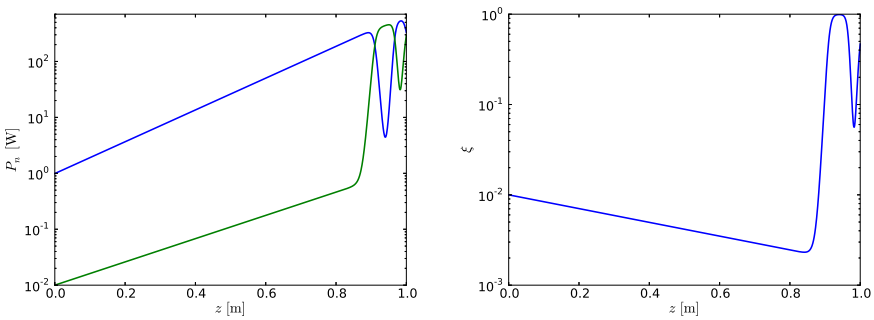

(a) Mode power (b) HOM content

Figure 6.18: (a) Average mode power P_n and (b) HOM content ξ as a function of z for 1 m of Fiber A with $g = \ln(700)/\Gamma_1$ m^{-1}. The input signal is an amplitude modulated signal with a linewidth due to phase noise of 1 Hz, a modulation depth $a = 10^{-4}$ and a modulation frequency $\Omega_m/(2\pi) = 1$ kHz. The input power in the FM / HOM is 0.99 W / 0.01 W.

amplifier is operating well above the threshold for quantum noise induced TMI, which results in the broad output spectra seen in Fig. 6.19. The discrete sidebands seen at lower power levels are no longer present in the spectra.

The broad spectra of the output mode amplitudes result in a chaotic fluctuation in the output intensity, as is evident from the spectrum shown in Fig. 6.20. The intensity spectrum has a broad shape with a maximum around 1 kHz and falls off with increasing frequency. The shape of the curve will depend on fiber parameters, in particular the core diameter [2], but the overall shape is quite similar to what was found in [53, 54].

The behavior of the TMI dynamics with increasing power matches quite well what was observed experimentally by Otto *et al.* [53] and Ward *et al.* [54], and it is therefore possible that the transition behavior observed in these experiments are caused by the mechanism proposed here. The experiment by Karow *et al.*, in which only chaotic intensity fluctuations were observed, is also naturally explained by our model, in the sense that a sufficiently strong harmonic modulation of the input signal is required to produce the harmonic behavior seen near threshold.

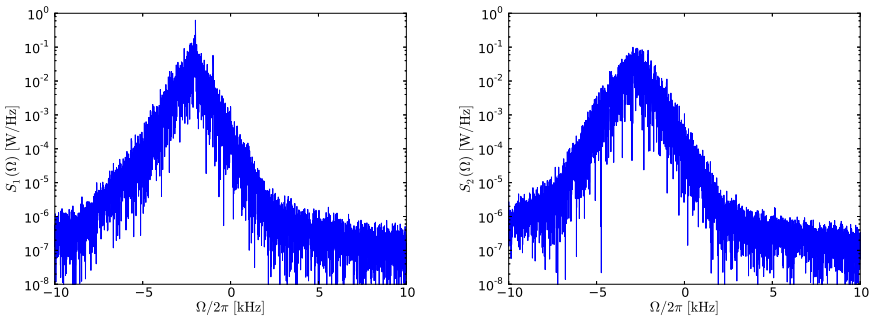

(a) FM spectrum (b) HOM spectrum

Figure 6.19: Output PSD of the light in (a) LP_{01} and (b) LP_{11} of the SIF amplifier described in Fig. 6.18. At this power level, quantum noise seeded TMI results in broad output spectra, without the discrete sidebands seen at lower power.

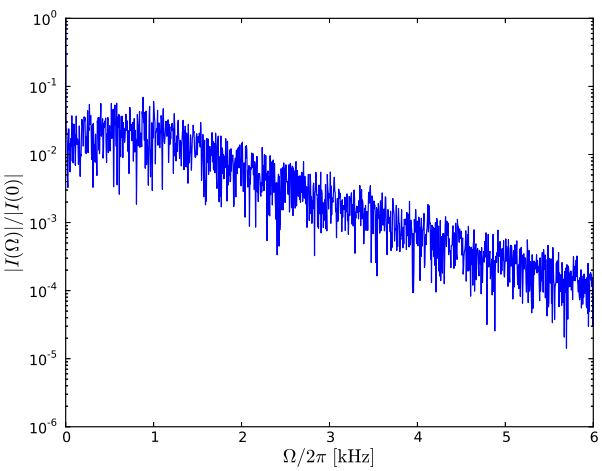

Figure 6.20: Spectrum of the output intensity at a point located at $r = 20$ μm, $\phi = 0$ of the SIF amplifier described in Fig. 6.19 operating well above the TMI threshold. Discrete spectral components are no longer seen at this power level, since quantum noise seeding is dominating. The broad spectrum reflects the chaotic nature of the mode fluctuations.

6.6 Conclusion

In this chapter we have presented a coupled-mode approach to the modeling of TMI in high average power fiber amplifiers. The model has the advantage of numerical simplicity and efficiency, and also lends itself well to approximate semi-analytical solutions. Similarly to the semi-analytic model presented in chapter 5, a number of simplifying assumptions were made, the most limiting being the neglect of the effect of gain saturation and thermal lensing. It may be possible to at least partly relax these assumptions, but this is beyond the scope of the work presented in this thesis. We have also included only the FM and one HOM, but the model can be easily extended to include more modes. This may be necessary in order to accurately model TMI at output powers well above the threshold. For numerical convenience, we have chosen to focus on a SIF amplifier, but the model can be used for any type of fiber for which the modes can be calculated, similarly to the calculations for the PCFs presented in chapter 5. In spite of these limitations, the threshold powers obtained from the model seem to match reasonably well with experiments, and most of the qualitative features of TMI observed in recent experiments agree well with the results.

We have shown how both quantum noise and RIN can act as a seed for TMI, and have shown by an approximate semi-analytical solution of the model that the upper limit on the TMI threshold is due to quantum noise. We also found that the threshold is quite insensitive to perturbations of the amount of signal accidentally launched into a HOM, which is consistent with the experiments by Ward *et al.* [54] and Karow *et al.* [55]. Considering coupling between the LP_{01} and LP_{02} modes, we found that the coupling between these two modes was significantly weaker compared to the coupling between LP_{01} and LP_{11} of the same fiber. This explains why LP_{02}-like modes have so far not been observed in experiments on TMI.

Experimentally it has been found that various types of cooling of the fiber amplifier can lead to variations in the TMI threshold power [54]. While the model allows for a varying cooling efficiency through the thermal boundary condition, we found no effect of varying the efficiency of the cooling. It should be noted, however, that the model only considers symmetric cooling of the fiber, which may not be appropriate for experiments in which the fiber is mounted on a heat sink. Furthermore, we have assumed that the thermal properties of fused silica are independent of temperature, which is an approximation that may not hold when the fiber amplifier is passively cooled.

By numerically solving the coupled-mode equations of the model, we investigated the behavior of the fiber amplifier above the TMI threshold and found that in the case of quantum noise seeding, the average power in each of the

two modes seems to converge to half the total power as the output power is increased well beyond the threshold. No drop in total output power is associated with reaching the TMI threshold, and the instability provides no impediment to increasing the signal power above the threshold power. This is consistent with what was reported by Eidam *et al.* [16]. The instantaneous power in each mode was found to fluctuate chaotically on a ms timescale in a manner similar to the findings of Stutzki *et al.* [52]. As discussed in chapter 5, this timescale depends on the core diameter of the fiber. We also found that the TMI threshold and dynamics was insensitive to the bandwidth of the input signal, consistent with the findings of Ward *et al.* [54].

Finally, we have investigated the effect of a small harmonic intensity modulation of the input signal on TMI, and shown how it may lead to the generation of discrete frequency components in the intensity of the output beam through a combination of thermally induced intra-modal FWM and inter-modal coupling. This effect may explain the behavior in the transition region near threshold observed in the recent experiments by Otto *et al.* [53] and Ward *et al.* [54].

The decrease in TMI threshold power with increasing core diameter reported in [46] cannot be explained by the model presented in this chapter. This is because the model assumes that the mode profiles are unaffected by the radial thermal gradient. As shown theoretically in [1] and experimentally in [46], this is not the case for LMA fiber amplifiers and the thermal lensing effect becomes more pronounced with increasing MFD.

In terms of mitigation strategies, the ever-present quantum noise means that in order to push the output power beyond the quantum noise TMI threshold, which can be as low as a few hundred W, fiber designs which reduce the overlap between the FM and any HOMs, as well as with the doped region, should be considered, as we discussed in chapter 5. PCF fiber designs combining index guiding with PBGs to provide nearly single-mode operation in a limited bandwidth can also be effective in increasing the TMI threshold, but due to the sensitivity of the bandgap location to the heating of the core [4], such fibers must be designed for use specifically at high operating power.

Intensity noise reduction can also increase the TMI threshold, but as we have shown, the threshold power is rather insensitive to the RIN level, and so the effect of noise reduction is expected to be modest. On the other hand, the presence of discrete spectral components of the RIN at a frequency close to the peak TMI gain of the fiber may lead to a substantial reduction of the TMI threshold, and active stabilization measures to reduce such spectral components may be worthwhile.

Chapter 7

Summary and outlook

Despite the excellent thermal properties of Yb-doped fiber amplifiers compared to conventional laser systems, the push towards higher average operating power means that thermo-optical effects are beginning to pose significant challenges to fiber lasers and amplifiers as well. The purpose of the work presented in this thesis is to provide a theoretical understanding of these effects, with a particular emphasis on the very recently discovered phenomenon of TMI. Here, a summary of the results obtained and a discussion and outlook towards future research is given.

7.1 Summary

In chapter 3 a 2D BPM model of an Yb-doped fiber amplifier was presented, which included the effects of THB of the gain and the thermo-optic effect. The model was used to study LMA single-mode amplifiers, and it was shown that large radial temperature gradients caused a thermal lensing effect, which significantly reduced the MFD of the beam. This effect leads to enhanced nonlinear optical effects, such as SPM under pulsed operation. It was also found that the thermo-optic effect can be large enough to render a nominally single-mode fiber effectively multimode, and that the local modes can vary significantly depending on the local thermal load. The model failed to convincingly reproduce TMI, showing only a modest transfer of power between the FM and first HOM at an output power an order of magnitude higher than what is observed experimentally for fibers of similar characteristics.

The 2D BPM model was extended to a 3D model in chapter 4 by expanding the azimuthal dependence of the dynamical variables in a truncated Fourier series. Since the fiber under study was only slightly multimode, only a few terms

in the Fourier expansion were required, leading to an efficient implementation compared to conventional 3D BPM codes. The model was used to study the interaction between the LP_{01} and LP_{11} modes in a LMA rod-type fiber, but no TMI was observed. The failure of the BPM models to convincingly reproduce TMI is due to the fact that a perfect CW signal is assumed, which means that the thermal profile can be calculated under the assumption of steady-state. The thermally induced refractive index grating is thus in phase with the mode beating pattern of the two modes, which precludes the efficient coupling of the modes. The modest mode coupling observed in chapter 3 is most likely due to the large longitudinal temperature gradient in this simulation, which causes a longitudinal variation in the periodicity of the index grating.

A semi-analytic model of TMI was presented in chapter 5, which showed that the phenomenon can indeed be understood as a thermally induced coupling between the FM and a HOM. The coupling is mediated by the thermally induced refractive index grating, but unlike in the BPM models, the grating is not stationary since the mode coupling was assumed to be seeded by frequency components of quantum noise redshifted by about 1 kHz relative to the signal. The finite response time of the thermal nonlinearity causes the refractive index grating to lag behind the mode beating pattern, which permits efficient power transfer to occur between the modes. The model provided a simple semi-analytical method for calculating the TMI threshold power, and was used to study the dependence of the threshold on various design parameters of a SIF. It was also shown how the model can be applied to PCF designs. In general, it was found that the threshold power decreases with increasing overlap between the modes and the doped region of the fiber core.

The main results on TMI were presented in chapter 6, in which a coupled-mode model of the phenomenon was formulated. The model is based on the same basic idea as the semi-analytic model in chapter 5, but is much more general, and can be used to study the temporal dynamics of TMI, both at threshold and beyond. It was found that signal intensity noise can also act as seed for TMI, and gives a lower threshold compared to quantum noise seeding. The effect of a small amplitude modulation of the input signal was also studied, and it was found that the "transition regime" observed in some recent experiments [53, 54] could be explained by a combination of thermally induced FWM and mode coupling. A number of qualitative features of TMI reported in recent experiments were compared to the results of the model, and it was found that almost all of them could be explained by the model. A more detailed discussion of this comparison can be found in the conclusion of chapter 6.

7.2 Outlook

TMI has become one of the main challenges in the ongoing effort to increase the output power of rare-earth doped fiber laser systems. While it is possible to increase the output power beyond the TMI threshold, the resulting loss of beam quality and pointing stability can render the laser effectively useless for applications that require high beam quality. It is therefore of considerable interest to investigate mitigation strategies that can significantly increase the TMI threshold. This work should benefit from an increased theoretical understanding of the phenomenon.

In terms of the work presented in this thesis, the semi-analytic and coupled-mode models presented in chapter 5 and 6 could conceivably be improved by taking the effects of gain saturation and thermal lensing into account in an approximate way. This should lead to better quantitative agreement with measured TMI threshold powers. Efforts by Jørgensen *et al.* to take thermal lensing into account in the semi-analytic model has already shown significant quantitative improvement in the results [6, 7].

The BPM models presented in chapters 3 and 4 could also be extended to include the temporal dynamics of the thermal nonlinearity. This has the advantage of taking gain saturation and thermal lensing fully into account, but at the expense of numerical complexity. A full 3D BPM model including temporal dynamics has been implemented by Smith and Smith [38] using a 2D cartesian grid for the transverse discretization. Including temporal dynamics in the Fourier expansion BPM algorithm presented in chapter 4 should be numerically more efficient, which would be very useful considering the long simulation time required by such models.

As for fiber amplifiers designed to increase the TMI threshold, the results presented in this thesis show that the key to obtaining a high threshold power is to reduce the overlap of any HOMs with the FM and the core. The LPFs presented in [15] were designed for this purpose. Another technique to obtain effectively single-mode behavior in a LMA fiber is to use the PBG effect to "filter out" the HOMs in a limited wavelength range [4]. However, both approaches are hindered by the presence of strong radial thermal gradients during high average power operation, which significantly alter the guiding properties of the fiber. However, it is possible that the latter approach could be refined to design a LMA fiber with effectively single-mode guidance at high average power by proper design of the mode filtering elements in the cladding microstructure. Such a fiber could potentially have a very high TMI threshold. The drawback of this approach would be that the fiber would be designed specifically for high power operation, and would likely have very poor guidance properties at low average power. The great design flexibility offered by PCFs should nonethe-

List of acronyms

BPM beam propagation method

CW continuous wave

FEM finite element method

FFT fast Fourier transform

FM fundamental mode

FSM fundamental space-filling mode

FWM four-wave mixing

GVD group-velocity dispersion

HOM higher-order mode

LMA large mode area

LPF large pitch fiber

MFD mode field diameter

NA numerical aperture

PBG photonic bandgap

PCF photonic crystal fiber

PM polarization-maintaining

PSD power spectral density

RIN relative intensity noise

SAP stress-applying part

SBS stimulated Brillouin scattering

SIF step-index fiber

SPM self-phase modulation

SRS stimulated Raman scattering

THB transverse hole burning

THG third-harmonic generation

TIR total internal reflection

TMI transverse mode instability

XPM cross-phase modulation

Bibliography

[1] K. R. Hansen, T. T. Alkeskjold, J. Broeng, and J. Lægsgaard, "Thermo-optical effects in high-power Ytterbium-doped fiber amplifiers," Opt. Express **19**, 23965–23980 (2011).

[2] K. R. Hansen, T. T. Alkeskjold, J. Broeng, and J. Lægsgaard, "Thermally induced mode coupling in rare-earth doped fiber amplifiers," Opt. Lett. **37**, 2382–2384 (2012).

[3] K. R. Hansen, T. T. Alkeskjold, J. Broeng, and J. Lægsgaard, "Theoretical analysis of mode instability in high-power fiber amplifiers," Opt. Express (submitted for publication).

[4] M. Laurila, M. M. Jørgensen, K. R. Hansen, T. T. Alkeskjold, J. Broeng, and J. Lægsgaard, "Distributed mode filtering rod fiber amplifier delivering 292W with improved mode stability," Opt. Express **20**, 5742–5753 (2012).

[5] K. R. Hansen, and J. Lægsgaard, "Thermal Effects in High-Power Fiber Amplifiers," in *CLEO:2011 - Laser Applications to Photonic Applications*, OSA Technical Digest (CD) (Optical Society of America, 2011), paper JWA32.

[6] M. M. Jørgensen, K. R. Hansen, M. Laurila, D. Noordegraaf, T. T. Alkeskjold, and J. Lægsgaard, "Modal instabilities in very large mode area rod fiber amplifiers," in *Northern Optics 2012*, Snekkersten, Denmark (2012).

[7] M. M. Jørgensen, K. R. Hansen, M. Laurila, T. T. Alkeskjold, and J. Lægsgaard, "Modal instability of rod fiber amplifiers: a semi-analytic approach," in *SPIE, Photonics West 2013* (accepted).

[8] Y. Jeong, J. K. Sahu, D. N. Payne, and J. Nilsson, "Ytterbium-doped large-core fibre laser with 1 kW of continuous-wave output power," Electron. Lett. **40**, 470–471 (2004).

[9] D. C. Brown, and H. J. Hoffman, "Thermal, Stress, and Thermo-Optic Effects in High Average Power Double-Clad Silica Fiber Lasers," IEEE J. Quantum Electron. **37**, 207–217 (2001).

[10] J. Limpert, T. Schreiber, A. Liem, S. Nolte, H. Zellmer, T. Peschel, V. Guyenot, A. Tünnermann, "Thermo-optical properties of air-clad photonic crystal fiber lasers in high power operation," Opt. Express **11**, 2982–2990 (2003).

[11] L. Li, H. Li, T. Qiu, V. L. Temyanko, M. M. Morrell, A. Schülzgen, A. Mafi, J. V. Moloney, and N. Peyghambarian, "3-Dimensional thermal analysis and active cooling of short-length high-power fiber lasers," Opt. Express **13**, 3420–3428 (2005).

[12] J. Li, K. Duan, Y. Wang, X. Cao, W. Zhao, Y. Guo, and X. Lin, "Theoretical analysis of the heat dissipation mechanism in Yb^{3+}-doped double-clad fiber lasers," J. Mod. Opt. **55**, 459–471 (2008).

[13] S. Hädrich, T. Schreiber, T. Pertsch, J. Limpert, T. Peschel, R. Eberhardt, and A. Tünnermann, "Thermo-optical behavior of rare-earth-doped low-NA fibers in high power operation," Opt. Express **14**, 6091–6097 (2006).

[14] T. Eidam, S. Hanf, E. Seise, T. V. Andersen, T. Gabler, C. Wirth, T. Schreiber, J. Limpert, and A. Tünnermann, "Femtosecond fiber CPA system emitting 830 W average output power," Opt. Lett. **35**, 94–96 (2010).

[15] F. Stutzki, F. Jansen, T. Eidam, A. Steinmetz, C. Jauregui, J. Limpert, and A. Tünnermann, "High average power large-pitch fiber amplifier with robust single-mode operation," Opt. Lett. **36**, 689–691 (2011).

[16] T. Eidam, C. Wirth, C. Jauregui, F. Stutzki, F. Jansen, H.-J. Otto, O. Schmidt, T. Schreiber, J. Limpert, and A. Tünnermann, "Experimental observations of the threshold-like onset of mode instabilities in high power fiber amplifiers," Opt. Express **19**, 13218–13224 (2011).

[17] J. Lægsgaard, *Introduction to optical fibers - Lecture notes for course 34041* (DTU Fotonik 2010).

[18] J. C. Knight, T. A. Birks, P. St. J. Russell, and D. M. Atkin, "All-silica single-mode optical fiber with photonic crystal cladding," Opt. Lett. **21**, 1547–1549 (1996).

[19] M. Koshiba, and K. Saitoh, "Applicability of classical optical fiber theories to holey fibers," Opt. Lett. **29**, 1739–1741 (2004).

[20] J. D. Joannopoulos, S. G. Johnson, J. N. Winn, and R. D. Meade, *Photonic Crystals - Molding the Flow of Light, 2. edition* (Princeton University Press 2008).

[21] T. T. Alkeskjold, "Large-mode-area ytterbium-doped fiber amplifier with distributed narrow spectral filtering and reduced bend sensitivity," Opt. Express **17**, 16394–16405 (2009).

[22] T. T. Alkeskjold, M. Laurila, L. Scolari, and J. Broeng, "Single-mode ytterbium-doped large-mode-area photonic bandgap rod fiber amplifier," Opt. Express **19**, 7398–7409 (2011).

[23] J. Stone, and C. A. Burrus, "Neodymium-doped silica lasers in end-pumped fiber geometry," Appl. Phys. Lett. **23**, 388–389 (1973).

[24] D. T. Walton, J. Nees, and G. Mourou, "Broad-bandwidth pulse amplification to the 10-μJ level in an ytterbium-doped germanosilicate fiber," Opt. Lett. **21**, 1061–1063 (1996).

[25] F. Jansen, F. Stutzki, C. Jauregui, J. Limpert, and A. Tünnermann, "High-power very large mode-area thulium-doped fiber laser," Opt. Lett. **37**, 4546–4548 (2012).

[26] H. M. Pask, R. J. Carman, D. C. Hanna, A. C. Tropper, C. J. Mackechnie, P. R. Barber, and J. M. Dawes, "Ytterbium-Doped Silica Fiber Lasers: Versatile Sources for the 1–1.2 μm Region," IEEE J. Sel. Topics Quantum Electron. **1**, 2–13 (1995).

[27] T. C. Newell, P. Peterson, A. Gavrielides, and M. P. Sharma, "Temperature effects on the emission properties of Yb-doped optical fibers," Opt. Commun. **273**, 256–259 (2007).

[28] G. P. Agrawal, *Nonlinear Fiber Optics, 4. edition* (Elsevier 2007).

[29] J. Limpert, F. Röser, D. N. Schimpf, E. Seise, T. Eidam, S. Hädrich, J. Rothhardt, C. J. Misas, and A. Tünnermann, "High Repetition Rate Gigawatt Peak Power Fiber Laser Systems: Challenges, Design, and Experiment," IEEE J. Sel. Topics Quantum Electron. **15**, 159–169 (2009).

[30] R. G. Smith, "Optical Power Handling Capacity of Low Loss Optical Fibers as Determined by Stimulated Raman and Brillouin Scattering," Appl. Opt. **11**, 2489–2494 (1972).

[31] J. M. Fini, M. D. Mermelstein, M. F. Yan, R. T. Bise, A. D. Yablon, P. W. Wisk, and M. J. Andrejco, "Distributed suppression of stimulated Raman scattering in an Yb-doped filter-fiber amplifier," Opt. Lett. **31**, 2550–2552 (2006).

[32] J. Kim, P. Dupriez, C. Codemard, J. Nilsson, and J. K. Sahu, "Suppression of stimulated Raman scattering in a high power Yb-doped fiber amplifier using a W-type core with fundamental mode cut-off," Opt. Express **14**, 5103–5113 (2006).

[33] C. Zeringue, I. Dajani, S. Naderi, G. T. Moore, and C. Robin, "A theoretical study of transient stimulated Brillouin scattering in optical fibers seeded with phase-modulated light," Opt. Express **20**, 21196–21213 (2012).

[34] C. Robin, and I. Dajani, "Acoustically segmented photonic crystal fiber for single-frequency high-power laser applications," Opt. Lett. **36**, 2641–2643 (2011).

[35] Y. Jeong, J. K. Sahu, D. N. Payne, and J. Nilsson, "Ytterbium-doped large-core fiber laser with 1.36 kW continuous-wave output power," Opt. Express **12**, 6088–6092 (2004).

[36] D. Gapontsev, "6 kW CW single mode Ytterbium fiber laser in all-fiber format," in *Proc. Solid State and Diode Laser Technology Review* (2008).

[37] C. Jauregui, T. Eidam, J. Limpert, and A. Tünnermann, "The impact of modal interference on the beam quality of high-power fiber amplifiers," Opt. Express **19**, 3258–3271 (2011).

[38] A. V. Smith, and J. J. Smith, "Mode instability in high power fiber amplifiers," Opt. Express **19**, 10180–10192 (2011).

[39] R. W. Boyd, *Nonlinear Optics, 3. edition* (Elsevier 2008).

[40] P. W. Milonni, and J. H. Eberly, *Lasers* (John Wiley & Sons 1988).

[41] D. E. McCumber, "Einstein Relations Connecting Broadband Emission and Absorption Spectra," Phys. Rev. **136**, A954–A957 (1964).

[42] G. R. Hadley, "Transparent boundary condition for beam propagation," Opt. Lett. **16**, 624–626 (1991).

[43] W. H. Press, B. P. Flannery, S. A. Teukolsky, and W. T. Vetterling, *Numerical Recipes in Pascal* (Cambridge University Press 1989).

[44] S. Wielandy, "Implications of higher-order mode content in large mode area fibers with good beam quality," Opt. Express **15**, 15402–15409 (2007).

[45] N. A. Mortensen, and J. R. Folkenberg, "Low-loss criterion and effective area considerations for photonic crystal fibres," J. Opt. A: Pure Appl. Opt. **5**, 163–167 (2003).

[46] F. Jansen, F. Stutzki, H.-J. Otto, T. Eidam, A. Liem, C. Jauregui, J. Limpert, and A. Tünnermann, "Thermally induced waveguide changes in active fibers," Opt. Express **20**, 3997–4008 (2012).

[47] C. Jauregui, T. Eidam, H.-J. Otto, F. Stutzki, F. Jansen, J. Limpert, and A. Tünnermann, "Temperature-induced index gratings and their impact on mode instabilities in high-power fiber laser systems," Opt. Express **20**, 440–451 (2012).

[48] K. D. Cole, and P. E. Crittenden, "Steady-Periodic Heating of a Cylinder," ASME J. Heat Transfer **131**, 091301 (2009).

[49] G. B. Arfken, and H. J. Weber, *Mathematical Methods for Physicists, 6. edition* (Elsevier 2005).

[50] E. Desurvire, and J. R. Simpson, "Amplification of Spontaneous Emission in Erbium-Doped Single-Mode Fibers," J. Lightwave Technol. **7**, 835–845 (1989).

[51] E. Coscelli, F. Poli, D. Passaro, A. Cucinotta, S. Selleri, C. B. Olausson, L. Leick, and J. Broeng, "Bending-Induced Single-Mode Behaviour of a Polarizing Double-clad Yb-Doped Photonic Crystal Fiber," presented at *36th European Conference and Exhibition on Optical Communication* (2010).

[52] F. Stutzki, H.-J. Otto, F. Jansen, C. Gaida, C. Jauregui, J. Limpert, and A. Tünnermann, "High-speed modal decomposition of mode instabilities in high-power fiber lasers," Opt. Lett. **36**, 4572–4574 (2011).

[53] H.-J. Otto, F. Stutzki, F. Jansen, T. Eidam, C. Jauregui, J. Limpert, and A. Tünnermann, "Temporal dynamics of mode instabilities in high-power fiber lasers and amplifiers," Opt. Express **20**, 15710–15722 (2012).

[54] B. Ward, C. Robin, and I. Dajani, "Origin of thermal modal instabilities in large mode area fiber amplifiers," Opt. Express **20**, 11407–11422 (2012).

[55] M. Karow, H. Tünnermann, J. Neumann, D. Kracht, and P. Weßels, "Beam quality degradation of a single-frequency Yb-doped photonic crystal fiber amplifier with low mode instability threshold power," Opt. Lett. **37**, 4242–4244 (2012).

[56] D. B. Leviton, and B. J. Frey, "Temperature-dependent absolute refractive index measurements of synthetic fused silica," in Proc. SPIE **6273**, *Optomechanical Technologies for Astronomy*, 62732K (2006).

[57] P. N. Brown, G. D. Byrne, and A. C. Hindmarsh, "VODE: A Variable Coefficient ODE Solver," SIAM J. Sci. Stat. Comput. **10**, 1038–1051 (1989).

[58] J. Chen, J. W. Sickler, E. P. Ippen, and F. X. Kärtner, "High repetition rate, low jitter, low intensity noise, fundamentally mode-locked 167 fs soliton Er-fiber laser," Opt. Lett. **32**, 1566–1568 (2007).

Copyright:
Kristian Rymann Hansen
and DTU Fotonik
All rights reserved
ISBN: 978-87-93089-16-7

Published by:
DTU Fotonik
Department of Photonic Engineering
Technical University of Denmark
Ørstyeds Plads, building 343
DK-2800 Kgs. Lyngby

Kristian Rymann Hansen was born in Aarhus, Denmark, and received his M.Sc. degree in physics from the University of Aarhus in 2006. After working as a research scientist in the Norwegian company Electromagnetic Geoservices for 3 years, he began his PhD studies at the Technical University of Denmark, which resulted in the research presented in this thesis.

DTU Fotonik
Department of Photonics Engineering